

Biophysical applications of correlative scanning probe and super-resolution microscopy

Présentée le 23 septembre 2021

Faculté des sciences et techniques de l'ingénieur
Laboratoire de biologie à l'échelle nanométrique
Programme doctoral en biotechnologie et génie biologique

pour l'obtention du grade de Docteur ès Sciences

par

Vytautas NAVIKAS

Acceptée sur proposition du jury

Prof. Ph. Renaud, président du jury
Prof. A. Radenovic, directrice de thèse
Prof. A. Diaspro, rapporteur
Prof. Y. Korchev, rapporteur
Prof. B. Fierz, rapporteur

A man should look for what it is,
not for what he thinks it should be.
— Albert Einstein

Acknowledgements

The journey towards PhD is not a journey that a person would take on his/her own. During 4 years of my PhD studies, I met intelligent, talented and open-minded people willing to share their expertise and help in a variety of situations in everyday lab life. All the people I have met in EPFL were the source of energy and knowledge which allowed me to grow professionally and personally during my PhD years.

First, I would like to thank my supervisor Prof. Aleksandra Radenovic for giving me an opportunity to pursue a PhD at EPFL. Aleksandra is a caring person with a remarkable passion for science and knowledge, who gives everyone the freedom of “scientific expression”. The most important part of the whole PhD journey is feedback and I am grateful for Aleksandra because she was always available to read a new manuscript or to suggest how to fix a non-working microscope, thus making research work so much more rewarding.

During these years I constantly collaborated with Samuel Leitão, a PhD student from LBNI led by Prof. Georg Fantner. Samuel’s help was essential for my PhD and I am really happy that we have learned a lot from each other. We both have started our PhDs at a similar time and have sorted out loads of problems together and became good friends. I am also grateful to Prof. Georg Fantner for fruitful discussions and his support of our collaboration with Samuel. I want to thank all former and present LBEN team members for supporting me during these eventful 4 years. In particular, I am grateful for Sanjin Marion and his realistic worldview not only for helping me to understand the mysteries of nanofluidics but also for various discussions and MTB trips. I thank Kristin Größmayer for showing the secrets of fluorescence microscopy and Adrien Descloux for always taking time to help and solve various microscopy related problems. I am also thankful for Lely Feletti for her constant support in the lab and a tolerant attitude towards my liberal approach to the lab order. I am grateful to Evgenii Glushkov for his continuous optimism and bravery in going with me to summer school. I thank Michael Graf for believing in me, Mukeshchand Thakur for doing a first TA together, Michal Macha for healthy sarcasm, Martina Lihter for organizing a lot of festive activities for the whole group, Andrey Chernev for his musical powers, Arielle Planchette for always finding a time to have a friendly conversation, Sebastian Davis for sharing a burden of nanocapillary fabrication, Simon Mayer for sharing his cuisine masterpieces, Nathan Ronceray for his pure positivity, Miao Zhang for constructive sharing of PALM setup, Martine Truan for her professional administrative support and all the other LBEN members for being supportive colleagues.

Finally, I am grateful to my parents for fostering curiosity from a very young age, thus moti-

Acknowledgements

vating me to pursue a scientific career and lastly, I am thankful to my beloved wife Ieva, who came with me to Lausanne and constantly supported me.

V.N.

Abstract

Imaging live cells in their native environment is crucial for the understanding of complex biological phenomena. Modern optical microscopy methods such as fluorescence super-resolution microscopy are increasingly combined with complementary, label-free techniques to put the high-resolution fluorescence information into cellular context. Common high-resolution imaging approaches used in combination with fluorescence imaging such as electron microscopy and atomic force microscopy (AFM) were originally developed for solid-state material characterization and thus are not straightforwardly applicable to image live cells for sustained periods of time. In this thesis, I am focusing on advancing state-of-the-art correlative scanning ion-conductance microscopy (SICM) combined with novel super-resolution imaging techniques. The work presented in this thesis demonstrates various technological advancements for both imaging modalities as well as experimental proof-of-principle studies. The first part of the work focuses on a novel experimental combination of SICM and super-resolution optical fluctuation imaging for single-cell imaging (SOFI). To demonstrate the capabilities of our method we show correlative 3D cellular maps with SOFI implementation in both 2D and 3D with self-blinking dyes for two-color high-order SOFI imaging. We employ correlative SICM/SOFI microscopy for visualizing actin dynamics in live COS-7 cells with subdiffraction resolution. In order to increase the imaging depth for thick samples, a novel remote focusing modality based on an adaptive optics device was developed. Here, we use a deformable mirror to acquire multiple image planes of the labelled cells and we process the data using a single-molecule localization routine and/or computed spatiotemporal correlations, demonstrating subdiffraction resolution within a whole imaging volume. Second, we demonstrate the advantages of a new SICM probe manufacturing method allowing the batch production of glass nanopipettes used for SICM imaging and sensing. Finally, we show a new application of SICM tailored for single-molecule characterization based on electrical signatures while performing controlled translocations of surface-immobilized DNA molecules. The method is developed to be compatible with single-molecule fluorescence imaging and was applied for the detection of various analytes in a correlative manner. We believe that a synergy between fundamentally different imaging modalities is going to become necessary in an age of computational microscopy to ensure an unbiased data interpretation in the rapidly progressing field of biological research.

Résumé

L'imagerie de cellules vivantes dans leur environnement naturel est cruciale pour la compréhension de phénomènes biologiques complexes. Les méthodes modernes de microscopie optique, telles que la microscopie à super-résolution par fluorescence, sont de plus en plus souvent associées à des techniques complémentaires sans marquage, afin de replacer les informations de fluorescence à haute résolution dans le contexte cellulaire. Les approches courantes d'imagerie à haute résolution utilisées en combinaison avec l'imagerie de fluorescence, telles que la microscopie électronique et la microscopie à force atomique (AFM), ont été développées à l'origine pour la caractérisation des matériaux à l'état solide et ne sont donc pas directement applicables à l'imagerie des cellules vivantes pendant des périodes prolongées. Dans cette thèse, je me concentre sur l'avancement de la microscopie corrélative à balayage à conductivité ionique (SICM) de pointe combinée à de nouvelles techniques d'imagerie à super-résolution. Le travail présenté dans cette thèse démontre diverses avancées technologiques pour les deux modalités d'imagerie ainsi que des études expérimentales de preuve de principe. La première partie du travail se concentre sur une nouvelle combinaison expérimentale de la SICM et de l'imagerie de fluctuation optique à super-résolution pour l'imagerie de cellules uniques (SOFI). Pour démontrer les capacités de notre méthode, nous présentons des cartes cellulaires 3D corrélatives avec la mise en œuvre de SOFI en 2D et 3D avec des colorants auto-bloquants pour l'imagerie SOFI bicolore d'ordre élevé. Nous utilisons la microscopie corrélative SICM/SOFI pour visualiser la dynamique de l'actine dans des cellules COS-7 vivantes avec une résolution inférieure à la diffraction. Afin d'augmenter la profondeur d'imagerie pour les échantillons épais, une nouvelle modalité de focalisation à distance basée sur un dispositif d'optique adaptative a été développée. Ici, nous utilisons un miroir déformable pour acquérir plusieurs plans d'image des cellules marquées et nous traitons les données en utilisant une routine de localisation de molécules uniques et/ou des corrélations spatio-temporelles calculées, démontrant une résolution subdiffractée dans un volume d'imagerie entier. Ensuite, nous démontrons les avantages d'une nouvelle méthode de fabrication de sondes SICM permettant la production par lots de nanopipettes en verre utilisées pour l'imagerie et la détection SICM. Enfin, nous montrons une nouvelle application du SICM adaptée à la caractérisation de molécules uniques basée sur des signatures électriques tout en effectuant des translocations contrôlées de molécules d'ADN immobilisées en surface. La méthode est développée pour être compatible avec l'imagerie de fluorescence monomoléculaire et a été appliquée pour la détection de divers analytes de manière corrélative. Nous pensons qu'une synergie entre des modalités d'imagerie fondamentalement différentes va

Résumé

devenir nécessaire à l'ère de la microscopie informatique pour assurer une interprétation impartiale des données dans le domaine de la recherche biologique qui progresse rapidement.

Contents

Acknowledgements	iii
Abstract (English/Français)	v
1 Introduction	1
Introduction	1
1.1 Optical microscopy	1
1.1.1 Image formation and diffraction limit	1
1.1.2 Fluorescence microscopy	3
1.2 Super-resolution optical microscopy	5
1.2.1 Far-field super-resolution fluorescence microscopy	6
1.2.2 Stimulated emission depletion microscopy (STED)	7
1.2.3 Structured light illumination microscopy (SIM)	7
1.2.4 Single-molecule localization microscopy (SMLM)	8
1.2.5 Self-blinking dyes for single-molecule localization microscopy	9
1.2.6 3D single-molecule localization microscopy	10
1.2.7 Super-resolution optical fluctuation imaging (SOFI)	11
1.3 Scanning probe microscopy and sensing	14
1.3.1 Atomic force microscopy	14
1.3.2 Scanning ion-conductance microscopy	15
1.3.3 Correlative scanning probe and fluorescence microscopy	16
1.3.4 Probes for scanning ion-conductance microscopy	18
1.4 Introduction to solid-state nanopore sensing	18
1.5 Thesis structure	18
2 Correlative 3D microscopy of single cells using super-resolution and scanning ion-conductance microscopy	21
2.1 Abstract	22
2.2 Introduction	22
2.3 Results	24
2.4 Discussion	31
2.5 Methods and Supporting Information	32
2.5.1 2D widefield fluorescence imaging setup	32

Contents

2.5.2	3D widefield imaging setup	33
2.5.3	Scanning ion-conductance microscopy setup	33
2.5.4	Combined 2D widefield fluorescence /SICM setup	34
2.5.5	Coverslip fabrication	35
2.5.6	Cell culture	35
2.5.7	Sample fixation and staining	36
2.5.8	Two-color sample staining	37
2.5.9	Phalloidin-f-HM-SiR chemical synthesis	37
2.5.10	Imaging buffers	38
2.5.11	Two-color SOFI imaging	38
2.5.12	SICM imaging and processing	39
2.5.13	SOFI Image analysis and image alignment	40
2.5.14	Live-cell SOFI/SICM imaging	40
2.5.15	Correlative 3D SICM/SOFI data rendering	40
2.5.16	Acknowledgements	41
2.6	Supporting figures	41
3	Adaptive optics enables multimode 3D super-resolution microscopy via remote fo-	
	cusing	53
3.1	Introduction	54
3.2	Results	56
3.3	Conclusion	59
3.4	Methods	60
3.4.1	Setup	60
3.4.2	Sample preparation	61
3.4.3	<i>In vitro</i> imaging and calibration routines	61
3.4.4	Image processing	62
3.5	Acknowledgments	63
3.6	Supporting information	64
4	High-Throughput Nanocapillary Filling Enabled by Microwave Radiation for Scan-	
	ning Ion Conductance Microscopy Imaging	71
4.1	Results and discussion	73
4.1.1	Nanocapillary fabrication and characterization	78
4.1.2	Solution	78
4.1.3	Filling of Nanocapillaries	79
4.1.4	Brightfield microscopy imaging	79
4.1.5	Recording of nanocapillary filling dynamics	79
4.1.6	Recording of IV curves	79
4.1.7	Preparation of a fixed COS-7 cell sample	80
4.1.8	Scanning ion conductance microscopy	80
4.1.9	Acknowledgement	80
4.1.10	Supporting Information	80

5	Scanning ion-conductance spectroscopy	85
5.1	Introduction	85
5.1.1	Biological nanopores	86
5.1.2	Solid-state nanopores	86
5.1.3	Controlled DNA translocations	87
5.1.4	Glass nanopores for controlled DNA translocations	87
5.2	Methods and Experimental setups	88
5.2.1	Fabrication and characterization of nanocapillaries	88
5.2.2	Nanocapillary filling procedure	88
5.2.3	Ultra-clean chambers for DNA immobilization	89
5.2.4	Lambda DNA preparation	90
5.2.5	DNA ruler constructs	90
5.2.6	gRNA preparation and immobilization	90
5.2.7	dCas-9-DNA complex formation	91
5.2.8	Surface immobilization	91
5.2.9	Single-molecule fluorescence imaging	92
5.2.10	SICS setup and electrical measurements	93
5.2.11	Data analysis	93
5.3	Results and Discussion	93
5.3.1	DNA rulers for SICS characterization	94
5.3.2	Lateral resolution estimation and SNR improvement strategies	95
5.3.3	SICS application for DNA-protein complex detection	96
5.3.4	Correlative SICS and SM fluorescence measurement	97
5.3.5	dCas-9 binding characterization on λ -DNA and DNA rulers	99
5.4	Conclusion and Outlook	100
6	Conclusion and Outlook	101
7	An Image Portfolio	105
8	Scientific contributions	109
	Bibliography	113
	Curriculum Vitae	133

1 Introduction

1.1 Optical microscopy

From the very dawn of human knowledge, the major scientific and industrial breakthroughs were achieved with novel metrology tools enabling the observation of previously unseen phenomena. One of these tools, in particular, was the light microscope invented in the 16th century. It was first brought to the attention of natural scientists by Antonj van Leeuwenhoek and used to observe living matter. The first of such studies revealed previously unseen microscopic structures of multicellular organisms and arguably observed, for the first time, bacteria and cellular organelles (1). However, it took a few centuries to establish the theoretical and technical frameworks of modern light microscopy and make it a standard tool in modern research.

The following thesis chapter gives a historical and theoretical basis for the optical imaging modalities. The use and discussion of multiple microscopy techniques are important as each modality uses a slightly different sensing scheme, thus resulting in a distinct image. Multimodal correlative approaches used extensively in this thesis are going to be discussed later on.

1.1.1 Image formation and diffraction limit

To understand the biological processes, we want to look at the small scales within single cells that are on or below the intrinsic diffraction limit of light. When dealing with an optical imaging system – it is important to understand how the optical system responds to an infinitesimally small point – known as a point source, since an image is a sum of small points. The property of the lens to collect the photons coming from a single point can be described as:

$$NA = n \sin \alpha \quad (1.1)$$

This important parameter, commonly used in microscopy, is called a numerical aperture

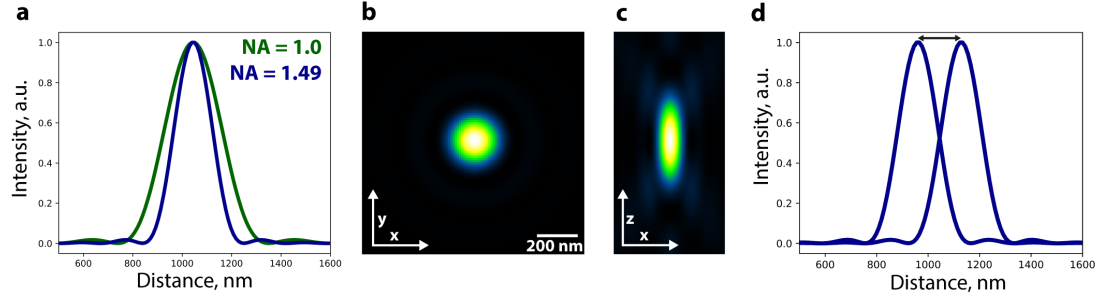


Figure 1.1 – PSF and diffraction limited resolution. (a) A lateral profile of the PSF based on the M.Born and E.Wolf model comparing objectives with different numerical apertures of 1 and 1.49. (b) Lateral and (c) axial PSF intensity plots ($NA = 1.49$, $\lambda = 500$, $n = 1.5$). (d) Lateral intensity profile of 2 point spread functions spaced at the distance equal to Rayleigh's criterion.

(NA), where n is a refractive index and α is the maximum half-angle at which the light can still enter or exit the lens. In modern high-performance microscopy, NA of the high-magnification objectives is typically limited to ≈ 1.5 due to a refraction index of the transparent materials available for fabrication.

The imaging optical system is typically characterized by its three-dimensional point-spread function commonly known as a PSF (Figure 1.1a-b). In ideal and aberration-free objective the PSF can be described using terms of wave-like nature of light. A light wave is emitted as a spherical wave from a point-like object located in the object plane. Based on the Huygens' principle, a spherical wavefront consists of multitude of single point sources, each emitting a spherical wave. All waves from the same wavefront are interfering together in the image plane, resulting in a diffraction pattern also known as Airy pattern. From this pattern, the lateral resolution of the optical systems can be described as:

$$d = 0.5 \frac{\lambda}{NA} \quad (1.2)$$

where NA is the numerical aperture of a lens, λ – wavelength of light used for detection (Figure 1.1c). This famous formulation was first proposed by Ernst Abbe in 1873. Other similar criteria were also proposed by other scientists with different constant in Eq.1.2. The most famous being 0.61 and is called Rayleigh criterion. However, the difference between these criteria is small. In practice, the typical resolution, which is routinely attainable by the diffraction-limited microscopy system, is around 200-250 nm, when high NA (1.4 - 1.5) oil-immersion objectives are used.

The discussed resolution criteria typically uses scalar PSF models, the most commonly being a model proposed by M.Born and E.Wolf(2). According to it, the lateral profile of the PSF corresponds to an Airy disc function:

$$PSF_{xy}(r) = I_0 \left(\frac{2J_1(k_0 r NA)}{k_0 r NA} \right)^2 \quad (1.3)$$

where $r = \sqrt{x^2 + y^2}$ is radial coordinate, J_1 is the Bessel function of the first kind of order 1 and k_0 is the wave vector in a vacuum. The examples of PSF profiles obtained from the model developed by M.Born and E.Wolf using 2 different NA (1 and N=1.49 ($\lambda = 500nm, n = 1.5$)) are displayed in Figure 1.1a-c. The real PSF for comparison can be seen in Figure 1.5a.

The theoretical image resolution which is in principle achievable by the system, however, is often different from the real value due to noise in the signal and aberrations in the imaging system. This resolution estimation problem is particularly challenging in novel microscopy methods, requiring multiple image analysis steps, increasing the possibility for image distortions and artefacts. To address the resolution estimation problem, multiple methods were developed such as Fourier-ring correlation(3). However, most resolution estimation methods required multiple images and a user-defined threshold for resolution estimate.

The most recent resolution estimation technique, capable of extracting the image resolution computationally from a single image is based on the highest spatial frequency obtainable from the image termed a parameter-free resolution estimation based on image decorrelation analysis (4). This method is used to estimate the lateral resolution of light microscopy images in this thesis. The algorithm can be summarized in two steps. First, the Fourier transform of the image is computed and normalized. Then, the Fourier transform of the input image is cross-correlated in Fourier space with a normalized Fourier transform of the same image using a Pearson correlation coefficient condensed to a single value (A_i) as a correlation metric which varies between 0 and 1. Second, the process is repeated by filtering the normalized Fourier transform by a circular mask with a decreasing radius (r_i), thus gradually removing the noise contribution by removing high frequencies. The resulting image decorrelation function (r_i, A_i) is related to the spatial frequency distribution of the image and the image resolution can be estimated as a position of the local maximum (4).

The practically obtainable image resolution in optical imaging systems (while imaging biological samples) is often traded for specificity, imaging speed or better live-cell imaging performance (reduced photo-toxicity), which requires low illumination powers.

1.1.2 Fluorescence microscopy

The most common microscopy technique, widely used in biology is called fluorescence microscopy. It has the ability to image specifically labelled biomolecules by using fluorescent dyes, thus achieving a high contrast. Furthermore, fluorescence microscopy is a basis for almost all super-resolution microscopy methods, which are discussed later on in the thesis.

Fluorescence microscopy is particularly advantageous in biology, due to particularly high contrast and ability to visualize a distribution of molecules of interest within the biological object of interest varying from multicellular organisms to viruses. The technique was especially fostered by the discovery and application of easily genetically expressible fluorescent protein - green fluorescent protein (GFP)(5). The genetically modified enhanced version of the original

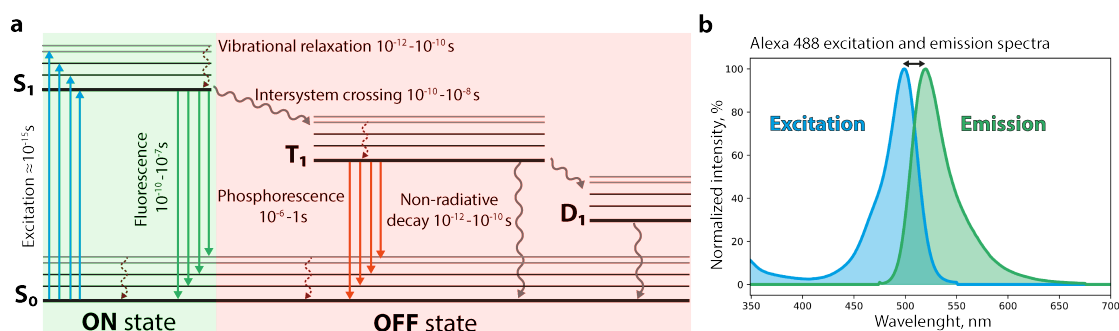


Figure 1.2 – Jablonski diagram of the main energy states of a fluorescent molecule. (a) If the molecule absorbs the photon it becomes excited from the ground singlet state S_0 to excited S_1 state. This process is very fast and typically takes (10^{-14} to 10^{-15} s). Excitation corresponds to increased energy in the electronic state of the molecule and the excitation/absorption rate is directly proportional to the laser intensity used. There are multiple ways how the energy can be dissipated. The electron can undergo intersystem conversion via change of electron spin and go into a long-lived triplet state T_1 , from which the electron goes into ground state S_0 via non-radiative decay, phosphorescence or meta-stable dark state D_1 , in which the molecule can be chemically reduced in the presence of reducing agent. Alternatively, the molecule can be photobleached and it is not able to undergo the excitation process again. (b) An example of fluorescence excitation and emission spectra. The black arrow indicated Stoke's shift from the difference in energy of the photon.

protein called (EGFP)(6) is now used as a standard biomarker to monitor gene expression and protein localization in multiple living organisms and model systems. Furthermore, the synthetic fluorescent dyes with excellent photophysical characteristics can also be used for labelling and allow for easy multi-colour imaging. However, as already discussed the intrinsic resolution, as for any light microscopy technique, is limited due to a diffraction phenomenon and equal to about 200-250 nm in a standard fluorescence microscope. We are going to further discuss the main techniques that allowed us to overcome this intrinsic limit later in the thesis.

Fluorescence microscopy is based on the photophysical process known as fluorescence. When a fluorescent molecule/atom/nanoparticle absorbs a photon, its energy is used to excite the electrons in the outer shell to higher-energy levels as the molecule goes from ground singlet state S_0 to an excited state S_1 . Typically, the excited electronic state is short-lived and the molecule quickly relaxes to a ground state, thus emitting a lower energy photon via processes called fluorescence. During this process, some of the energy is lost due to a non-radiative, typically vibrational relaxation in the excited electronic states which is visible as the shift of the emission spectrum towards longer wavelengths. This energy loss is called Stokes Shift and can be seen from the shifted emission peak. It allows the decoupling of the emission spectra from the excitation, allowing for a significant increase in the contrast of the molecule-of-interest. The broadening of the absorption and emission spectra is due to a large number of vibrational energy levels between each electronic state. As it is shown in a Jablonski diagram (Figure 1.2) there are multiple ways how the energy can be transferred from the excited electronic state.

Alternatively, several other energy transitions are available. During the non-radiative decay, the energy can be released as thermal heat via vibrational relaxation. A molecule can also go into triplet state T_1 via the inter-system crossing. During this process, the electron in the excited state changes its spin. The triplet state is typically long-lived as the transition to the ground state is forbidden by the Pauli exclusion principle due to a different electron spin. The energy from a triplet T_1 state is either emitted as phosphorescence, converted to vibrational energy via reversed intersystem crossing (ICS) or converted to chemical energy. While in triplet state – a molecule is susceptible to photo-bleaching which irreversibly changes its structure and prevents the molecule from absorbing the photon again thus diminishing its fluorescence ability. This process is fostered via the presence of molecular oxygen, which is known to be responsible for bleaching by photo-oxidation.

Furthermore, in the presence of a reducing agent organic fluorophores such as rhodamine or cyanine-based dyes group dyes can be further reduced to a meta-stable dark D_1 state, also known as anion radical state via chemical reduction(7). The anion can be then stochastically oxidized, upon the presence of the oxidizing agent, thus bringing back the molecule to its ground state. This stochastic process results in a reversible switching between ON and OFF states thus inducing the temporal fluctuations of the signal. However, this description of photo-switching is one in the plethora of switching principles discovered and gives only the basis for the further understanding of the novel fluorescence microscopy methods.

1.2 Super-resolution optical microscopy

Optical microscopy was for a long time limited to about 250 nm resolution due to diffraction and the breakage of the so-called diffraction limit seemed unrealistic. Multiple advancements in photochemistry, high-sensitivity cameras and illumination patterning techniques allowed various practical implementations of super-resolution microscopy in the early 2000s. The most common techniques are explained below together with the methods, that I used in the thesis.

The advances in the scanning probe microscopy during the twentieth century, realized the idea of a near-field scanning optical microscope (SNOM)(8), which uses a small aperture (<50 nm) which is controllably placed within a few nanometers from the sample. The small probe is used to illuminate the sample and to collect the light in the vicinity of a probe. Using this technique, it is possible to achieve the resolution of $\lambda/60$ (8). The method was further improved by increasing the scanning speeds to make it more accessible and practical but never got sufficient traction in biological applications, due to technical difficulties placing the small aperture close to the sample.

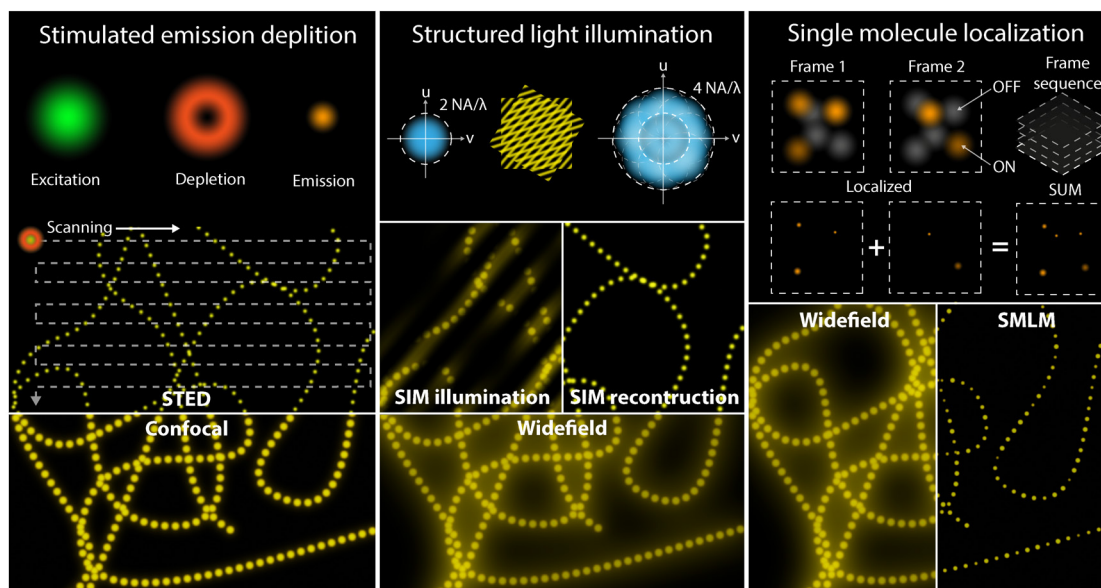


Figure 1.3 – Main super-resolution microscopy techniques. General working principle of stimulated emission depletion microscopy (STED), structured light illumination microscopy (SIM) and single molecule localization microscopy (SMLM).

1.2.1 Far-field super-resolution fluorescence microscopy

In the early 21st century, a few so-called super-resolution microscopy (SRM) techniques were proposed what were able to achieve the resolution below the diffraction limit in the far-field, thus, for the first time, giving the ability to visualize the biochemical processes in single cells at the molecular level. The fluorescence nanoscopy field was established, resulting in the 2014 Nobel Prize in Chemistry award “For the development of super-resolved fluorescence microscopy” which further boosted the development of SRM methods and their applications.

Super-resolution microscopy methods can be divided into two main categories by the means of the separation of the fluorescence signal from closely spaced molecules. The diffraction limit can be overcome by separating the emission signal either in the time domain (temporarily) or in the space domain (spatially). These methods do not break the fundamental nature of light diffraction, but rather circumvent this limit by exploiting a priori knowledge of the sample. The gain in resolution is always associated with an increased acquisition time and/or requires a complex system design that involves precise sample scanning. The main SRM methods are summarized in Figure 1.3. However, only the historically most influential techniques from a plethora of SRM methods present today are explained below, with the main focus on the methods used in this thesis.

1.2.2 Stimulated emission depletion microscopy (STED)

The methods exploring the spatial separation of fluorophores to achieve super-resolution typically use a structured illumination. The stimulated emission depletion (STED) microscopy (9; 10) is an extension of the traditional confocal scanning microscope and typically goes as an add-on to an existing system. The core working principle of the technique exploits the properties of an excited two-level system of the fluorescent molecule. The incoming photon is triggering a decay to the ground state, thus preventing the molecule from emitting a photon. To achieve this, the high-intensity light is applied to deplete the system forcing it to switch the fluorophores off. Typically, a doughnut-shaped depletion laser beam with an intensity minimum in the middle is used simultaneously with a diffraction-limited excitation beam. The molecules located in the cross-section of two beams are only detected, thus resulting in the effective excitation spot smaller than a diffraction-limited spot. The excitation and depletion lasers are scanned simultaneously by a high-speed and high-precision galvanometric scanner. The image resolution for this method is not fundamentally limited by any means but is practically limited to the STED beam laser power, the depletion cross-section, aberrations of STED beam and signal to noise (SNR) ratio. However, the method was demonstrated to achieve sub-3 nm lateral resolution on a solid-state samples(11) and routinely achieves sub 100 nm lateral resolution in fixed biological samples(12). The axial resolution can be also increased by shaping the depletion beam in 3D(12). Similarly to STED, the cis-trans isomerization found in switchable fluorescent proteins can also be used to make a STED-like recording (13), giving a name Reversible Saturable/Switchable Optically Linear (Fluorescence) Transitions (RESOLFT) to this technique. The fundamentally simple, yet effective general principle of the STED sparked multiple methods such as MINFLUX(14), that benefited from a general principle and allowed to extend the resolution of STED microscopy even further.

1.2.3 Structured light illumination microscopy (SIM)

The other method based on spatial separation of the emission signal - structured light illumination microscopy (SIM)(15) achieves a two-fold resolution improvement together with increased contrast, compared to conventional widefield microscopy. The method is based on the modified excitation path, which uses a predefined illumination pattern, typically a 2D sinusoidal pattern is used with a spacing closed to a diffraction limit. The interference pattern produced with a sample, known as a Moiré effect, results in the spatial frequencies outside the cut-off frequency due to a non-linear response. To adequately sample the spatial domain, images with different sinusoidal grating orientations and phases need to be acquired (at least 3 orientations and phases). While typically a 2D sinusoidal pattern is used, other patterns can be implemented as well. One of the most recent approaches - instant SIM (iSIM)(16), uses an all-optical, parallel scanning implementation dramatically improving the imaging speed and simplifying the imaging process at the cost of technical complexity. SIM approach is sometimes excluded from the family super-resolution methods since the 2x image resolution improvement is fundamentally limited. However, SIM is one of the most popular

super-resolution microscopy techniques for biological research as it allows to image sensitive biological samples due to low power of illumination used(17; 18) at relatively high imaging speeds, suitable to study various biological processes, such as mitochondria fission(19).

1.2.4 Single-molecule localization microscopy (SMLM)

Structured illumination modalities are based on the precise knowledge of the location of the excitation beam/pattern, thus spatially separating the fluorescence signal. The single-molecule localization microscopy (SMLM) techniques on, the other hand, work by exploiting a temporal separation of the fluorescence signal from the fluorophores that are spatially overlapped. Temporal separation is achieved by switching on only a small fraction of molecules located in a field of view (FOV). The positions of non-overlapping emitters are then computationally estimated with a precision far higher than the diffraction limit. Many frames are needed to be recorded for further data analysis in order to sample the structure properly. This group of methods is trading an increased acquisition time, required to record thousands of camera frames for a spatial resolution. The following chapter will feature the description of the general SMLM methods directly used for this thesis.

The SMLM term encompasses a plethora of photochemical/biophysical methods that are used to achieve sparsely blinking fluorophores. Historically, the first such method was introduced in 2006 by Betzig et al. (20). It uses photoactivatable genetically encoded proteins such as mEOS(21) that changes absorption spectra upon the UV illumination. By illuminating with a low UV laser intensity, only a small fraction of molecules are "turned ON" at a given time, thus giving name Photo Activated Localization Microscopy (PALM). Shortly after, Stochastic Optical Reconstitution Microscopy (STORM) proposed the use of special imaging buffers, containing a reducing agent (mercaptoethylamine (MEA) or β -mercaptoethanol (BME) that prolongs a non-fluorescent OFF state for organic cyanine and rhodamine fluorescent dyes(7). STORM also requires an efficient oxygen scavenging system to remove the oxygen from the imaging medium, since it is the main source of photo-bleaching.

Soon after the demonstration of SMLM, many other techniques were demonstrated. Here I am going to mention just a few. DNA Points Accumulation for Imaging in Nanoscale Topography(22) uses specifically designed DNA probes that stochastically bind together, producing a significant increase in fluorescence, thus blinking. The method was demonstrated to be able to achieve <1nm localization precision(23). A fundamentally similar technique was also demonstrated with genetically encoded protein tags(24). Another SMLM technique, ground-state depletion microscopy followed by individual molecular return (GSDIM)(25) is based on the concept proposed by Hell et al., where high energy laser power is used to excite the fluorophores, significantly increasing the probability they will undergo a 'spin-flip' and enter the OFF state, thus depleting the ground state. Some of the recent SMLM techniques attempt to combine the spatial and temporal separation of the fluorophores resulting in sub-1nm localization precision(14) and claiming real molecular spatial resolution. MINFLUX

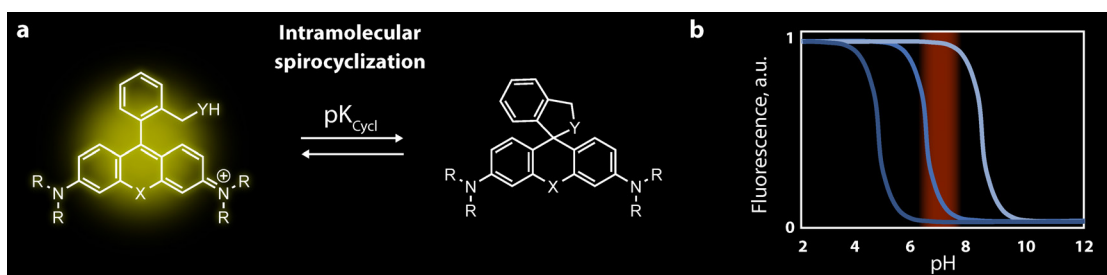


Figure 1.4 – Photochemical working mechanism of self-blinking dyes. (a) Intramolecular spirocyclization reaction between lactone and zwitterion of rhodamine-based dyes with an equilibrium constant pK_{cycl} . The reaction equilibrium between ON and OFF states is induced by intramolecular nucleophiles (Y) and the microenvironment of the dye. (b) Schematic titration curves of fluorophores with different pK_{cycl} values. pH values suitable for live-cell imaging are indicated in red. Figure was modified from(30).

demonstrated its versatility in imaging 3D structures and tracking the diffusion of single-molecules(26). However, the complexity of the system makes this approach particularly hard to access and the imaging artifacts need to be carefully evaluated(27).

The standard SMLM techniques like STORM or PALM require high laser illumination intensity or UV light, to induce blinking of fluorophores and to achieve sufficient SNR, thus performs poorly in live-cell imaging, due to extensive photodamage. DNA-PAINT, on the other hand, do not require high illumination intensity, however, the live-cell imaging is limited as a result of the high cellular toxicity of fluorescent probes or the lack of membrane permeability, though a few recent studies are tackling this problem(28). In general, most of the live-cell SMLM imaging attempts were focused on mitigating the photo-damage(29), however, none of the techniques is suitable for long term time-lapse cell imaging and the high-resolution (<100nm) SRM is typically restricted for fixed-cell imaging only.

1.2.5 Self-blinking dyes for single-molecule localization microscopy

One of the most promising approaches for live-cell imaging compatible SMLM was a development of a new class of fluorophores – termed self-blinking dyes that do not require high illumination intensity or reducing chemical agents such as thiols to induce blinking. Spontaneously blinking fluorophores based on intramolecular spirocyclization were recently demonstrated (31). The fluorescent and non-fluorescent forms interconvert via an intramolecular spirocyclization reaction and are in a thermal equilibrium state that is heavily dependent on the pH (Figure 1.4). Far-red emitting dyes are especially beneficial for live-cell imaging, due to low-phototoxicity (32). HM-SiR was demonstrated to be stable in live-cell SMLM time-lapse imaging of tubulin for up to 1h (31). Further advancements of both fluorogenic and self-blinking features of f-HM-SiR dye were shown to be useful for imaging nucleus and mitochondria in live cells with minimal phototoxicity and low intracellular background(33). Self-blinking behaviour was also observed in other fluorescent compounds, such as fluxional

Introduction

molecules, allowing the development of self-blinking dyes with reduced photobleaching(34) for SMLM time-lapses of living cells with a total exposure time up to 30 min for tracking the synaptic vesicle trafficking in live neurons or red-shifted BODIPY conjugates for imaging of lysosomes in mammalian cells(35). These few mentions are just a few selected examples of self-blinking dyes that were already demonstrated for live-cell SMLM.

The localization uncertainty in SMLM is the most commonly used metric to determine the performance of the system. Assuming the shot-noise limited signal and using a 2D Gaussian PSF model, the localization uncertainty can be described as:

$$\sigma = \frac{\sigma_a^2}{N} \left(\frac{16}{9} + \frac{8\pi\sigma_a^2 b^2}{Na^2} \right) \quad (1.4)$$

Where σ is the standard deviation of a PSF, $\sigma_a = \sigma^2 + \frac{a^2}{12}$, a is a projected camera pixel size, N is the number of photons detected and b is the average background value in photons per pixel. The formula was first proposed by Mortensen et al.(36). Localization precision is proportional to \sqrt{N} and typical lateral localization precisions while using fluorophores such as Alexa group dyes can reach 5-10nm(37) in ideal conditions.

1.2.6 3D single-molecule localization microscopy

The main advantage of SMLM compared to other SRM methods is the ability to encode the information about the PSF's position in its shape projected on the camera. The most common approach due to its simplicity is the astigmatic PSF, which can be achieved by introducing astigmatism in a system using a cylindrical(38) or adaptive optical element, such as deformable mirror(39). As a result, the ellipticity and orientation of a PSF image vary, based on its position in a regard to the image plane. This allows the localization of the molecules within an axial range of $\approx 1 \mu\text{m}$ with a localization precision down to 20 nm (38). However, localization precision is strongly dependant on the axial position of the molecule with a regard to an image plane. By using a dual-objective approach to collect more photons, axial localization precision up to 8 nm can be achieved(40).

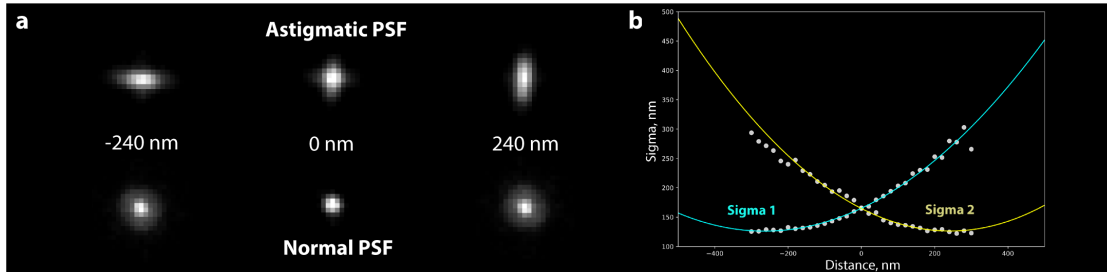


Figure 1.5 – Astigmatism-based 3D single-molecule localization microscopy imaging (a) A comparison between normal and astigmatic experimental PSFs at different heights. (b) A calibration curve of astigmatic PSF's σ values in x (σ_1) and in y (σ_2).

Deformable mirrors can also be advantageous for astigmatism-based imaging, thus enabling aberration-free imaging at high depths and with high-NA oil-immersion objectives by correcting for aberrations from refraction index mismatch(39). The astigmatism-based SMLM approach is very stable and straightforward to implement, whereas the higher precision of this method at the cost of the increased complexity of the optical setup to achieve excellent detection efficiency and mechanical stability. The axial SMLM range can be expanded with a custom-designed PSF's such as double-helix(41), self-bending(42), saddle-point(43) or tetrapod(44) PSFs designed to expand the axial range up to 5 μm . To make 3D SMLM more flexible, computational strategies such as Zernike Optimized Localization Approach (ZOLA) are being employed to achieve the optimal resolution within a tunable axial range(45). Other approaches to retrieve axial PSF position use methods such as single-photon interferometric SMLM (iPALM)(46) or direct optical nanoscopy with axially localized detection (DONALD)(47), that can also achieve the axial localization precision down to 10 nm. However, all of these approaches require optimal imaging conditions to achieve sparse blinking and excellent fluorophore brightness, requiring high illumination intensities and thus mostly limiting these techniques to a fixed-sample, a few notable exceptions demonstrating a proof-of-principle live-cell imaging capabilities(48).

1.2.7 Super-resolution optical fluctuation imaging (SOFI)

To provide microscopists with SRM tools for the samples with high-fluorophore density imaged with low-illumination power (live-cell imaging compatible) computational approaches analysing the spatiotemporal fluctuations of the fluorophores were developed. Historically, the first SRM method exploiting the statistical analysis of the fluorescence signal of fluctuating fluorophores was super-resolution optical fluctuation imaging (SOFI)(49). Alongside standard SMLM approaches, SOFI was used in this thesis as an approach for high-density samples, that can be easily implemented on a widefield setup and used within a broad range of fluorescent probes.

SOFI method relies on the computation of spatiotemporal cross-cumulants of the sequence from blinking (fluctuating) fluorophores. It can be applied to any fluctuating signal as long as three main conditions are fulfilled:

- The signal fluctuations should originate from two distinct states (i.e. ON and OFF)
- The signal fluctuations should be stochastic and independent. (i.e. laser illumination should be constant without any modulation of the fluorescence signal)
- The Nyquist sampling criterion has to be fulfilled (i.e. pixel size of the camera should be below 125 nm)

If these conditions are fulfilled, the fluorescence signal from the sequence of fluctuating fluorophores is only correlated in time and space with itself. This assumption allows making use of

Introduction

the additivity property of statistical cumulants, meaning that the signal from each fluorophore can be processed independently and making it possible to increase the resolution of the signal in space by a factor of \sqrt{n} , where n is the order of cumulants. By further deconvolving the image with an appropriate deconvolution algorithm, the total resolution improvement of n (n is the order of cumulants) can be achieved(30). SOFI can be straightforwardly extended to 3D while performing a simultaneous volumetric multiplane recording of the sample by using beamsplitters(50) and computing the cumulants in the axial dimension as well.

Given signal from a time sequence of N blinking fluorophores, the intensity that is detected on the camera can be described as:

$$I(\mathbf{x}, t) = \sum_i^N \varepsilon_i U(\mathbf{x} - \mathbf{x}_i) s_i(t) + b(\mathbf{x}, t) \quad (1.5)$$

where ε_i is the molecular brightness, $U(\mathbf{x})$ is the point-spread function, \mathbf{x}_i is the position of the PSF, $s_i(t) \in [0, 1]$ describes the switching behaviour of the fluorophore between the on-state (1) and the off-state (0) over time, $b(\mathbf{x})$ is the constant background signal together with an uncorrelated noise.

By using the semi-invariance and additivity properties of the statistical cumulants, we can rewrite the expression for the n^{th} order cumulant with zero-time lag as:

$$\kappa_n(\mathbf{x}) = \sum_i^N \varepsilon_i^n U^n(\mathbf{x} - \mathbf{x}_i) \kappa_n\{s_i(t)\} + \kappa_n\{b(\mathbf{x})\} \quad (1.6)$$

Where $\kappa_n\{b(\mathbf{x})\}$ is the cumulant, which can be eliminated if the background and noise level stays constant, what is typical for most of the experiments. The cumulant of the blinking statistics $\kappa_n\{s_i(t)\}$ is a Bernoulli distribution with probability $p = \frac{t_{on}}{t_{on} + t_{off}}$ which is also known as an ON-time ratio of the fluorophore. Finally, the cumulant of the blinking statistics can be approximated by n^{th} order polynomial function of the ON-time ratio $f_n(\rho) = (1 - \rho) \partial f_n \partial \rho$ which leads to the final equation for SOFI cumulants:

$$\kappa_n(\mathbf{x}) = \varepsilon^n f_n(\rho) \sum_i^N \varepsilon_i^n U^n(\mathbf{x} - \mathbf{x}_i) \quad (1.7)$$

The resolution improvement of the n^{th} order SOFI image comes from the raising of the system's point spread function to the n^{th} power. Applying a deconvolution or a reweighting scheme in the Fourier domain, the final resolution can be improved to the n^{th} order of the cumulant (51; 52). However, the inhomogeneities in the molecular brightness often lead to a local increase of the SOFI signal which quickly saturates the image. To mitigate this problem, deconvolution of the cumulant followed by a linearization step was introduced(52). The

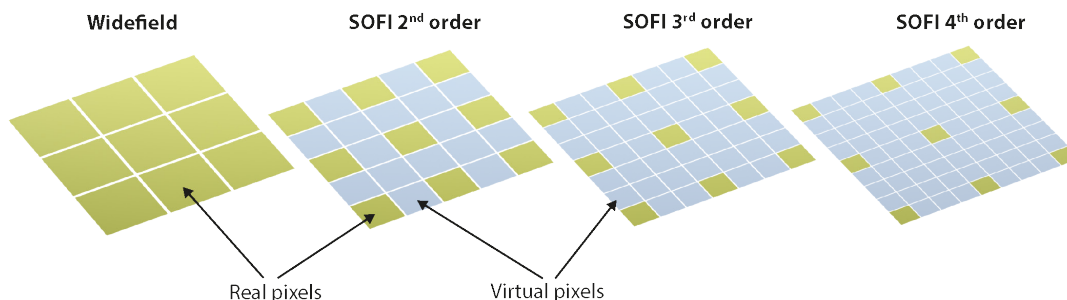


Figure 1.6 – Schematics of SOFI cumulant calculation principle. Pixel maps from Widefield (left) to 4th order SOFI (right) demonstrating the cross-cumulant analysis, which creates the virtual pixels (blue) in between the real pixels (green).

linearization of the brightness response is calculated by taking n^{th} root of the deconvolved image and was successfully demonstrated for 2D and 3D SOFI cases. In general, there is no fundamental limit for the SOFI resolution. However, in practice for high SOFI orders, SNR of the images decreases due to limitations in SNR of the image sequence and the number of frames recorded.

SOFI was demonstrated to be feasible with many different samples and fluorophores, but the high order SOFI imaging ($>3^{rd}$ order) is rarely achieved. The 25^{th} order SOFI imaging was demonstrated in the original proof-of-principle SOFI publication by using isolated quantum dots, however, this was not demonstrated to be feasible in imaging biological structures because of cusp artefacts, that were identified in higher-order cumulant analysis of quantum dot labelled cells due to significant heterogeneities in the photophysics of these fluorophores(53). Recently, the number of papers from our group demonstrated the feasibility of high-order SOFI by using self-blinking dyes with a high on/off ratio, allowing up to 5^{th} order SOFI(30) to resolve the biological structures in fixed cells and showing promise for live cell imaging as well. The self-blinking dyes combined with SOFI are going to be discussed in detail later in the thesis.

Alongside the development of SOFI, multiple other techniques taking the advantage of the temporal fluctuations in the fluorescence signal were demonstrated. All these approaches are generating super-resolution images directly from image stacks, without a need to localize the fluorophores. Approaches like deconSTORM(54), which reconstructs super-resolution images by averaging extensively deconvolved images of sub-populations of fluorophores or 3B(55) - which uses Bayesian analysis, or SRRF(56), which calculates the degree of local gradient convergence across the entire frame, on a sub-pixel basis, were demonstrated. Most of these methods demonstrate the ability of fast and minimally phototoxic live-cell imaging(57; 58).

In a plethora of computational super-resolution microscopy approaches, the problem of image artefacts becomes increasingly severe. It is especially crucial for approaches based on deep-neural networks(59; 60) that are based on a priori knowledge to reconstruct the

super-resolution images or localize emitters in three dimensions. Approaches for SMLM such as Haar wavelet kernel (HAWK)(61) in a combination with standard SMLM algorithms(62), were also developed to mitigate the artefacts in high-density single-molecule localization cases. Image artefacts were observed in analysed in almost all super-resolution modalities, including STED(63), SIM(64), SMLM(65), SOFI(53) facilitating a further need for a correlative imaging approaches, where the same sample can be imaged with fundamentally different methods with preferably higher resolution, allowing to get meaningful comparisons, to get multifunctional information and to achieve artefact-free imaging. The following part of the thesis is going to focus on scanning probe microscopy techniques that are highly compatible with super-resolution imaging modalities and can usually be straightforwardly implemented in an optical microscopy setup.

1.3 Scanning probe microscopy and sensing

Before the super-resolution optical methods evolved a single-molecule imaging capability, the scanning probe microscopy (SPM) holds a huge promise for biological research because of its ability to obtain the three-dimensional topographical images of the sample at sub-nanometer axial and lateral resolution. While fluorescence SRM techniques excel at selective imaging of the protein of interest, SPM methods can provide a nanometer-scale topographical and structural information about the sample. Here I summarize the basics of SPM imaging and single-molecule sensing.

1.3.1 Atomic force microscopy

SPM modalities such as atomic-force microscopy (AFM) can perform imaging in liquid environments in contrast with scanning-electron microscopy (SEM), which can image in a vacuum only. In addition to the topographical information of the sample, SPM has a unique ability to provide information about the various physical sample properties such as stiffness, surface charge, surface magnetism, temperature, etc. SPM can also be used to manipulate the biomaterial and apply predefined forces on soft biological samples and living cells. In contrast to optical methods, only "outside" imaging of biological samples is possible, given the nature of the technique, and in-cell SPM imaging remains elusive. In the following paragraphs of the thesis, the basic principles of SPM and applications for live-cell imaging are going to be discussed.

The atomic force microscope (AFM) was a continuation of a scanning-tunnelling microscope, demonstrated in 1981(66), which was capable of imaging conductive samples in a vacuum only. The first publication of the atomic force microscopy (AFM), capable of imaging dielectric samples in various conditions, including liquid environments(67), led to the development of various SPM modalities. The atomic force microscope works by sensing the surface via a sharp tip at the end of a cantilever which is positioned with a fast piezo. The actual height information is gained by measuring the intensity of a laser beam, which reflects from a can-

tilted to a quadrant photodiode (QPD) sensor. The imaging is typically performed, either by moving the sample or the scanning head, which holds the cantilever. Since the demonstration of the general principle of the method, it quickly became commercially available and the development of new AFM systems was focused on increasing the imaging speed and reducing the tip-sample interaction forces to image soft samples, such as biological cells.

The first images of live cells were demonstrated in 1990(68) and the method was not suitable for imaging soft cell membrane, without disrupting it, so multiple non-contact AFM scanning modes were developed to further reduce tip-sample interaction force. The latest high-speed AFM developments of the amplitude-modulation mode proved to be a versatile tool to study samples with extremely low interaction forces and were shown to visualize molecular processes such as actin-myosin complex dynamics(69) or lately, the self-assembly of centriolar scaffold protein, by using a high-speed photothermal off-resonance tapping mode(70). But even at these extremely low contact forces (50-80 pN) the AFM based imaging of living cells for extended periods of time remains challenging to the present day.

1.3.2 Scanning ion-conductance microscopy

Originally, scanning ion-conductance microscopy (SICM) was developed to image the topography of nonconducting surfaces covered with electrolytes (71). The principle of this technique relies on the flow of ions through the aperture of the glass pipette. The flow could be blocked at short distances between the probe and the surface, thus limiting the ion conductance. The magnitude of the ion currents is determined by the combination of the pipette resistance and the access resistance between the pipette tip and the sample surface. Since the pipette is never in direct contact with a surface it makes SICM truly a non-contact surface scanning method, suitable to image the most sensitive live samples, while performing significantly better in live-cell imaging with minimal volume distortions (Figure 1.7). Since its invention in 1989, SICM was used to visualize various complex biological objects while keeping them viable and active during extended periods of time. SICM was used to image multiple types of living cells, showing the dynamics of sensitive cell types such as living neurons(72), dynamics of microscopic microvilli(73) or even proteins in cell membranes(74) at the nanometer scale. A hopping mode was a particularly important achievement for SICM development, allowing to reduce the pipette-sample contact events to a bare minimum and opening the doors for imaging extremely high aspect ratio structures such as drosophila eye filaments(72).

In regard to image resolution, scanning probe microscopy is not diffraction-limited, but rather directly dependant on the shape of the probe used for sensing. As for light microscopy, the image is the product of the convolution of the true object and the microscope's PSE. For SPM the convolution is performed between the 3D shape of the imaging probe and the sample. The image formation principles and deconvolution strategies were extensively studied for AFM using experimental and finite element modelling approaches(76), however, the image formation principle in SICM remained open for debate for a long time due to a complex

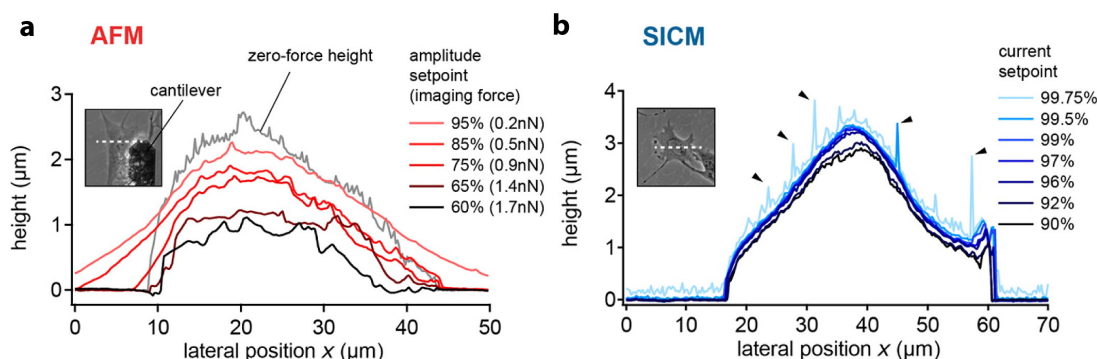


Figure 1.7 – Comparison of live cell imaging for AFM and SICM. (a) AFM height profiles of a live mouse embryonic fibroblast (MEF) for different tapping mode amplitude setpoints and the corresponding estimated imaging forces. The zero-force height (gray) was obtained in the force mapping mode. (b) SICM height profiles of a live MEF cell for different ion current setpoints (relative to the free ion current). The figure obtained from (75) and reproduced with permission.

pipette-sample interaction. A recent study demonstrated, that the full width half maximum (FWHM) of SICM point-spread function (sPSF) is approximately equal to $3r_i$, where r_i is the radius of the pipette used and this relation is kept in various imaging modes leading to a lateral resolution of approximately $3r_i$ (77). With a fabrication of small glass nanocapillaries and flat samples, such as membrane protein monolayers – the lateral resolution up to 3-6 nm was demonstrated(74). However, the model for the axial resolution is not well established and typically is dependent on the current set-point and the pipette size(78). Nevertheless, SICM can regularly resolve the thickness of a lipid bilayers(79) suggesting the axial precision well below 4 nm. However, the resolution of SICM is strongly dependant on multiple parameters such as surface charge, the conductivity of a solution, pipette size and pipette 3D shape.

1.3.3 Correlative scanning probe and fluorescence microscopy

As already mentioned before, the convenience of the scanning probe imaging methods lies in their ability to be straightforwardly implemented on inverted optical microscopes, thus enabling multi-mode correlative imaging both with SPM and light-microscopy modalities. This approach is widely used and a number of studies benefited from correlative SPM and light microscopy imaging. The particular interest for modern biology is a combination of the fluorescence super-resolution microscopy techniques with scanning probe modalities, that are capable of imaging soft samples in their native environment, ideally in conditions suitable for live-sample imaging. The task of live-cell imaging is particularly challenging because the negative effects of both (light microscopy and SPM) modalities need to be balanced and carefully optimized to maintain the minimal physical and photophysical damage for extended periods of time, thus keeping the imaging quality sufficiently high to resolve the structures of interest. SICM is particularly advantageous for this purpose, due to low probe-sample interac-

1.3. Scanning probe microscopy and sensing

tion forces and it was already demonstrated to be superior to AFM for a live-cell imaging(80) as well as to produce images with minimal topographical distortions. However, few studies where fluorescence methods are combined with the SICM technique were published so far.

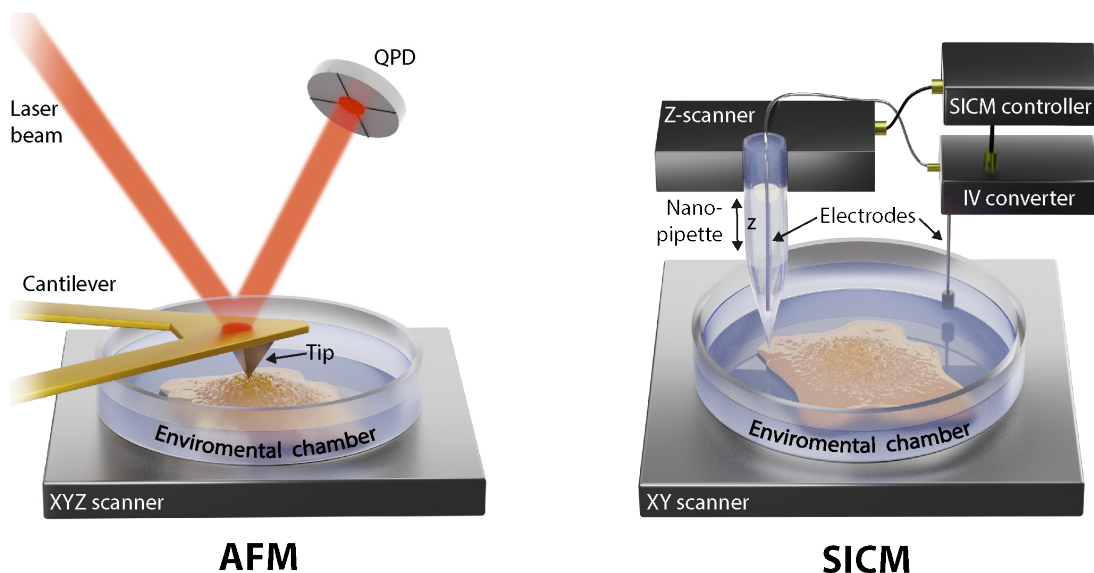


Figure 1.8 – Schematics of AFM and SICM. Atomic force microscopy (AFM) works by scanning the surface topography with an ultra-sharp tip. The feedback about the tip position is achieved by reading the reflection signal from the laser beam reflecting from a miniature cantilever. Scanning can be performed in various environments, thus enabling live-cell imaging. Scanning ion-conductance microscopy (SICM) works by scanning the surface with a sharp glass pipette. The feedback signal is the measured ionic current between the electrode in a nanocapillary and a bulk electrode in a solution. The current decreases then the pipette is close to the surface. The main benefit of the method is a truly non-contact measurement, allowing to image sensitive samples for extended periods of time.

Multiple studies employing AFM for ultraprecise topographical imaging were demonstrated together with high and super-resolution fluorescence microscopy techniques for correlative imaging. AFM was combined with a scanning confocal microscope(81), SIM(82), STED(63), STORM(83; 84) and PALM(85). However, the correlative SICM was used just in a few studies, likely due to limited availability of the technique. The advantages that SICM can provide for correlative live-cell imaging were not fully explored. SICM was combined with fluorescence confocal microscopy to study the dynamics of endocytic pits(86) and recently SICM was demonstrated together with STED microscopy in a proof of principle paper(87). Correlative SICM and SOFI will be discussed later in the thesis, by demonstrating the possibility to retrieve structural and functional information of cellular cytoskeleton at a single-cell level. However, the SICM is not limited to topographical imaging only and it can be used for nanopore-based single-molecule detection as well.

1.3.4 Probes for scanning ion-conductance microscopy

The fragile borosilicate/quartz nanocapillary probes used in SICM frequently is a limiting factor for the resolution and throughput. However, the solid-state nanopore can be employed for a different application – DNA sensing. The application of SICM for DNA spectroscopy by using ultra-small nanocapillaries is demonstrated in the 4th chapter of this thesis. The idea of electrical sensing of analytes using small pores and ionic-current detection was first patented in the middle of the 20th century(88). The molecular sensing with nanopores is achieved when a small molecule or nanoparticle (DNA, protein, etc.) passes through the pore due to the electrical bias applied between 2 chambers. During the moment, then the molecule (analyte) translocates through the pore, the ionic current is reduced and a current drop is registered. By analysing the amplitude and the length of the drop, certain parameters of the analyte, such as size, length or charge can be obtained.

1.4 Introduction to solid-state nanopore sensing

The field of nanopore-based sensing is the basis of the next-generation DNA sequencing techniques. By using bacterial porins, such as alpha hemolysin(89) or MspA(90), it is possible to read the DNA sequences when the single strand of DNA is passing through a specifically engineered biological pore. Each base corresponds to a slightly different current blockade which can be detected using precise current amplifiers(89). However, biological pores are also sensitive to the environment and difficult to work with, thus solid-state nanopores are being developed as a logical step towards making the high-throughput DNA sensing more accessible(91). So far, the solid-state nanopores failed to demonstrate a single-nucleotide detection in a DNA strand, due to fast translocation speeds of 50–50000 nt ms^{-1} , limiting current resolution. One of the platforms for DNA translocations are glass nanocapillaries (92). Glass nanocapillaries are easily manufactured and simple to handle, thus at the same time provide low capacitance for low-noise current measurements(93). Glass nanocapillaries were used in multiple nanopore experiments to detect DNA translocations(92), DNA barcodes(94), to study DNA-protein interactions(95) or even for digital DNA data storage applications(96). Most of the studies are using nanocapillaries that are immobilized in microfluidic chips that are suitable for free-translocations only. Controlled translocations' platform using nanocapillaries was demonstrated with optical tweezers(95), by using a DNA immobilized via biotin to the polymer bead, which was precisely positioned using an optical trap. Other implementations demonstrated precisely positioned solid-state probes and complex nanofluidic designs, which are further described in this thorough review(97).

1.5 Thesis structure

The following chapters of this thesis represent the journey through modern single-molecule biophysics to gain additional knowledge by combining multiple single-molecule detection

techniques. Important to note here is that the first, third and fourth chapters were done in close collaboration with PhD student **Samuel Mendes Leitao** from a Laboratory for Bio- and Nano- Instrumentation led by Prof. Georg Fantner, who works on numerous improvements on the SICM design. The first chapter presents the combined SICM and SOFI approach, allowing us to image biological samples well beyond the diffraction limit of light with topographical information retrieved by SICM. The second chapter shows the alternative approach for multi-plane 3D super-resolution microscopy based on remote focusing with adaptive optics. The third chapter slightly shifts the focus to the nanofluidics, where a high-throughput nanocapillary filling approach is demonstrated, which was crucial for the next chapter. The fourth chapter discusses a SICM application, for scanning surface-immobilized DNA, thus demonstrating a new modality of SICM and enabling ultra-precise conductance measurements of single DNA molecules.

2 Correlative 3D microscopy of single cells using super-resolution and scanning ion-conductance microscopy

The following chapter is based on the of the following publication:

Vytautas Navikas¹, Samuel M. Leita², Kristin S. Grussmayer¹, Adrien Descloux¹, Barney Drake², Klaus Yserentant³, Philipp Werther⁴, Dirk-Peter Herten³, Richard Wombacher^{4,5}, Aleksandra Radenovic¹, Georg E. Fantner². **Correlative 3D microscopy of single cells using super-resolution and scanning ion-conductance microscopy**, Nature Communications, 2021.

V.N. and S.L. equally contributed to the paper by conceiving and refining general idea and writing the final manuscript with input from all the authors. V.N. prepared the cell samples, performed all optical imaging experiments and correlative SOFI image data analysis and the final data visualization. B.D and S.L. built the SICM setup, S.L. performed the SICM imaging and SICM data processing. Simultaneous SICM/SOFI imaging was performed by V.N. and S.L. K.G. contributed by creating and adapting labelling protocols. A.D. adapted and improved the existing SOFI analysis code. K.Y. and P.W. synthesized and provided f-HM-SiR-phalloidin conjugate. D.-P.H., R.W., A.R and G.E.F. supervised the work.

¹Laboratory of Nanoscale Biology, Institute of Bioengineering, School of Engineering, Swiss Federal Institute of Technology Lausanne (EPFL), Lausanne, Switzerland.

²Laboratory for Bio- and Nano-Instrumentation, Institute of Bioengineering, School of Engineering, Swiss Federal Institute of Technology Lausanne (EPFL), Lausanne, Switzerland. ³College of Medical and Dental Sciences, Medical School and School of Chemistry, University of Birmingham, Birmingham, United Kingdom. ⁴Institute of Pharmacy and Molecular Biotechnology, Heidelberg University, Heidelberg, Germany. ⁵Department of Chemical Biology, Max Planck Institute for Medical Research, Heidelberg, Germany. ⁶These authors contributed to manuscript equally: Vytautas Navikas, Samuel M. Leita.

2.1 Abstract

High-resolution live-cell imaging is necessary to study complex biological phenomena. Modern fluorescence microscopy methods are increasingly combined with complementary, label-free techniques to put the fluorescence information into the cellular context. The most common high-resolution imaging approaches used in combination with fluorescence imaging are electron microscopy and atomic-force microscopy (AFM), originally developed for solid-state material characterization. AFM routinely resolves atomic steps, however on soft biological samples, the forces between the tip and the sample deform the fragile membrane, thereby distorting the otherwise high axial resolution of the technique. Here we present scanning ion-conductance microscopy (SICM) as an alternative approach for topographical imaging of soft biological samples, preserving high axial resolution on cells. SICM is complemented with live-cell compatible super-resolution optical fluctuation imaging (SOFI). To demonstrate the capabilities of our method we show correlative 3D cellular maps with SOFI implementation in both 2D and 3D with self-blinking dyes for two-color high-order SOFI imaging. Finally, we employ correlative SICM/SOFI microscopy for visualizing actin dynamics in live COS-7 cells with subdiffraction resolution.

2.2 Introduction

Imaging living cells *in vitro* is crucial in deciphering the biochemical mechanisms underlying complex cellular activity such as cell motility(98), differentiation(99), membrane trafficking(100), and cell-to-cell communication(101). Our knowledge about the ultra-structure of a cell is almost exclusively derived from high-resolution electron microscopy (EM) on fixed and sectioned cells. Modern EM techniques can routinely reach sub-nm resolution and even provide the atomic structures of macromolecular complexes such as ribosomes(102) or lately even whole viruses(103). The function of the structures is typically inferred from the presence of specific molecules of interest by performing targeted expression or immunolabelling, followed by fluorescence microscopy techniques thus resulting in correlative light and electron microscopy (CLEM)(104). Axial information can be obtained from EM images through serial sectioning(105), however obtaining unperturbed 3D information about the shape of the cell membrane remains difficult and low throughput. The portfolio of fluorescence imaging techniques has been expanded with multiple so-called super-resolution microscopy techniques, that circumvent the traditional diffraction limit of optical microscopy(106). Many of these techniques trade-off temporal resolution for lateral resolution, and often require high light intensities causing light-induced cell damage in live cells(107). An approach named super-resolution optical fluctuation imaging (SOFI)(108) was developed to mitigate the negative phototoxic effects of long-term imaging by increasing acquisition speeds. SOFI relies on stochastic temporal fluctuations of the signal in independently blinking emitters and is less sensitive to varying fluorophore density and different blinking conditions, compared to localization microscopy approaches(109). SOFI was demonstrated as a powerful imaging method which goes well beyond the diffraction limit and can be extended for live-cell 3D imaging(110)

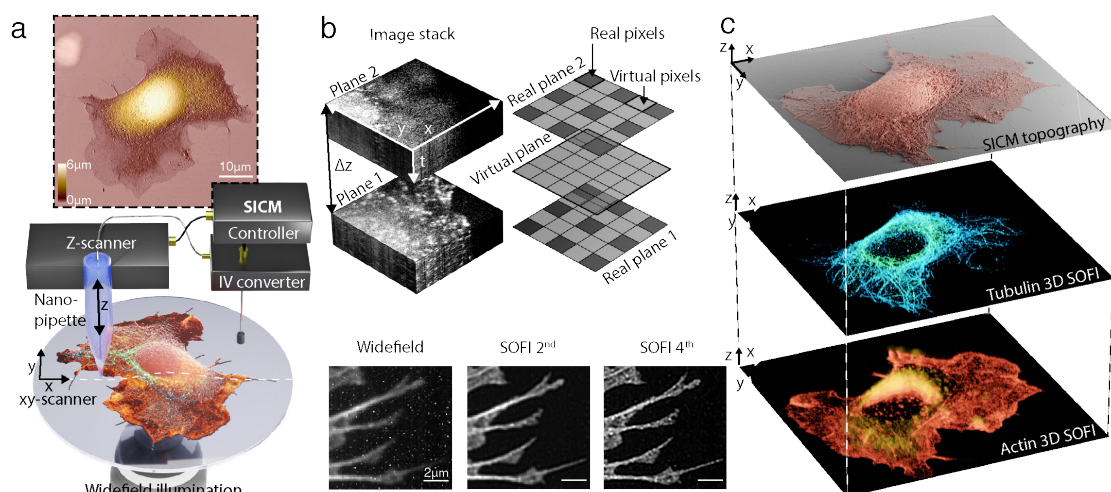


Figure 2.1 – Combined scanning ion conductance microscopy (SICM) and super-resolution optical fluctuation imaging (SOFI) for three-dimensional topography-fluorescence correlative imaging. (a) Schematic illustration of the SICM-SOFI setup. In SICM, a current is generated through a nanopipette and modulated as a function of the z-position. The image generated reflects a three-dimensional topographical view of the surface at high lateral and axial resolution (top panel). The lateral resolution in SICM ranges from 150 nm to 30 nm and the axial resolution in the 10 nm range (Figure 2.13). Since the scanning head is mounted on top of the widefield setup, fluorescence imaging can be performed simultaneously. (b) Conceptual visualization of the SOFI principle. The recorded image stack, containing time traces of independently fluctuating fluorophores is used for analysis. A SOFI image is generated by computing cross-cumulants, creating virtual pixels between adjacent real pixels. The cross-cumulant computation principle can be applied in the axial direction as well if multiple sample planes are simultaneously acquired. For the n th order SOFI image, the cumulant PSF volume is raised to n th power thus giving the resolution improvement of a factor of $\sqrt[n]{n}$. The inset images of the actin structure at the bottom of the (b) panel represent a standard deviation of the image stack (widefield), 2nd and 4th order of linearized SOFI images with corresponding lateral resolution values estimated with an image decorrelation-analysis algorithm of 420 nm, 194 nm, and 93 nm, respectively. (c) Schematics of correlative SICM and two-color 3D SOFI imaging.

or combined with self-blinking dyes(30), simplifying the image acquisition pipeline. On the other hand, scanning probe microscopy (SPM) can obtain nanometer resolution images of the 3D surface of unlabeled living cells in its physiological environment(111). It has been proven as a versatile tool for biological imaging, and is often combined with fluorescence microscopy methods(112). The most commonly used SPM technique, atomic-force microscopy (AFM), enables the study of the mechanobiology of fixed or living cells(113), to image biological membranes(114) and even track the dynamics of molecular assembly processes(115). Label-free AFM methods combined with label-specific super-resolution fluorescence microscopy tools can provide maps of single-cells in unprecedented detail not only in fixed, but also in living samples(116; 82). AFM relies on the direct physical interaction with a sample, which usu-

ally deforms sensitive biological specimens and causes height artifacts in live-cell imaging(80). To perform truly non-contact imaging in physiological conditions a scanning modality based on ionic current sensing was developed a few decades ago(71) and was significantly improved with further developments for robust live-cell imaging(72). Scanning-ion conductance microscopy (SICM) relies on the ionic current flowing through a nanocapillary in electrolyte. The ionic current strongly depends on the presence of a surface in the vicinity of the probe tip, hence the nanocapillary can be used as a nanoscale proximity sensor, without ever touching the sample. The sensing distance where the current drops is dependent on the pipette's pore diameter(117). SICM is therefore suitable for sensitive biological systems such as neurons, even with high-aspect ratio topographies with the invention of the hopping mode scanning modality(72). The use of combined SICM and stimulated emission depletion microscopy for topographical imaging was demonstrated to provide additional information about the structure of cytoskeletal components(87), but lacked the ability to perform the complementary correlative recording on the same setup. Here we present a combined SICM-SOFI approach for *in-situ*, correlative single-cell imaging.

2.3 Results

Our pipeline for a combined SICM/SOFI approach is based on correlative imaging with a home-built high speed SICM setup (Fig. 1a), operating in hopping mode(72), combined with a SOFI workflow for either two- or three-dimensional sample imaging. SOFI increases the resolution of the widefield microscope by using the statistical information from stochastic intensity fluctuations and calculating the cumulants of the intensities between the individual pixels and image planes for resolution improvement in 2D and 3D respectively(118), (Figure 2.1b). The lateral resolution of SICM is approximately equal to three times the radius of the pipette(117). In this work, we exclusively use nanocapillaries with a radius of 40-60 nm, which results in a lateral resolution comparable to SOFI. For increased resolution, glass nanocapillaries smaller than 10 nm radius can be fabricated(119). Such nanocapillaries are however highly susceptible to clogging and are therefore not suitable for long-term measurements.

To get label-specific information about the cytoskeletal structure of the cells, we performed SOFI with both traditional and self-blinking fluorescent dyes. Self-blinking dyes enable high-order SOFI analysis, that can be applied to various densities of temporally fluctuating fluorophores in order to gain spatial resolution and improve optical sectioning(30). SOFI has the advantage of tolerating higher labelling densities(109) compared to single-molecule localization microscopy, thus decreasing the acquisition time required to the order of 10 s of seconds per SOFI frame(120). Subsequently, we correlated SICM data with two-color 2D and 3D SOFI images, that provided high-resolution single-cell maps showing a distribution of the actin and tubulin cytoskeletal proteins ((Figure 2.1c)).

Before combining the two techniques within one instrument, we tested the 2D SOFI approach with self-blinking dyes on a dedicated setup (Figure 2.2a-b). We achieved up to 72 ± 3 nm

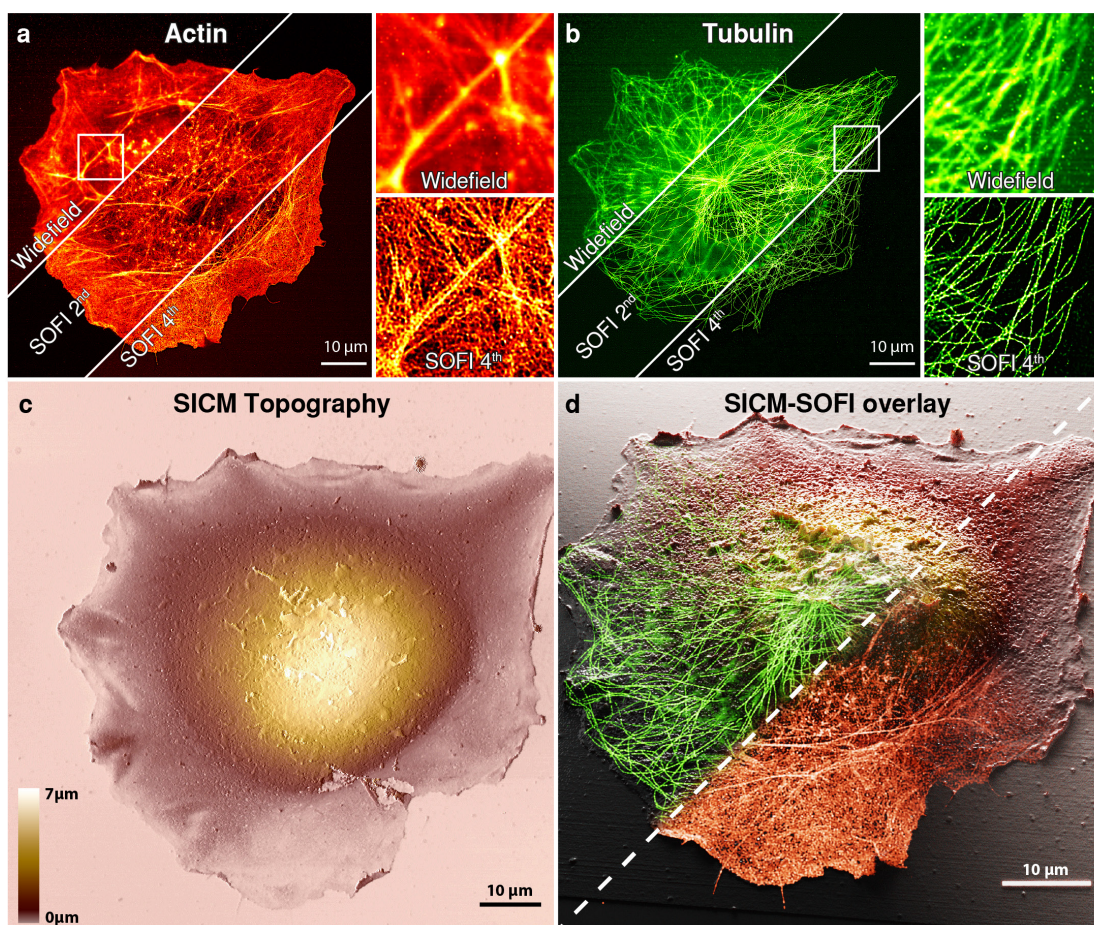


Figure 2.2 – Correlative 2D SICM-SOFI imaging cytoskeletal components of a fixed COS-7 cell. (a) Large field of view ($100\ \mu\text{m} \times 100\ \mu\text{m}$) 2D SOFI imaging of filamentous actin labeled with a phalloidin-f-HM-SiR self-blinking dye conjugate. (b) Subsequently, immunostained tubulin labelled with the self-blinking Abberior FLIP-565 dye was imaged. $10\ \mu\text{m} \times 10\ \mu\text{m}$ zoom-ins of the standard deviation of the image stacks (widefield) and 4th order SOFI images are shown for (a) and (b) panels. 635 nm flat-fielded laser excitation was used for imaging f-HM-SiR and a 561 nm laser line for Abberior FLIP-565. Imaging was performed in a 25% glycerol and PBS mixture at pH = 8. (c) Corresponding topographical SICM image of the same cell acquired on a dedicated SICM setup. 1024×1024 pixels image (78nm pixel size), acquired at a pixel acquisition rate of 200 Hz with a hopping height of $5\ \mu\text{m}$. (d) 3D rendering of a correlative SICM-SOFI overlay. The transparency gradients of tubulin and actin channels are shown as a 2D plane, while topographical SICM information is used for the height representation in the Blender 3D software. The overlay shows that actin is distributed within the boundary of the cell while tubulin displays the canonical cytoskeletal structure. This figure is representative of more than 10 correlative 2D SICM/SOFI single-cell images obtained from at least two independent experiments.

resolution for 4th order SOFI images for microtubules labelled with the commercially available Abberior FLIP-565 dye and $101 \pm 9\ \text{nm}$ for actin labelled with custom synthesized f-HM-

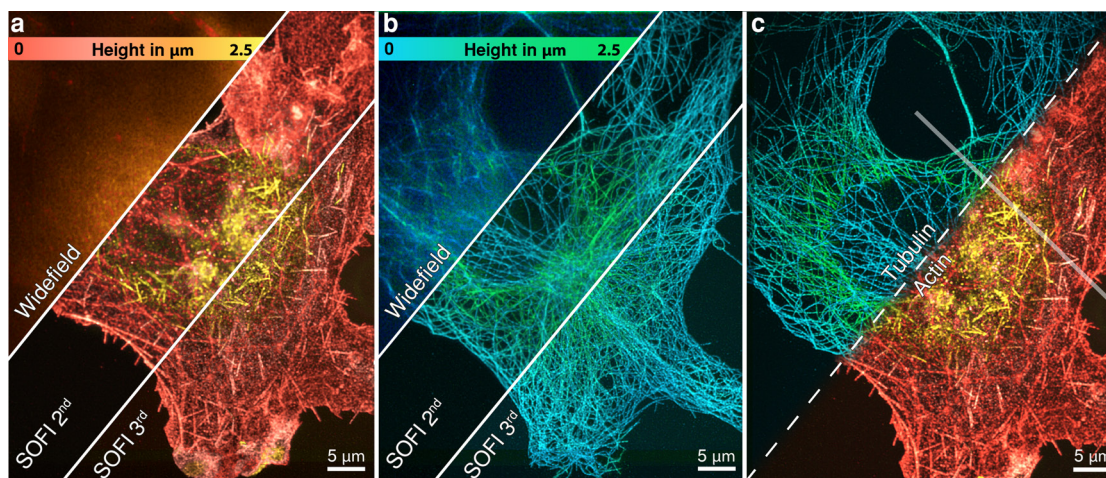


Figure 2.3 – Multi-plane 3D SOFI imaging of cytoskeletal components in a fixed COS-7 cell. (a) 3D SOFI imaging of filamentous actin labeled with phalloidin conjugated to Alexa-647 and tubulin (b) labelled with the Abberior FLIP-565 self-blinking dye. A sample volume of $2.45 \mu\text{m} \times 65 \mu\text{m} \times 55 \mu\text{m}$ was recorded with 8 equally spaced physical planes, resulting in 22 image planes after 3rd order SOFI processing. Flat-fielded 635 nm and 532 nm laser lines were used for the excitation. Alexa-647 dye was imaged in ROXS imaging buffer with 10 mM MEA, while the Abberior FLIP-565 dye was imaged in a 50% glycerol and PBS solution at pH = 7.5. Height is represented in color scales displayed for each channel. (c) Co-registered 3D 3rd order SOFI volumes of tubulin and filamentous actin. Co-registration was performed based on brightfield microscopy images acquired after recording each fluorescence channel. Semi-transparent line shows the cross-sections displayed in Figure 2.5a-b. This figure is representative of more than 10 two-color 3D SOFI images obtained from at least two independent experiments.

SiR(121), compared to a widefield resolution of $437 \pm 106 \text{ nm}$ and $480 \pm 30 \text{ nm}$ (mean \pm s.d., $N=8$ images for SOFI 2D resolution measurements) respectively. Resolution was estimated using an image decorrelation analysis algorithm(4), which allowed us to estimate the resolution image-wise. The calculated values agreed with theoretical values expected from SOFI analysis (Figure 2.14). Low-intensity (275 W/cm^2 of 632 nm, 680 W/cm^2 for 561 nm) illumination was used, resulting in minimal bleaching and long bleaching lifetimes of $406 \pm 168 \text{ s}$ for Abberior FLIP-565 and $625 \pm 130 \text{ s}$ for fHM-SiR (mean \pm s.d, $N=8$ images for SOFI 2D bleaching measurements) (Figure 2.15). Labelling density for both dyes was optimized for SOFI imaging, however both datasets were also processed with SMLM software(62), which revealed that SOFI analysis was comparable in terms of resolution to the SMLM approach in low SNR conditions. Furthermore, analysis showed artefacts in high-density regions, non-optimal for SMLM analysis. The resolution, estimated with an image decorrelation analysis algorithm, was found to be 56 nm for tubulin and 98 nm for actin (Figure 2.15). The excellent optical sectioning and contrast provided by SOFI allowed to routinely resolve individual actin filaments (Figures 2.2, 2.17). Subsequently, the corresponding cells were imaged in a custom SICM using an adaptive hopping mode. This yielded the topographical map of the cell membrane (Figure 2.2c) resolving individual microvilli and filopodia membrane structures. Fluorescence and

SICM images were registered based on the features from the topography map and the SOFI actin channel (Figure 2.2d). Filamentous actin (f-actin) is known to be located in the lower part of the cell volume and correlates well with the topography of the cell boundary(122) in COS-7 cells, that allowed us to simplify the registration process (Figure 2.23c).

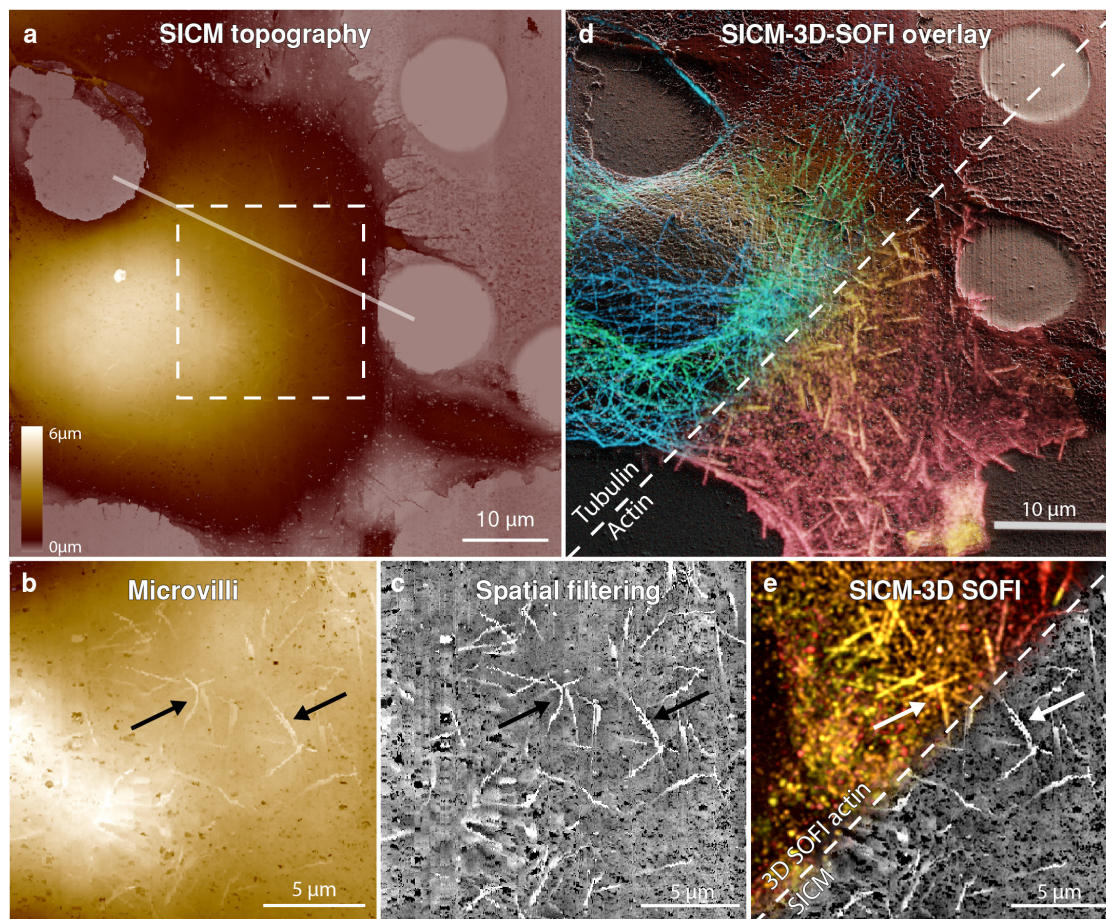


Figure 2.4 – Correlative SICM and 3D SOFI imaging of cytoskeletal components in a fixed COS-7 cell. (a) Topographical SICM map of a fixed COS-7 cell imaged on a dedicated SICM setup after two-color 3D-SOFI acquisition. Corresponding fluorescence images are shown in Figure 2.3. The scan resolution is 1024 x 1024 pixels over an 80 μm x 80 μm area with a corresponding pixel size of 78 nm. The pixel acquisition rate was 200 Hz with a hopping height of 6 μm . Semi-transparent line shows the cross-section area displayed in Figure 2.5. (b) Leveled zoom-in of the upper part of the cell by mean plane subtraction, showing the topography of microvilli (marked with black arrows) on the surface of the cell. (c) Spatial band-passed filtered SICM image to highlight multiple microvilli structures. (d) 3D rendered correlative SICM and two-color 3D-SOFI overlay. The tubulin and actin channels are rendered as volumes consisting of 22 planes, while topographical SICM information is used for a height representation in the Blender 3D software (Supplementary movie 1). (e) Correlative SOFI and SICM overlay (white arrows correspond to the black arrows in (b-c)). This figure is representative of more than 10 correlative SICM and 2-color 3D-SOFI single-cell images obtained from at least two independent experiments.

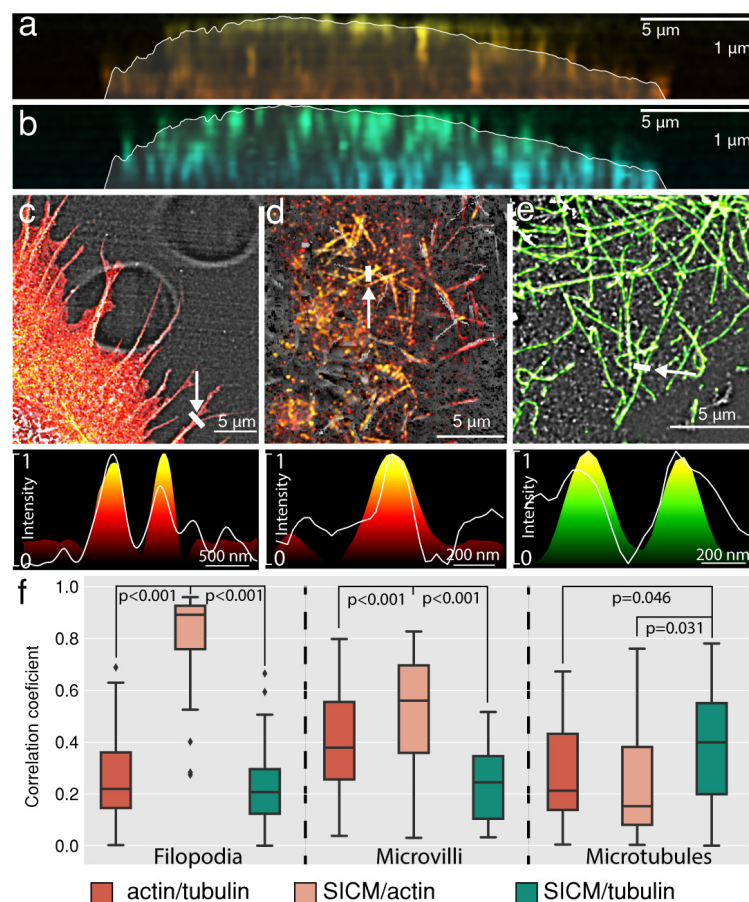


Figure 2.5 – Volumetric distribution of cytoskeletal components from correlative SICM-3D-SOFI images. Vertical cross-sections of actin (a) and tubulin (b) in a fixed COS-7 cell marked in Figure 2.3 and Figure 2.4 overlaid with the SICM topography displayed as a semi-transparent contour. (c-e) Correlative imaging of different cellular components resolved by SICM: filopodia overlaid with fluorescently labeled f-actin from 3D-SOFI (c), microvilli overlaid with fluorescently labeled f-actin from 3D-SOFI (d) and microtubules of chemically unroofed COS-7 cells overlaid with fluorescently labeled tubulin from 3D-SOFI (e). Normalized intensity profiles are displayed below each image. The arrows in (c,d,e) are guides for the eye to indicate the locations of cross sections. For overlays only, the intensity values of SOFI images were projected on spatially filtered SICM images for a better structural representation. (f) Normalized Pearson cross-correlation coefficients of normalized height and intensity cross-sections for both SICM topography and fluorescence channels. Cross-sections ($N=30$) were manually selected (Figure 2.22) from the SICM image for each of the features. Correlation coefficients were measured on filopodia structures, microvilli structures and microtubules. Significantly higher ($p < 0.05$, two-sided t-test) correlation values were identified for filopodia (SICM)/actin, microvilli (SICM)/actin (3D-SOFI) and microtubules (SICM)/tubulin (3D-SOFI). For all comparisons p values are shown in upper part of (f) panel. This figure is representative of more than 10 correlative SICM and 2-color 2D/3D SOFI single-cell images obtained from at least two independent experiments.

SOFI is not limited in providing the resolution improvement laterally, but it can also be used to improve axial resolution and sectioning by using information from multiple image planes acquired simultaneously. To demonstrate 3D SOFI's capability of volumetric single cell imaging, we performed two-color 3D SOFI imaging on a dedicated setup for the same cytoskeleton components with a multiplane SOFI approach based on an image splitting prism(118) (Figure 2.3a-b), allowing us to calculate cumulants in 3D. However, the trade-off for 3D imaging capability is a reduced signal-to-noise ratio, which makes it difficult to perform high-order SOFI analysis, therefore we only show up to 3rd order 3D SOFI images of microtubules labelled with the Abberior FLIP-565 dye and actin labelled with Alexa-647 (Figure 2.18). The acquired 8 physical planes resulted in 22 total planes spaced 116 nm apart after 3rd order SOFI computation, giving a 3D volume of $50\text{ }\mu\text{m} \times 60\text{ }\mu\text{m} \times 2.45\text{ }\mu\text{m}$ with a lateral resolution comparable to the 3rd order 2D SOFI results (Figure 2.14). A single color 3D SOFI image required as little as 3 min to acquire. This facilitates the screening of a large number of 3D cell volumes (Figure 2.19).

We then correlated the 3D SOFI information with the 3D SICM images, which have an order of magnitude higher axial resolution. The samples were moved to the dedicated SICM setup (Figure 2.4) to resolve microvilli at the surface of the cell (Figure 2.4b-c. Finally, we correlated SICM and 3D SOFI information (Figure 2.4d), which resulted in a detailed picture of the cell volume showing actin colocalized with microvilli protrusions over the whole cell surface (Figure 2.4e).

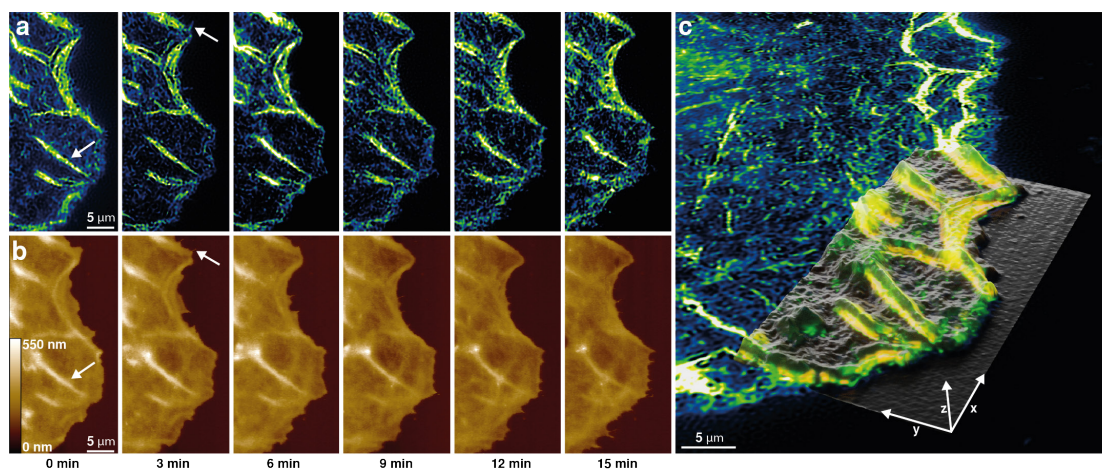


Figure 2.6 – Live-cell SICM/SOFI imaging of cytoskeletal actinin dynamics of COS-7 cell. (a) 2nd order SOFI images of actinin-mEOS-2 in transfected COS-7 cells reconstructed from 250 frames each, thus allowing to achieve 12.5 s temporal resolution per SOFI frame. (b) Corresponding SICM height maps (200 x 100 pixels image, with 200 nm pixel size) were acquired at a pixel acquisition rate of 200 Hz with a hopping height of 1 μm. Correlative SICM/SOFI data was recorded at 180s per frame. The white arrows indicate the corresponding features in SICM and SOFI images. (c) 3D render of SICM height map aligned to the full SOFI image at the start of the recording (0 min) revealing the correlative dynamics of actinin in a live-cell. This time-lapse sequence is representative of more than 5 independent correlative SICM/SOFI time-lapse experiments.

We have further interpreted the correlative information and compared the topographical maps of multiple cellular structures with two fluorescent channels which we acquired. Taking advantage of a multiplane SOFI approach, we compared the SICM topography with volumetric localization of actin (Figure 2.5a) and tubulin (Figure 2.5b) in a vertical section, which is marked in Figure 2.3c and Figure 2.4a. Patches of actin are distributed in the top and bottom parts of the cell, while tubulin is distributed homogeneously within the cell volume. We also measured the correlation values for different cellular structures such as filopodia (Figure 2.5c), microvilli (Figure 2.5d) and microtubules (Figure 2.5e) and calculated Pearson correlation coefficients between the pairs of actin, tubulin and SICM topography channels. The physical access to microtubules by SICM was obtained by partially removing the top membrane using Triton X-100 detergent during the permeabilization step(123) (Figure 2.20). We found high correlations between the SICM/actin channels for filopodia and microvilli structures and for SICM/tubulin channels (Figure 2.5f) for the chemically unroofed cell.

The establishment of a correlative SOFI/SICM pipeline on different instruments paved the way for a combined instrument. For correlative live-cell imaging, we combined the prototype SICM instrument with a 2D SOFI capable widefield microscope. We performed a correlative measurement of cytoskeletal proteins and cell morphology revealing the correlated dynamics of actin and membrane topography at the subcellular level. We transfected COS-7 cells for

cytoskeletal proteins of actin filaments (actinin or actin) fused with mEOS-2 photo-switching fluorescent proteins in order to achieve stochastic fluctuations in the fluorescence signal. Cells were then scanned in a consecutive manner with SICM and imaged with SOFI in a custom-design chamber with an environmental control. Recordings of 300 frame-long stacks of the fluorescence signal were performed after each SICM frame, resulting in a combined SICM/SOFI acquisition time of 3 min/frame for images of parts of the cell, and 10 min for whole cell imaging (Figure 2.24, Figure 2.25). The 2nd order SOFI images in Figure 3.10a show the actin filaments with a 173 ± 20 nm (mean \pm s.d, N=6 images for live-cell SOFI 2D resolution measurements) lateral resolution. After recording, SICM and SOFI images were aligned, revealing correlated dynamics of cytoskeletal proteins and membrane topography (Figure 3.10b-c). During the SICM imaging, there was no laser applied, resulting in two-minute dark intervals between SOFI frames. This significantly reduced the photodamage enabling us to record time-lapse sequences of 10-15 SOFI frames for up to 42 min without observable cell negative phototoxic effects (Figure 2.24).

2.4 Discussion

We have established correlative membrane topography and cytoskeleton imaging provided by combined SICM and SOFI modalities for fixed COS-7 cells both in 2D and 3D on separate imaging setups preserving the state-of-the-art capabilities of both imaging modalities. For imaging densely-labelled samples we used novel self-blinking dyes suitable for high-order SOFI imaging. Additionally, the 3D SOFI approach allowed us to retrieve information about the cytoskeletal protein distribution within the cell volume. Subsequently acquired SICM high-resolution axial topography provided detailed volumetric cell-mapping. Finally, we have performed simultaneous SICM/SOFI live-cell imaging in a combined setup for routinely obtaining correlative measurements *in vitro*.

Previous studies have demonstrated that a combination of topographical and biochemical sample information is a powerful tool which can provide a comprehensive picture of cellular activity. Correlative SPM and super-resolution microscopy studies, involving techniques such as SMLM(116), stimulated emission depletion (STED)(87; 63), structured light illumination (SIM)(82) have been demonstrated. SOFI, as a computational method, does not require a complex optical setup design compared to SIM or STED approaches. We show that it can be easily implemented on existing SPM/SICM setups with only few optical components required. Simultaneous SICM measurements can be used to directly detect the cell topography changes related to apoptosis(124) thus acting as a detector for phototoxicity. Furthermore SICM has been shown to outperform AFM in live-cell imaging(80) due to its non-contact nature, which is crucial in imaging sensitive samples. SICM and confocal microscopy combination was demonstrated to be a versatile tool to study virus-like particle and cell interactions (125; 126). Small imaging volume, located in the vicinity of the pipette, allows to have superior optical sectioning and colocalized measurement, which is ideal for studying cellular activity near the membrane. On the other hand, AFM has demonstrated its superiority over SICM in terms of

imaging resolution(77). AFM is also more versatile in terms of retrieving information about the nanomechanical sample properties(127) and can even be used for molecular-specific imaging(128). Due to the fragile nature of the glass nanocapillary, SICM is less forgiving of imaging mistakes that can lead to fracture of the capillary. This is exacerbated by the fact that no pre-fabricated SICM capillaries are commercially available.

We demonstrated the ability of the combined method for biological studies of the dynamic cell morphology and cytoskeletal architecture inside the cells. This could be used to investigate open questions in membrane trafficking(100), cell migration(129) or infection (130). Due to the electrical nature of SICM measurements, it can also retrieve surface charge information(79), thus adding a whole new dimension for the measurement. The ability to additionally map the charge of a cell membrane is particularly relevant for problems such as clustering of membrane proteins(131), membrane curvature influence on density of membrane proteins and lipids(132), lipid-rafts(133), behaviour of voltage-gated ion channels(134), etc. While there are some remaining technological challenges in terms of usability, the combination of the multimodal SICM and flexible SOFI has the potential to become a routine live-cell imaging modality capable of tackling challenging biological problems.

2.5 Methods and Supporting Information

2.5.1 2D widefield fluorescence imaging setup

A home-built widefield microscopy setup described previously(30) was used (Figure 2.7). The setup has four laser lines for illumination: a 200 mW 405 nm laser (MLL-III-405-200mW, Roithner Lasertechnik), a 1 W 632 nm laser (SD-635-HS-1W, Roithner Lasertechnik), a 350 mW 561 nm laser (Gem561, Laser Quantum) and a 200 mW 488 nm laser (iBEAM-SMART-488-S-HP, Toptica Photonics). The beam of the 635 nm laser is flat fielded by coupling it into the multimode fiber and passed through a speckle reducer (Optotune, LSR-3005-17S-VIS) similarly to that described previously(135). All laser lines are collimated, expanded and focused in the back focal plane of the water immersion 60x objective (Nikon SR Plan Apo IR 60 \times 1.27 NA WI) resulting in the effective FOV of 100 \times 100 μ m with a pixel size of 107 nm. Fluorescence signal is then filtered using a quad-line dichroic mirror (ZET405/488/561/640, AHF Analysetechnik) and emission filter (R405/488/561/635 flat, AHF Analysetechnik). Additional band-pass emission filters (596/83 or 685/70, Chroma) were used for sequential two-color imaging. Finally, the light is focused on a sCMOS camera (ORCA Flash 4.0, Hamamatsu; back projected pixel size of 108 nm). Z stabilization is achieved with a PID controller using a total internal reflection from a coverslip using 980 nm laser diode (CPS980, Thorlabs) reflecting from a sample at the critical angle. Axial positioning is achieved with a nano-positioning stage (Nano-Drive, MadCityLabs) using a custom-written software in LabVIEW environment. Lateral sample position is controlled by a Scan-plus IM 120 \times 80 (Marzheuser) stage. Image sequence acquisition is done in Micromanager software.

Chapter 2. Correlative 3D microscopy of single cells using super-resolution and scanning ion-conductance microscopy

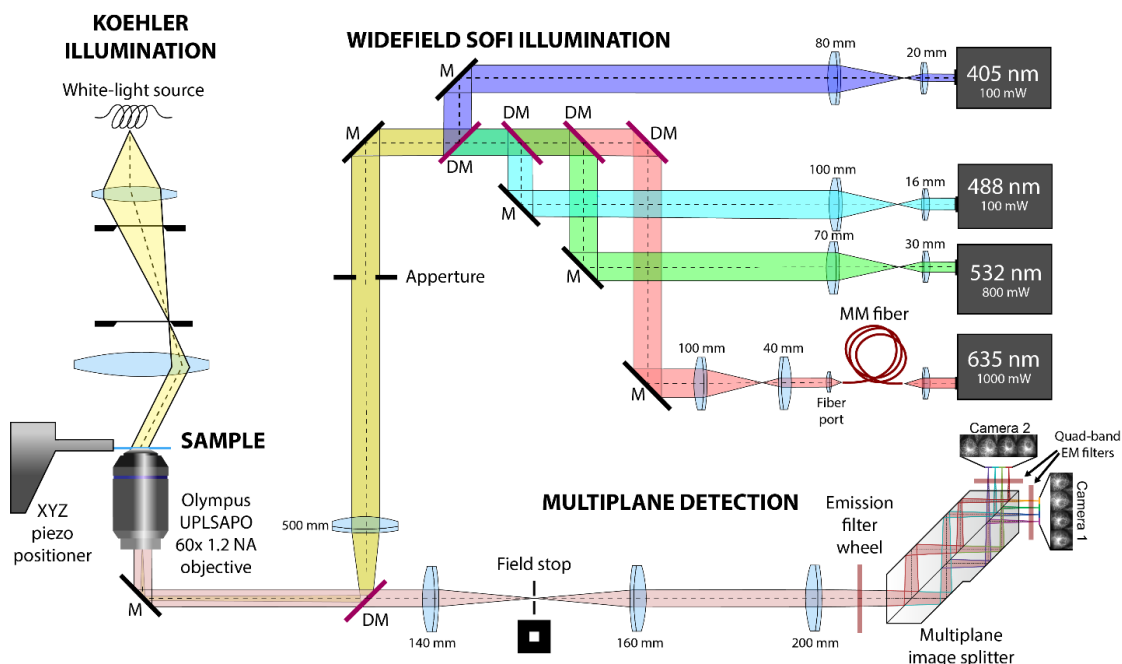


Figure 2.8 – Detailed schematics of 3D SOFI setup. Schematics of the setup used for 3D SOFI imaging as described in the Methods section.

TOR102SG). The nanocapillary was moved in Z by a home-built actuator, operated in hopping mode. Borosilicate and quartz nanopipettes were fabricated with a CO-2 laser puller (Model P-2000, Sutter Instruments) with a radius below 60 nm (Figure 2.26) fabricated as described previously(136).

2.5.4 Combined 2D widefield fluorescence /SICM setup

A home-built widefield setup is assembled in combination with a SICM scanner (For more detail see SICM setup) mounted atop an inverted Olympus IX-071 microscope body (Figure 2.9). For sample excitation, a four-color (405 nm, 488 nm 561 nm, 647 nm) pigtailed Monolithic Laser Combiner (400B, Agilent Technologies) is used. Light is collimated and focused to the back focal plane of the oil-immersion high-NA objective (Olympus TIRFM 100x, 1.45 NA) by using a custom built TIRF illuminator. The fluorescence signal is then filtered using a dichroic mirror (493/574 nm BrightLine, Semrock) and a band emission filter (405/488/568 nm stop line, Semrock). Finally, the light is focused on an sCMOS camera (Photometrics, Prime 95B; back projected pixel size of 111 nm). Coarse lateral sample positioning is done with a mechanical stage, while fine positioning is achieved with a SICM XY piezo scanner (Piezosystem Jena TRITOR102SG). Image stacks for SOFI are recorded with a Micromanager software, while laser control and sample positioning are achieved in custom-written LabVIEW software.

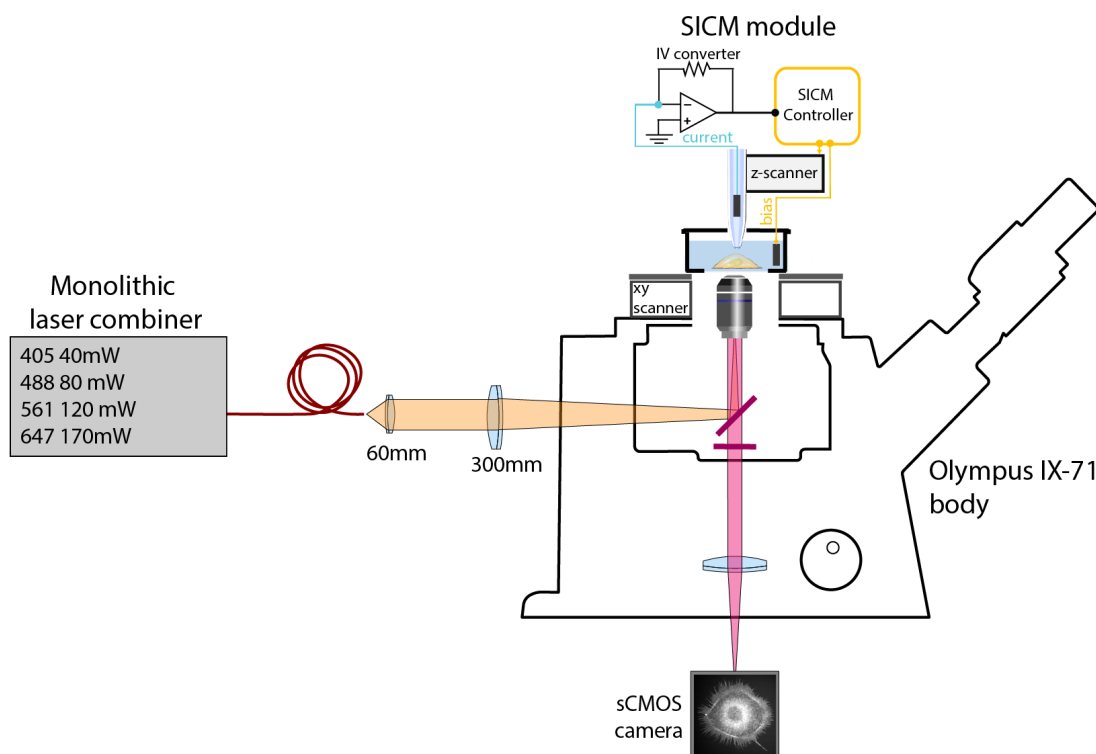


Figure 2.9 – Detailed schematics of a combined SICM-SOFI setup.

2.5.5 Coverslip fabrication

High precision No. 1.5 borosilicate 25 mm coverslips (Marienfeld) were patterned with a custom layout (Figure 2.10) by using a commercial UV excimer laser patterning setup (PTEC LSV3). It allowed to create a user-friendly sample map, which was crucial for further SOFI-SICM correlation experiments while transferring the sample between different setups. After patterning, coverslips were cleaned with piranha solution, washed in MiliQ water, dried with N_2 flow and kept dry for further use. Before use, coverslips were cleaned with oxygen plasma cleaner (Femto A, Diener electronic GmbH) for 660 s at maximum power setting, washed with PBS (pH = 7.4) once and coated with 50 μ M fibronectin solution in PBS (pH = 7.4) for 30 min at 37° C before seeding the cells.

2.5.6 Cell culture

Cells were cultured at 37 °C and 5 % CO₂. DMEM high glucose without phenol red medium (Gibco, Thermo Fisher Scientific) was used, containing 10 % fetal bovine serum (Gibco, Thermo Fisher Scientific), 1% penicillin-streptomycin (Gibco, Thermo Fisher Scientific) and 4 mM L-glutamine (Gibco, Thermo Fisher Scientific). Before seeding on coverslips, cells were detached from a flask with TrypLE (Gibco, Thermo Fisher Scientific) and 30 000 cells were seeded on 25 mm coverslips coated with fibronectin. Coverslips were washed twice with PBS before seeding

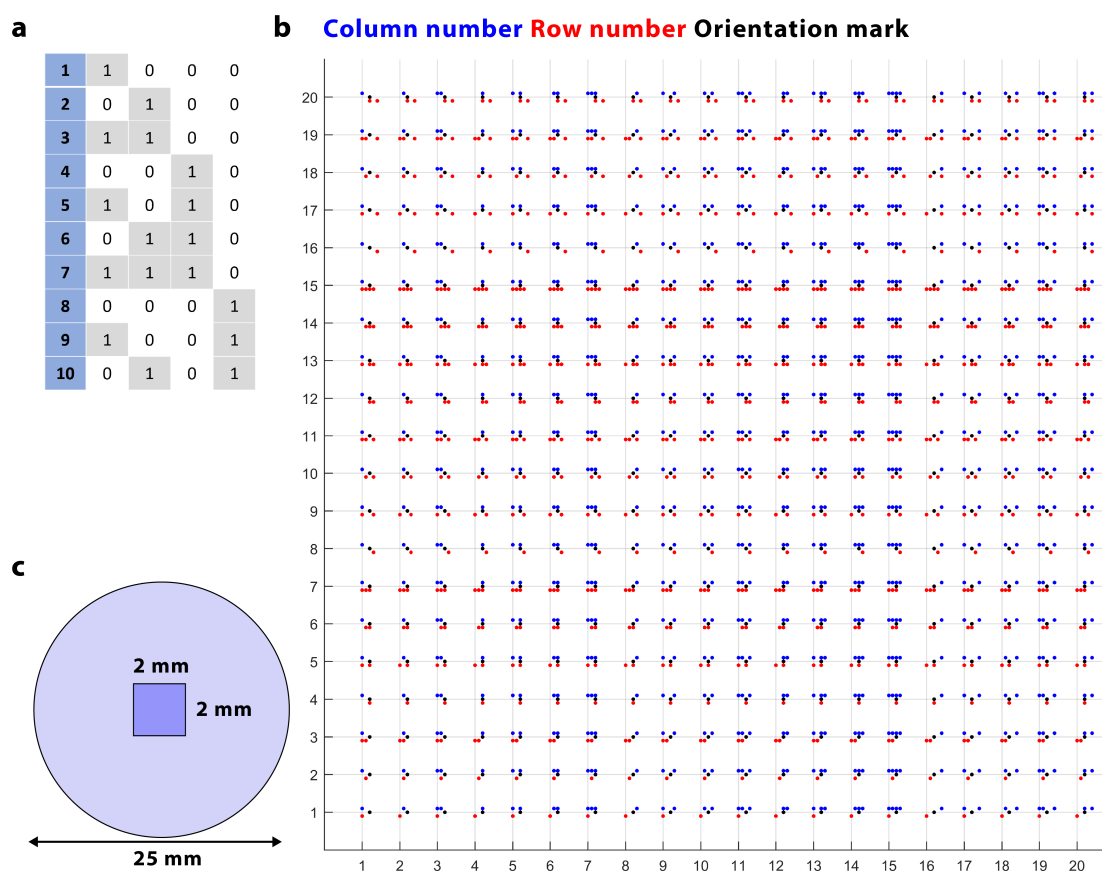


Figure 2.10 – Coverslip fabrication and binary mark map generation. (a) The principle of number representation in binary values. 4 binary digits were used to represent numbers from 1 to 20. (b) The final layout of the sample map. Layout was generated with a Matlab code, by using the `dec2bin` function. Binary numbers were used for x and y axis. The static dot in the middle was incorporated for a better determination of the sample orientation. (c) Schematics of the dimensions of the binary digit pattern.

the cells and 2 ml of DMEM medium was used. Cells were grown overnight (12-16 h) before fixation in 6-well plates.

2.5.7 Sample fixation and staining

Cells were washed once with DMEM described previously and incubated for 90 s in a pre-warmed microtubule extraction buffer, consisting of 80 mM PIPES, 7 mM $MgCl_2$, 1 mM EDTA, 150 mM NaCl and 5 mM D-glucose with a pH adjusted to 6.8 using KOH with 0.3 % (v/v) Triton X-100 (AppliChem) and 0.25 % (v/v) EM-grade glutaraldehyde (Electron Microscopy Sciences). After 90 s the solution was exchanged to pre-warmed 4 % paraformaldehyde dissolved in PBS (pH=7.4) and samples were incubated for 10 min at room temperature. Afterwards, samples were washed thrice for 5 min with PBS on orbital shaker. Cells were kept for 5 min with a freshly

prepared 10 mM NaBH₄ solution in PBS on an orbital shaker in order to reduce background fluorescence. Step was followed by one quick wash in PBS, and two washes of 10 min in PBS on an orbital shaker. Samples were then additionally permeabilized to ensure antibody penetration with 0.1 % (v/v) Triton X-100 in PBS (pH=7.4) on an orbital shaker followed by additional wash with PBS. Finally, samples were blocked with freshly prepared blocking buffer consisting of 2 % (w/v) BSA, 10 mM glycine, 50 mM ammonium chloride NH₄Cl in PBS (pH=7.4) for 60 min at room temperature or stored overnight at 4 °C for further staining. All chemicals were bought from Sigma Aldrich unless stated differently.

2.5.8 Two-color sample staining

For incubation with antibodies and/or phalloidin, coverslips were placed on parafilm in a closed box in the dark, at high humidity to prevent coverslips from drying. 100 µL of staining solution was typically used for each coverslip. After blocking, samples were incubated with 2% (v/v) primary anti-tubulin antibody (clone B-5-1-2, Sigma-Aldrich) in blocking buffer for 60 min at room temperature. Samples were washed with blocking buffer thrice for 5 min on orbital shaker. Coverslips were incubated with 2 % (v/v) secondary donkey anti-mouse-Abberior FLIP-565 antibody, which was labelled as described previously(30). Samples then were kept in blocking buffer for 60 min and washed thrice for 5 min on orbital shaker. Samples were incubated for 10 min in 2 % (w/v) PFA in PBS (pH=7.4) as a post-fixation step followed by three 5 min washes with PBS on orbital shaker. After tubulin staining, actin was stained with 500 nM custom synthesized phalloidin-f-HM-SiR (Figure 2.11) or phalloidin-Alexa-647 (Sigma Aldrich) solutions in PBS by incubating for 60 min at room temperature. Samples were washed thrice for 5 min with PBS on orbital shaker and imaged immediately in imaging buffer.

2.5.9 Phalloidin-f-HM-SiR chemical synthesis

Phalloidin f HM SiR was synthesized from f-HM-SiR(33) and Phalloidin BCN, which were prepared according to literature procedures. In short: Phalloidin BCN (46 µg) was dissolved in anhydrous MeCN (90 µL) and f-HM-SiR (24.8 µg, 4 µL from 10 mM stock solution) was added at room temperature. The reaction mixture was incubated for 4 h in a thermo-shaker at 700 rpm and subsequently purified by HPLC (gradient 20-90% solvent B / solvent A ; in 40 min). Phalloidin f HM SiR was afforded as blue solid and after photometric determination of the amount of substance, a 1 mM stock solution in anhydrous DMSO was prepared. HRMS (ESI+) m/z 1867.9047 calculated for [C₉₄H₁₃₁N₁₄O₂₂SSi]⁺ (M⁺), 1867.91 found; m/z 945.4470 calculated for [C₉₄H₁₃₁N₁₄NaO₂₂SSi]²⁺ (M⁺⁺Na⁺), 945.4482 found. HPLC analytics and semi-preparative purifications were conducted on an Agilent 1100 series HPLC system. Phenomenex Luna 3 µ and 5 µ C18 reversed-phase columns were used for these purposes (Solvent A: H₂O containing 0.1% TFA; Solvent B: MeCN containing 0.1% TFA). Collected HPLC fractions were dried by lyophilization. Mass spectrometry was performed on a Bruker microTOF-QII (for ESI-MS) mass spectrometer. Synthesis was performed by Philipp Werther.

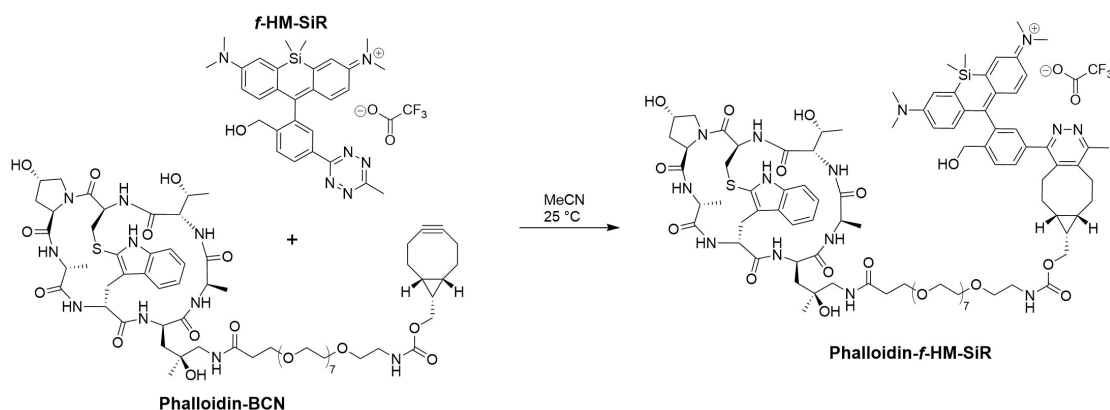


Figure 2.11 – Reaction scheme of Phalloidin-f-HM-SiR conjugate.

2.5.10 Imaging buffers

2D imaging with self-blinking dyes was performed in 50 % glycerol PBS solution at pH=8. The buffer was degassed with N₂ flow for 30 min before use. 3D phalloidin-actin imaging was performed in an imaging buffer described previously(37) containing 10 % (w/v) D-glucose, 20 % (v/v) glycerol, 50 mM TRIS, 10 mM NaCl, 2 mM COT, 10 mM MEA, 2.5 mM PCA and 50 nM PCD with a pH adjusted with HCl to 7.5. 3D imaging of tubulin labelled with an Abberior FLIP-565 was performed in 50 % (v/v) glycerol solution in PBS (pH=7.4). All imaging experiments were done in a sealed imaging chamber.

2.5.11 Two-color SOFI imaging

2D SOFI imaging was performed with self-blinking dyes sequentially. Phalloidin-f-HM-SiR labelled actin was imaged first at 275 W/cm^2 635 nm excitation, then 680 W/cm^2 of 561 nm was used to image Abberior FLIP-565 labeled tubulin. The sample was kept on the setup for at least 30 min before imaging, to reduce thermomechanical drift during imaging. 16 000 – 30 000 frames were acquired for each channel for high-order SOFI analysis with a minimal photobleaching effects (Figure 2.15, Figure 2.12). Sample drift between two-color acquisitions was neglected for further analysis. 3D SOFI imaging was first performed with phalloidin-Alexa-647 labelled actin excited with a 632 nm laser at 3.4 kW/cm^2 with a low power (5 W/cm^2) 405 nm activation laser to increase the population of fluorophores in a bright state. After imaging multiple cells, the oxygen-scavenging imaging buffer was changed to 50 % (v/v) glycerol in PBS for Abberior FLIP-565 labelled tubulin imaging. The sample was then imaged with the 532 nm laser at 3.5 kW/cm^2 . 4 000 frames for each image plane were recorded for high-order 3D-SOFI analysis. After recording each image stack, a subsequent brightfield-image was taken for a further alignment of 2-channel data. 50 ms exposure time was used for all imaging experiments. The data presented in the paper are from two distinct samples.

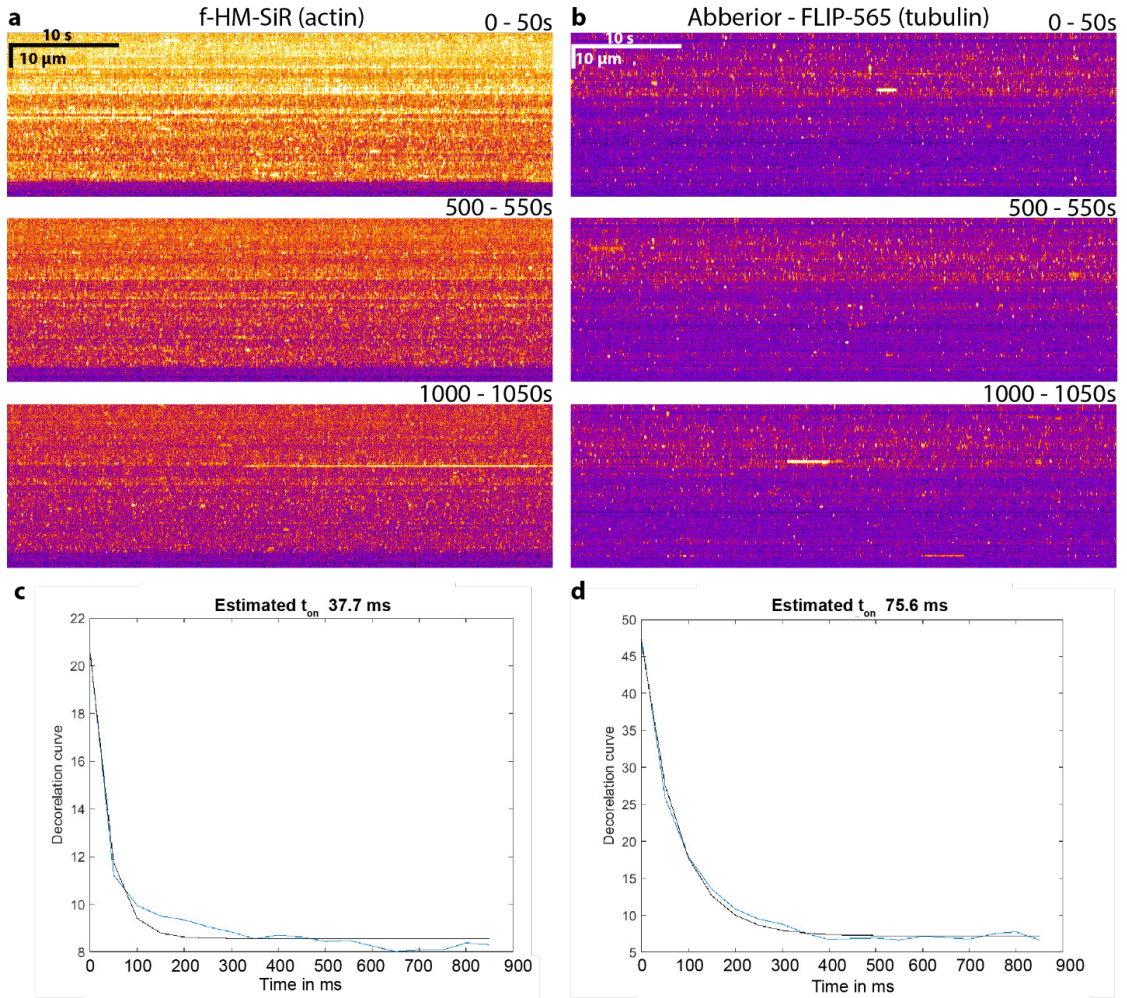


Figure 2.12 – Kinetics of self-blinking dyes for high-order SOFI imaging and ON time estimation. Kymographs of signal intensity over time for f-HM-SiR (a) and Abberior-FLIP 565 (b) dyes showing the signal fluctuation over a long-term imaging. Average ON-times were also estimated by computing 2nd order cumulant as a function of time lag and averaging it for subsequences of 500 frames¹. Corresponding lag functions for stacks showed in (a-b) are showed below (c-d). Mean on time for f-HM-SiR dye was estimated to be 38.7 ms and for Abberior-FLIP 565 – 65.75 ms. However, the exposure time of 50 ms might be the limiting factor for the precision of ON-time estimation.

2.5.12 SICM imaging and processing

The SICM imaging was performed in PBS (pH = 7.4). On fixed cells, SICM images with 1024x1024 pixels were acquired at a pixel acquisition rate of 200 Hz with a hopping height of 5 μm and 6 μm . After performing fluorescence imaging corresponding cells were found using markers described in a coverslip fabrication section. On live cells, SICM images with 512x256 and 200x100 pixels were acquired at a pixel acquisition rate of 200 Hz with a hopping height of 1 μm and 3 μm . These experiments were performed in the combined SICM/SOFI system

Chapter 2. Correlative 3D microscopy of single cells using super-resolution and scanning ion-conductance microscopy

described previously. The current setpoint used in all the SICM measurements was 99% of the normalized current recorded. SICM images were further processed using Gwyddion(137) and Fiji(138).

2.5.13 SOFI Image analysis and image alignment

2D and 3D SOFI image analysis was performed as described previously(30; 118). Briefly, the image stack was drift-corrected using cross-correlation between SOFI sub-sequences before performing cumulant calculation. Different planes of the 3D image stack were registered based on acquired bead stack and images sequence was drift-corrected after the registration, assuming that the drift is homogenous within the volume. 4th order SOFI images were used in 2D SOFI case, while 3rd order SOFI images were taken for 3D SOFI. Images were further deconvolved with a Lucy-Richardson deconvolution algorithm using gaussian PSF model. Deconvolution settings were optimized using decorrelation analysis algorithm for resolution estimation 30. 2D and 3D SOFI analysis code was implemented in Matlab and is available upon request. After 2D and 3D SOFI processing, images were aligned with a topographical SICM map using custom-written Python code based on the hand-selected features in the actin channel and SICM image using an affine transformation (Figure 2.23). For two-color 3D SOFI, two-color SOFI stacks were co-registered based on brightfield images and then aligned with SICM image based on the actin channel.

2.5.14 Live-cell SOFI/SICM imaging

COS-7 cells were seeded according to the procedure described previously. After 12-16 h cells were transfected with actinin-mEOS2 or Lifeact-mEOS2 (Supplementary information: Plasmid sequences) with a Lipofectamine 3000 (Thermo Fisher) according to the protocol provided by manufacturer. Cells were used for combined SICM-SOFI experiment 24 h after the transfection. Imaging was performed at 37 °C and 5 % CO₂ in a custom-built imaging chamber in FluoroBrite DMEM media (Gibco, Thermo Fisher Scientific) in order to reduce autofluorescence. SICM and SOFI imaging was performed subsequently i.e. after each SICM image, a fluorescent stack of 300 frames with an exposure time of 50 ms was recorded. The first 50 frames were excluded from SOFI processing due to rapid intensity change upon 405 activation and only 250 frames were used for further SOFI analysis. Live-cell imaging was performed under the low-illumination intensity (500 W/cm^2 of 561 imaging laser and 0.3 W/cm^2 of 405 nm activation laser) in order to reduce phototoxicity.

2.5.15 Correlative 3D SICM/SOFI data rendering

In order to fully expose the correlative 3D data, we have used the advanced open-source 3D rendering tool Blender 3D for data visualization. Normalized topographical SICM data was imported as a height map and scaled in the axial direction. Then, 2D SOFI data was overlaid

by importing a co-registered fluorescence image and a custom-written shader was used for volumetric multiplane data rendering (Figure 2.27) to generate the final figures.

2.5.16 Acknowledgements

V.N. and A.R. acknowledges the support of the Max Planck-EPFL Center for Molecular Nanoscience and Technology and Swiss National Science Foundation through the National Centre of Competence in Research Bio-Inspired Materials. K.Y. and D.P.H. gratefully acknowledge funding by the Centre of Membrane Proteins and Receptors (COMPARE, Universities of Birmingham and Nottingham). GEF acknowledges the support by the European Research Council under grant number ERC-2017-CoG; InCell; Project number 773091. The authors thank Adrian Pascal Nievergelt and Charlene Brillard for their input on technical development of SICM controller. The authors also thank Prof. Jens Anders and his team from the University of Stuttgart for insightful discussions into high-speed transimpedance amplifiers.

2.6 Supporting figures

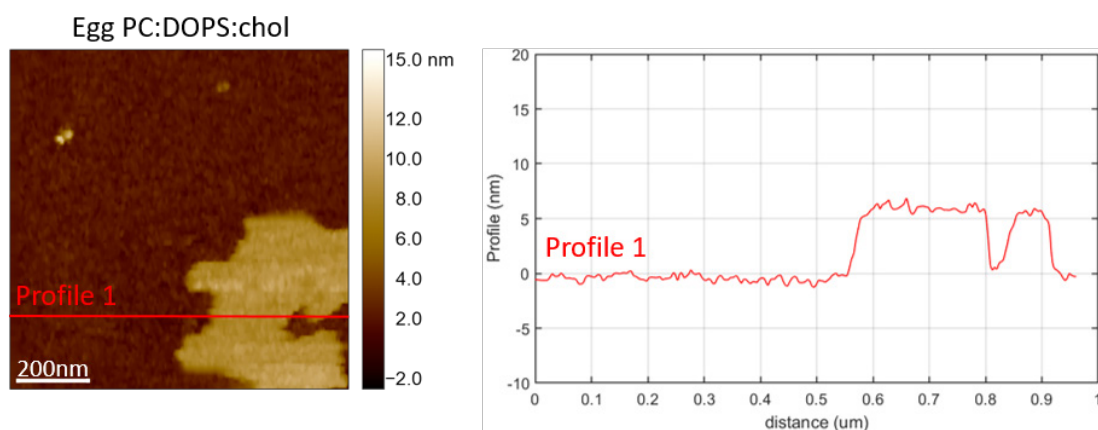


Figure 2.13 – SICM image of a supported lipid bilayer (SLB) for axial resolution estimation. (a) SICM image of a SLB, composed of Egg PC:DOPC:chol (3:1:2), deposited on mica acquired using 15 nm radius nanocapillary. 480 x 480 pixels image acquired at pixel acquisition rate of 300 Hz with a hopping height of 100 nm. (b) Height profile of the SLB indicating the axial resolution of SICM below 5 nm.

Chapter 2. Correlative 3D microscopy of single cells using super-resolution and scanning ion-conductance microscopy

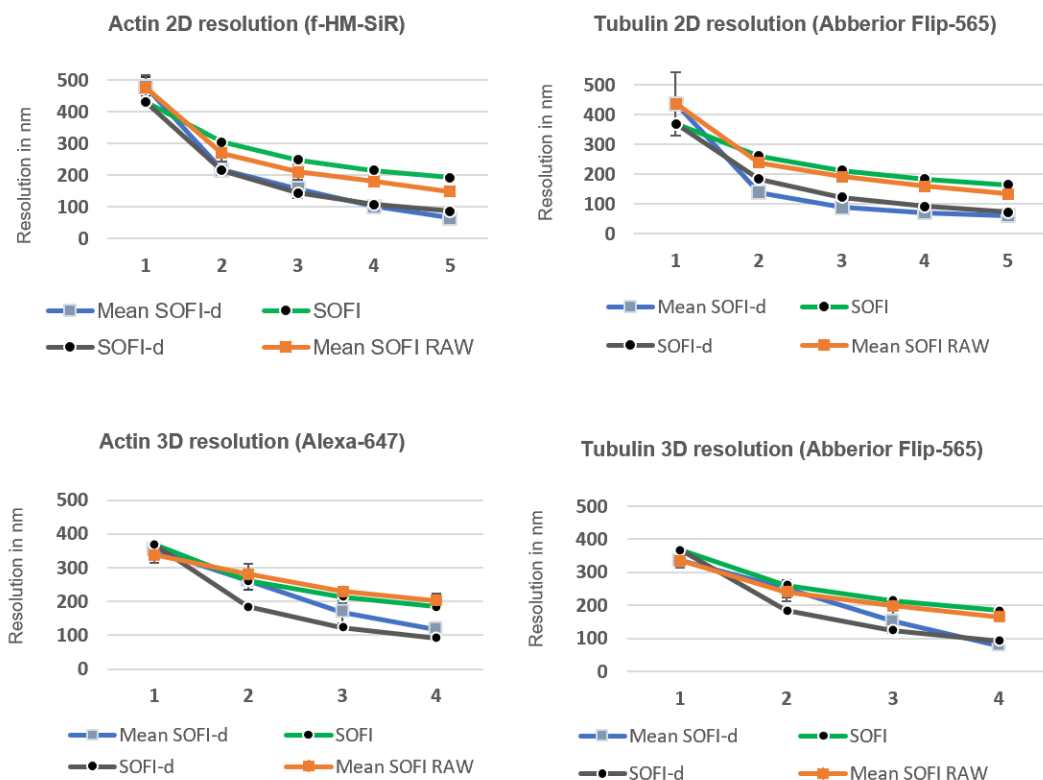


Figure 2.14 – SOFI resolution estimation for two-color 2D and 3D SOFI images. Resolution was estimated with a parameter-free image resolution estimation algorithm 3. For 2D images, each value is calculated from 8 images. For 3D SOFI stack resolution was estimated in all planes ($N=8$, $N=15$, $N=22$, $N=29$) for corresponding SOFI orders. Theoretical values for SOFI and SOFI-d (deconvolved) based on the diffraction limited PSF size are also plotted.

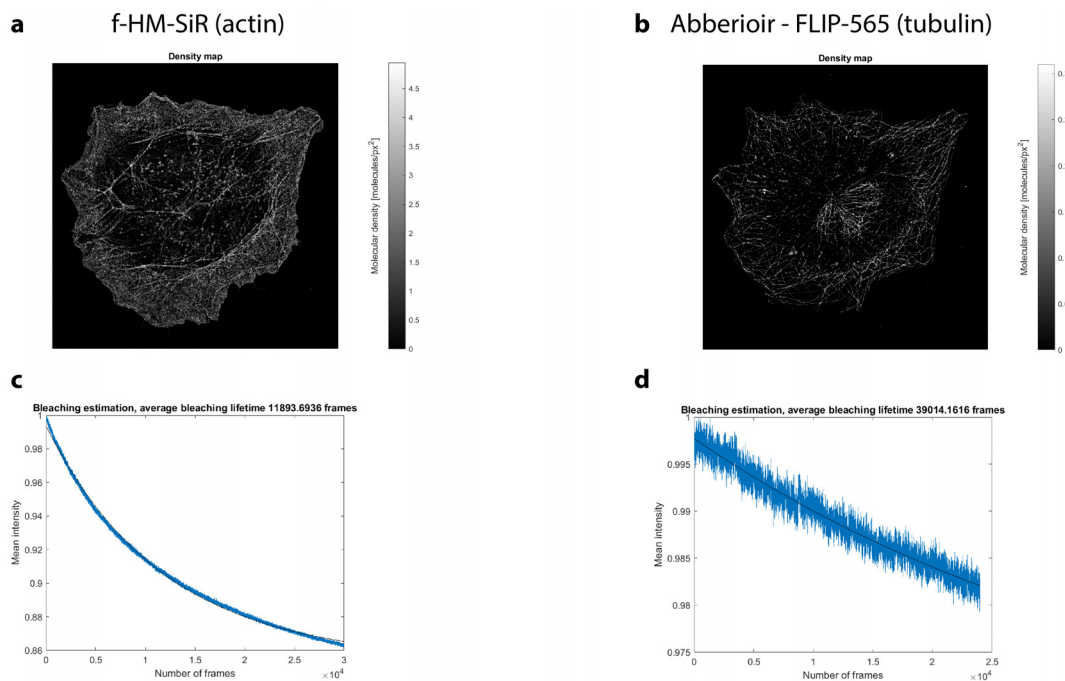


Figure 2.15 – Labelling density and bleaching kinetics of self-blinking dyes. Molecular densities of f-HM-SiR (a) and Abberior-FLIP 565 (b) dyes from a representative image, together with bleaching curves estimated from the corresponding image stacks. Calculated average bleaching lifetimes (8 stacks with 30 000 frames) for f-HM-SiR dye was 406 ± 168 s and 625 ± 130 s for Abberior FLIP-565 (mean \pm s.d, N=8 image stacks consisting of 30 000 frames).

Chapter 2. Correlative 3D microscopy of single cells using super-resolution and scanning ion-conductance microscopy

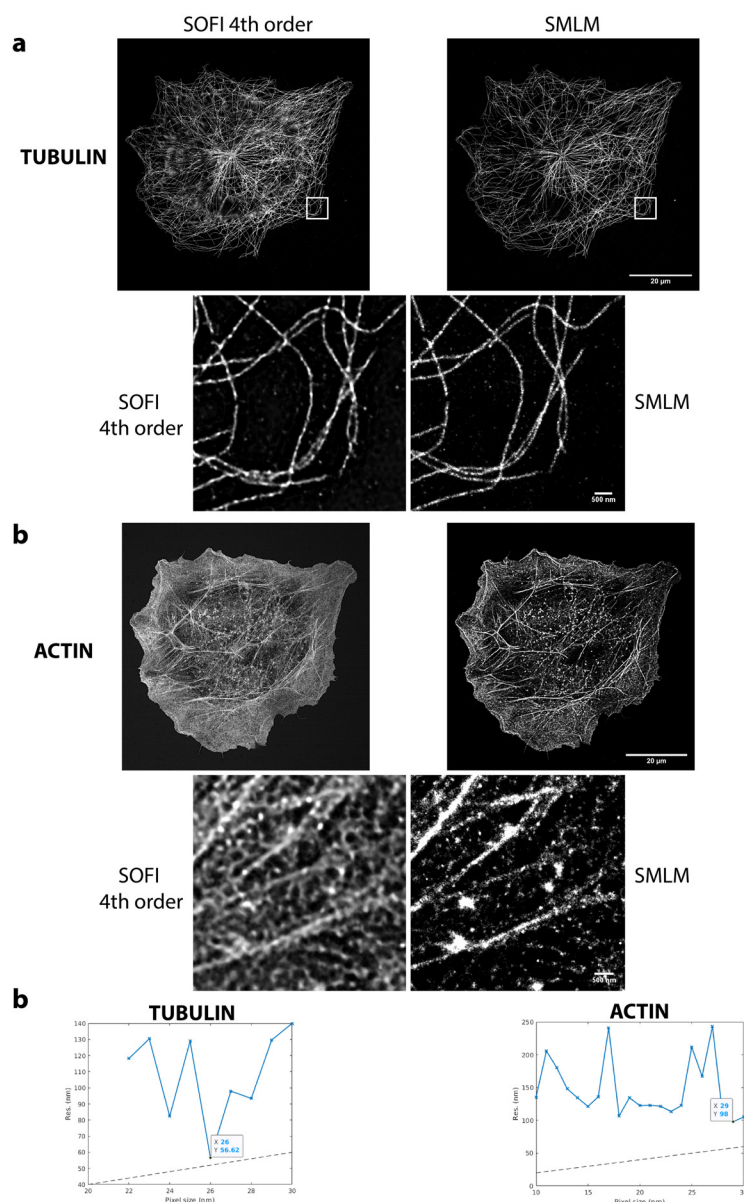


Figure 2.16 – High order SOFI comparison with SMLM. a) 4th order SOFI and SMLM (Thunderstorm) image quality comparison. Images stacks were processed with the latest version of Thunderstorm software2 by using single-emitter fitting function. It is visible that in sparse blinking conditions (Abberior FLIP-565 labelled microtubules) both approaches (SOFI and Thunderstorm) perform similarly, however for f-HM-SiR labelled f-actin SMLM seems to produce localization artifacts, that are expected for high-density data. Resolutions metric stated in the paper were computed with image decorrelation analysis algorithm3. The localization precision might be improved by using multi-emitter fitting or pre-processing tools such as HAWK4, however this is clearly outside of the scope for this study.

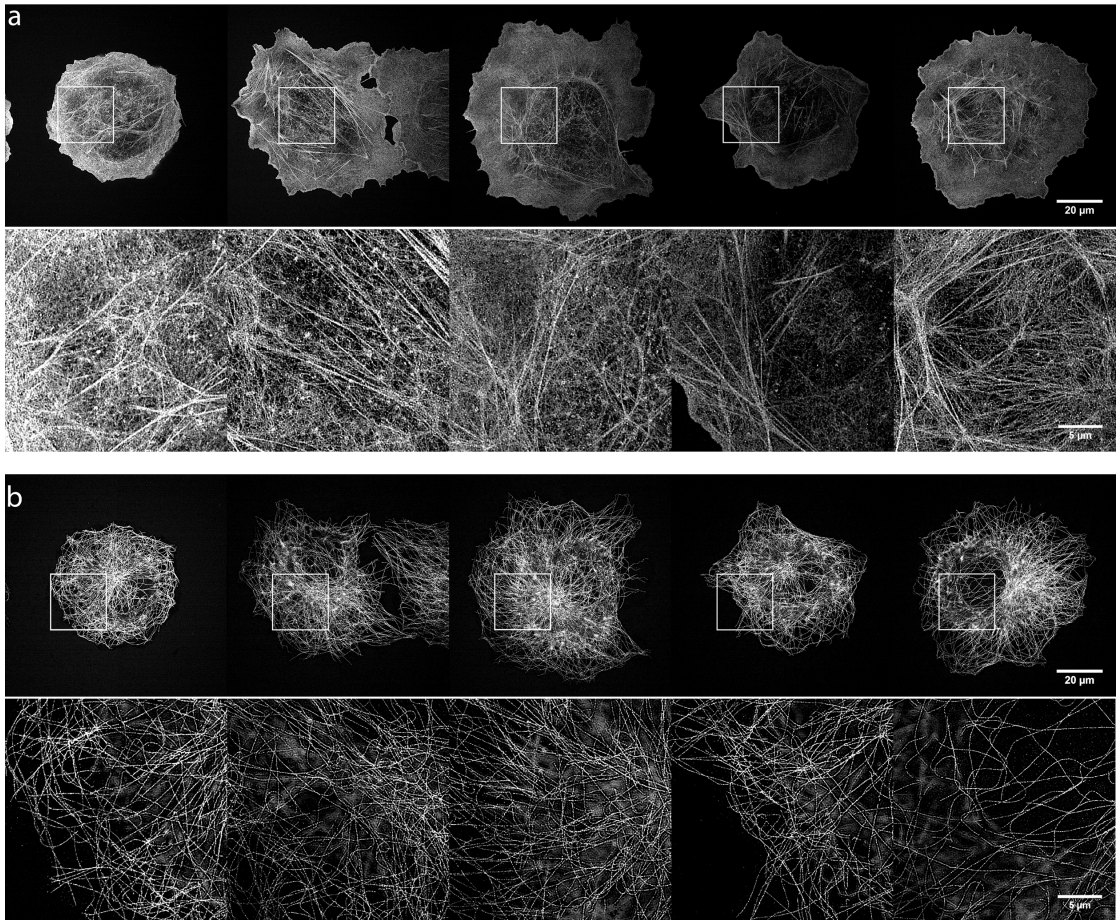


Figure 2.17 – Multiple two-color 4th order SOFI images. 4th order SOFI images of phalloidin-f-HM-SiR labeled actin (a) and Abberior FLIP-565 immunostained tubulin (b). Zoom-ins of 25 μm are shown together with the whole 90 μm x 90 μm field of view images.

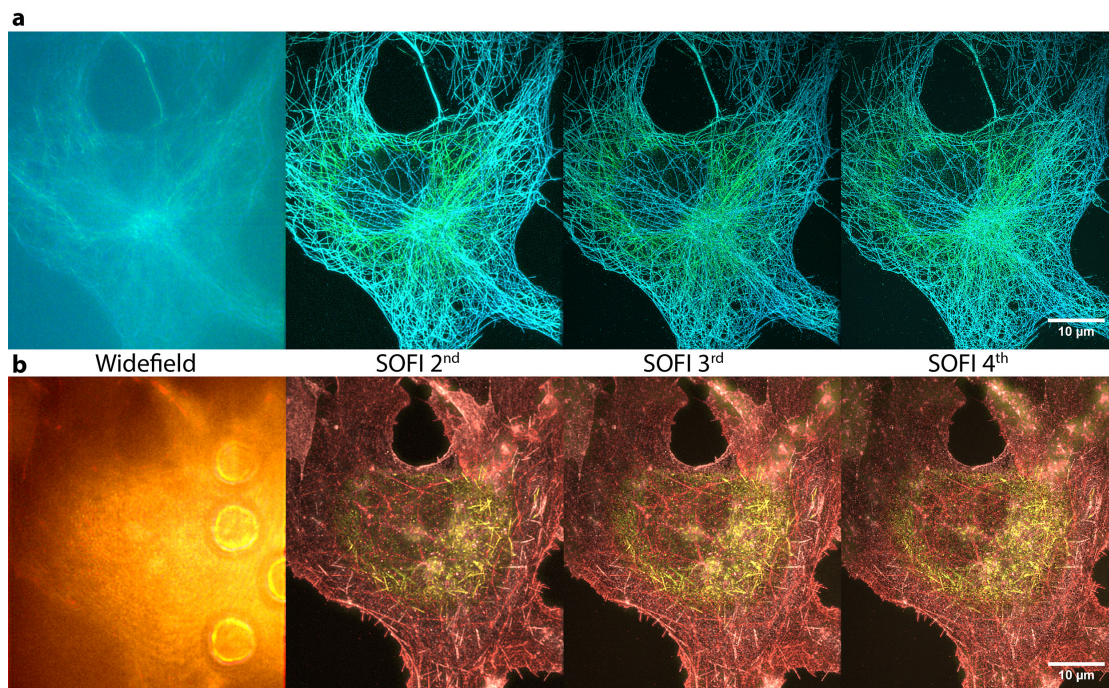


Figure 2.18 – Comparison of image quality of 3D SOFI orders. SOFI orders for the two-color 3D SOFI image used in the main text Figure 3.

2.6. Supporting figures

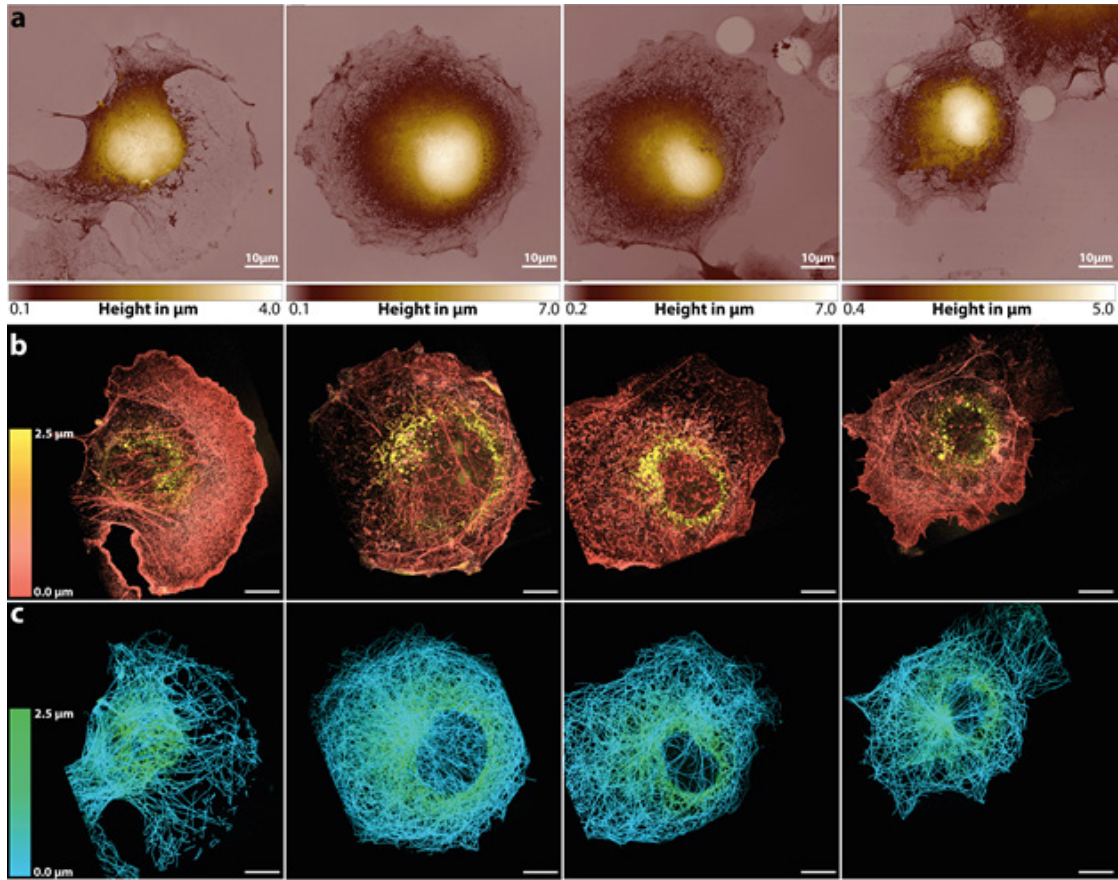


Figure 2.19 – Multiple correlative SICM and two-color 3rd order 3D SOFI images. (a) SICM images (1024 x 1024 pixels, 78nm pixel size), acquired at pixel acquisition rate of 200 Hz with a hopping height of 5 μm SICM images are shown at the top row; (a) together with a co-aligned 3rd order SOFI images of phalloidin-Alexa647 labeled actin (b) images labeled with letter A) and Abberior FLIP-565 labelled tubulin (images labeled with Tc). 2.45 μm axial range is represented with a color bar. Axial scales are represented as color bars. Scales bars are 10 μm in all images. All images were correlated according to a procedure described in Methods section.

Chapter 2. Correlative 3D microscopy of single cells using super-resolution and scanning ion-conductance microscopy

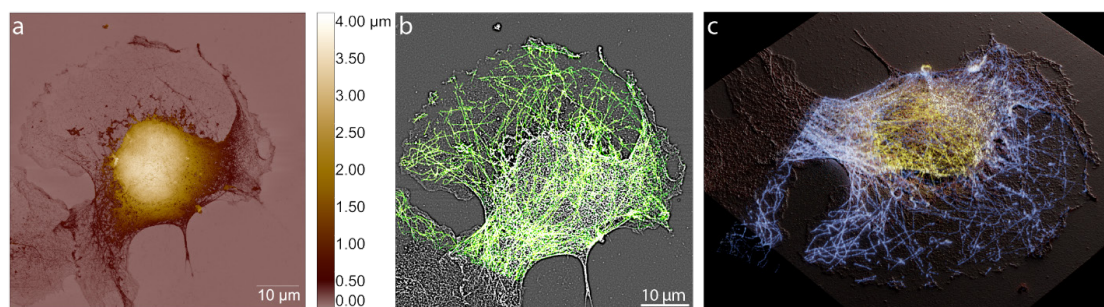


Figure 2.20 – SICM topographical map of microtubules. (a) SICM image of a single cell which has part of the membrane removed by permeabilization with Triton X-100. Interestingly, this allows to reveal a preserved microtubular network of the inner part of the cell, which can be better resolved by further spatially filtering the SICM image (b) which is overlaid with a tubulin fluorescence signal from the bottom plane of 3rd order 3D SOFI stack. Band-pass spatial filter with 2-8 px range was used applied on the image (a). (c) Final 3D rendering in Blender 3D software with an overlaid SOFI and SICM data.

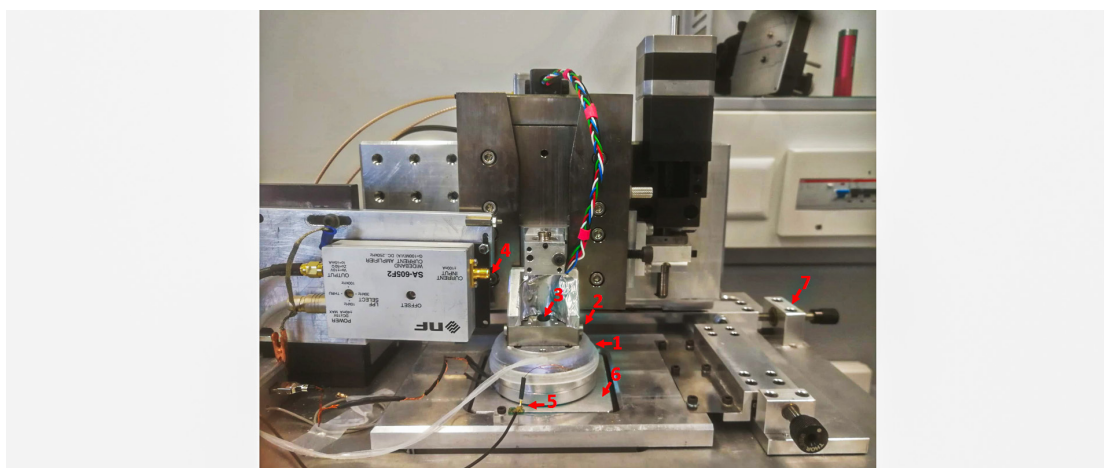


Figure 2.21 – SICM setup with an environmental control chamber for live cell imaging described in detail previously(139) 1) Mini-incubator for environmental control. 2) Pipette actuator. 3) Pipette inlet. 4) TIA input for the pipette electrode. 5) Bath electrode. 6) XY scanner. 7) Translation stage.

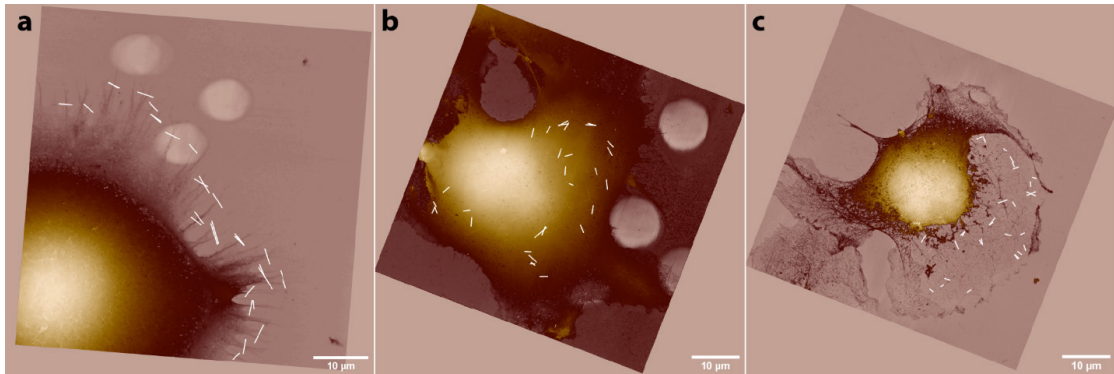


Figure 2.22 – Cross sections used to calculate Pearson-correlation coefficient between different channels. For figure 2.5f 1D cross sections were manually depicted by selecting the structures of interest by hand. Filopodia (a), microvilli (b) and microtubules (c) were selected.

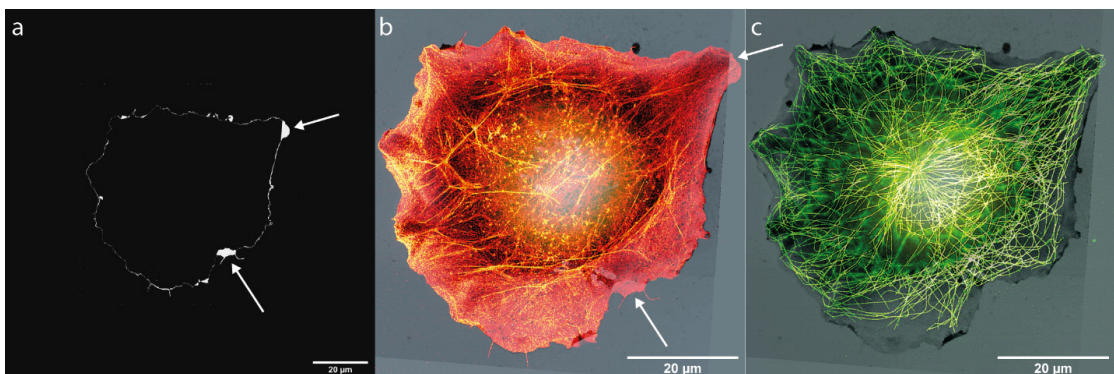


Figure 2.23 – SICM SOFI image co-registration procedure. (a) Difference of the thresholded SICM and actin channels revealing the different cell features between SICM and actin channels. (b) SICM image overlaid with actin and (c) channels. Arrows are showing the ambiguities marked in image (a). 2D SOFI images were aligned with SICM topographical map based on the actin channel. Same features were manually depicted in both images and affine transformation matrix was computed using at least 10 corresponding marks. 2D tubulin image was transformed using the same transformation matrix assuming that the lateral drift between two SOFI images is neglectable. 3D SOFI image stacks were processed in the same way expect in this case two-color stacks were aligned based on the brightfield microscopy by phase correlation using the images recorded before acquiring each of the stack.

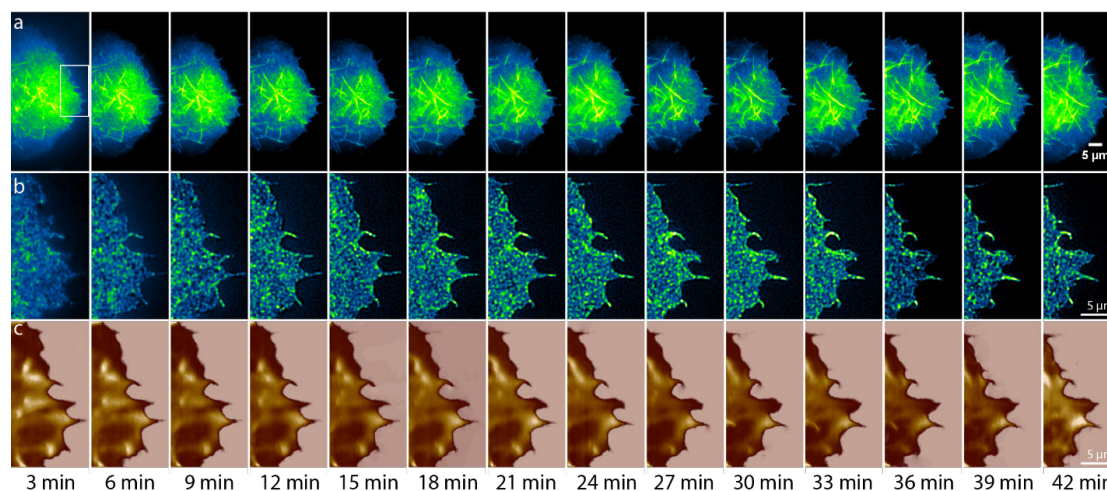


Figure 2.24 – Live-cell SICM-SOFI imaging of actin of filopodia for 42 min. Acquisition was performed consequently by recording $10\ \mu\text{m} \times 20\ \mu\text{m}$ SICM scans and 300 frame long fluorescence stacks for imaging photoactivated Lifeact-mEOS-2. Standard deviation image sequence (a) and 2nd order SOFI (b) aligned with SICM topography images (c) are shown. COS-7 cells were transfected as described in the Methods section by using a Lifeact-mEOS-2 plasmid and imaged after 24 h in FluoroBrite medium. $200\ \text{W}/\text{cm}^2$ of 561 imaging laser and $0.2\ \text{W}/\text{cm}^2$ of 405 nm activation laser were used for illumination with a corresponding exposure time of 50 ms. Corresponding SICM height maps were recorded at 200×100 pixels image (100 nm pixel size), acquired at a pixel acquisition rate of 200 Hz with a hopping height of $1\ \mu\text{m}$.

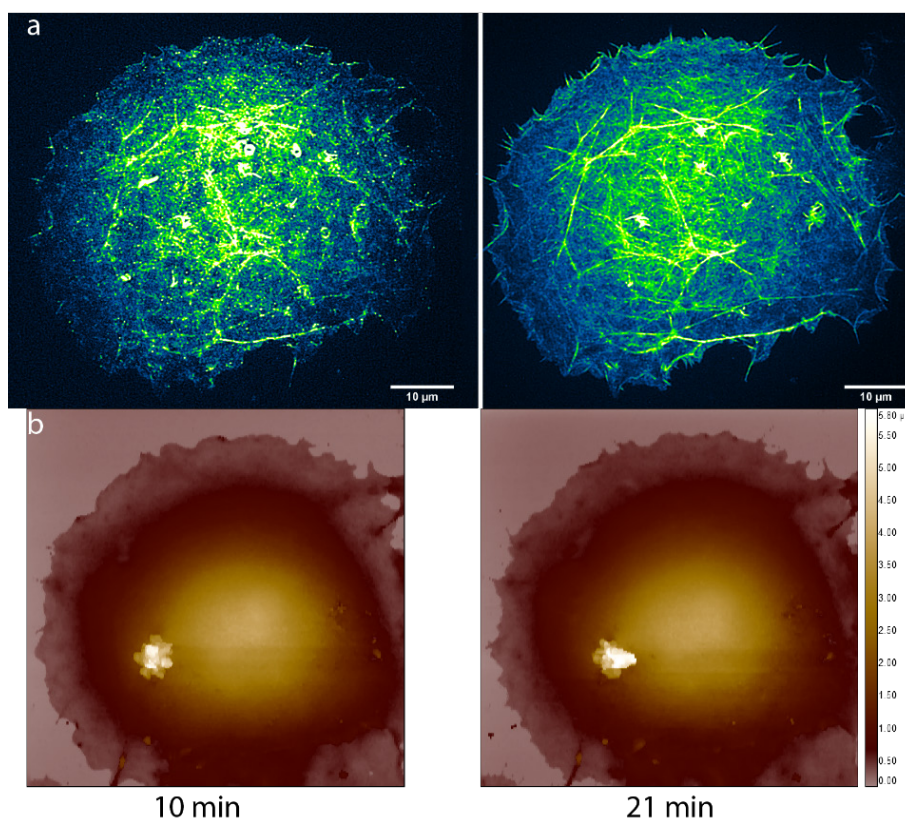


Figure 2.25 – Live-cell SICM-SOFI imaging of a single cell. Acquisition was performed consequently by recording $60\ \mu\text{m} \times 60\ \mu\text{m}$ SICM scans and 2 fluorescence stacks (300 and 1000 frames long) of photoactivated mEOS-2 for 2nd order SOFI computation. 2nd order SOFI (a) aligned with SICM topography images (b) are showed. COS-7 cells were transfected as described in the Methods section by using a Lifeact-mEOS-2 plasmid and imaged after 24 h in FluoroBrite medium. $200\ \text{W}/\text{cm}^2$ of 561 imaging laser and $0.2\ \text{W}/\text{cm}^2$ of 405 nm activation laser were used for illumination with a corresponding exposure time of 50 ms. White spot in the SICM image is most likely a particle, attached from the solution.

Chapter 2. Correlative 3D microscopy of single cells using super-resolution and scanning ion-conductance microscopy

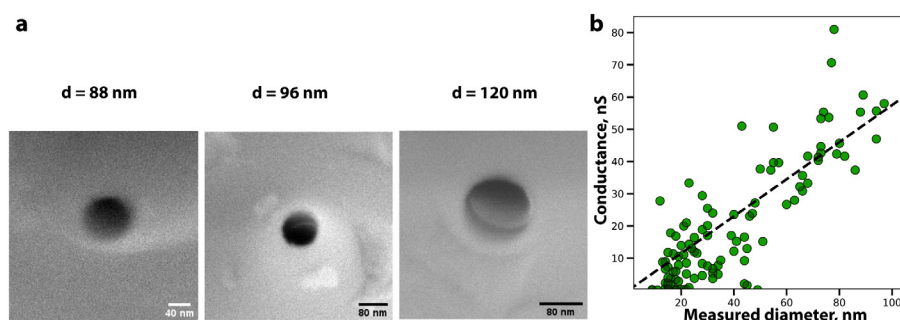


Figure 2.26 – SEM characterization of glass nanocapillaries. These SEM images are representative of more than 100 SEM images used to calculate the diameters of the pipettes plotted in (b). (b) Conductance measured in 400 mM KCl solution vs opening diameter measured with SEM (N=138). The dashed line represents a least-square fit of the model which was established in a previous study(119). The figure is adapted composed from the images and data published in our previous study(136)

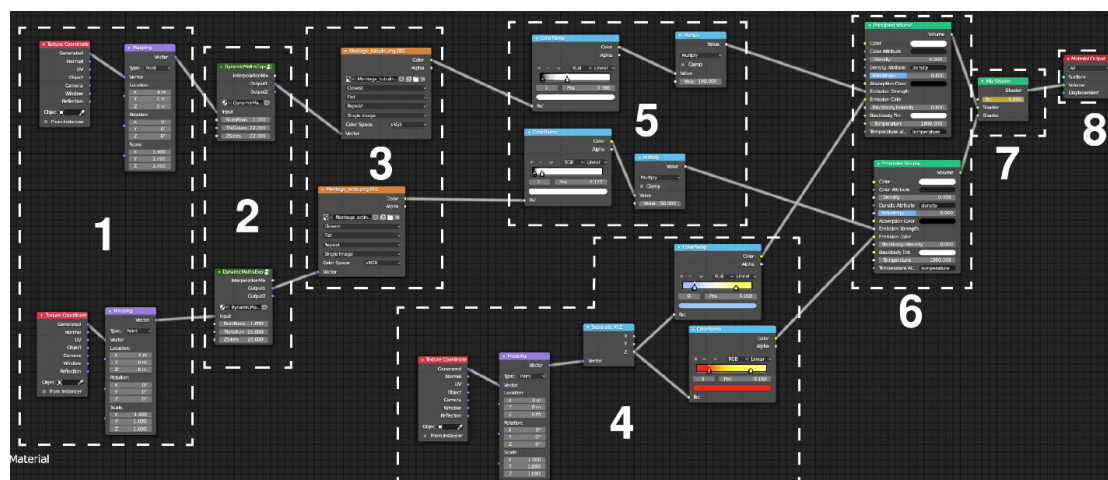


Figure 2.27 – Description of final 3D SOFI data visualization in Blender 3D. A simple cube was used as a volume corresponding to the 3D SOFI volume of $2.45\mu\text{m} \times 60\mu\text{m} \times 60\mu\text{m}$. Two separate colors were visualized in parallel. Different parts of the shader are explained as follows: 1) Setting up the texture coordinates 2) A script node used to make a 3D volume from the stack of SOFI images. Each image is represented as voxel with dimensions determined by a 3D cube 3) Input of a stack file 4) Color ramps used to represent the height in different colors 5) Contrast and intensity adjustment 6) A principled volume shader 7) A mix shader used to switch between tubulin and actin channels 8) A volume output node.

3 Adaptive optics enables multimode 3D super-resolution microscopy via remote focusing

The following chapter is based on the postprint of the following publication:

Vytautas Navikas¹, Adrien Descloux¹, Kristin S. Grussmayer^{1,2}, Sanjin Marion¹, Aleksandra Radenovic¹ **Adaptive optics enables multimode 3D super-resolution microscopy via remote focusing**, Journal of nanophotonics, 2021.

V.N. contributed to the paper by conceiving and refining general idea and writing the final manuscript with input from all the authors. V.N. prepared the cell samples, built the optical setup, performed all optical imaging experiments, image data analysis and final visualization. K.G. provided the adjusted protocols for sample preparation, A.D. gave advises to image processing pipeline and performed a custom image resolution estimation, S.M. advised on a Labview programming. A.R supervised the work.

¹Laboratory of Nanoscale Biology, Institute of Bioengineering, School of Engineering, Swiss Federal Institute of Technology Lausanne (EPFL), Lausanne, Switzerland.

²Current address: Grussmayer Lab, Department of Bionanoscience, Faculty of Applied Science and Kavli Institute for Nanoscience Delft, Delft University of Technology, Delft, Netherlands.

Abstract

A variety of modern super-resolution microscopy methods provide researchers with previously inconceivable biological sample imaging opportunities at a molecular resolution. All of these techniques excel at imaging samples that are close to the coverslip, however imaging at large depths remains a challenge due to aberrations caused by the sample, diminishing the resolution of the microscope. Originating in astro-imaging, the adaptive optics (AO) approach for wavefront shaping using a deformable mirror is gaining momentum in modern microscopy as a convenient approach for wavefront control. AO has the ability not only to correct aberrations but also enables engineering of the PSF shape, allowing localization of the emitter axial position over several microns. In this study, we demonstrate remote focusing as another AO benefit for super-resolution microscopy. We show the ability to record volumetric data ($45\mu\text{m} \times 45\mu\text{m} \times 10\mu\text{m}$), while keeping the sample axially stabilized using a standard widefield setup with an adaptive optics add-on. We processed the data with single-molecule localization routines and/or computed spatiotemporal correlations, demonstrating sub-diffraction resolution.

3.1 Introduction

Conventional light microscopy methods are inherently constrained in terms of their lateral and axial resolution due to the limited numerical aperture of the imaging apparatus and the finite wavelength of the fluorescence. During the past two decades, multiple approaches were developed to overcome this restriction by exploiting spatial and/or temporal separation of fluorescent emitters(106). In single-molecule localization microscopy (SMLM) the diffraction limit is circumvented by computationally fitting the point-spread function (PSF) of temporally separated single emitters. SMLM analysis requires a long sequence of sparsely blinking fluorophores in order to appropriately sample the labelled structure. This sequence is typically acquired with high illumination intensities and by using complex imaging buffers with oxygen scavenging systems(7) to minimize the bleaching or by using genetically encoded photo-switchable proteins(20). To speed up the acquisition procedure and perform imaging in varying fluorophore density environments, alternative computational approaches were developed(49; 61). For example, Super-resolution Optical Fluctuation Imaging (SOFI) relies on spatiotemporal correlations of the signal of independently blinking emitters. SOFI is particularly suitable to imaging samples with higher fluorophore densities and is less sensitive to varying blinking conditions(109). Both single molecule localization methods and SOFI are not restricted to 2D imaging. However, obtaining an axial resolution beyond the diffraction limit throughout the full thickness of adherent cells ($4\text{-}10\mu\text{m}$) is not usually achieved and requires a modified detection path(140).

In SMLM, one of the first and most common ways to retrieve information of the axial PSF position is the introduction of astigmatism in the detection path by using a cylindrical lens(141) or a wave-front shaping optical element such as a deformable mirror(142). Complex PSF

engineering techniques such as the Zernike optimized localization approach(143) allows the adjustment of the PSF for the extended Z-range (2-5 μm) in a trade-off of lateral localization precision and can, in theory, achieve isometric resolution. Other approaches such as opposing objective lenses (4Pi arrangement)(144) or interferometric SMLM(46) can achieve a sub-10nm axial resolution, but require a complex optical system design. To image samples thicker than 5 μm , Z-scanning is needed, which is typically achieved by physically moving either the sample or the objective axially with a piezoelectric stage. Alternatively, light-sheet illumination with Bessel beams can be used for structured sample illumination, increasing the axial resolution(145), but requiring a separate objective lens placed in close proximity to the sample(145; 146).

Furthermore, biplane imaging with 50:50 beam splitters or image splitting prisms in their extreme can be used to separate the detection path into multiple planes(147; 118; 148), thus enabling a simultaneous volume acquisition in exchange for signal-to-noise ratio. However, when imaging deeper into the sample, aberrations induced by the optical system distort the PSF and ultimately diminish the localization precision. This is a particular problem for high NA oil immersion objectives because of the refractive index mismatch between the imaging medium and immersion oil. Fortunately, these intrinsic aberrations, together with inhomogeneities in the refractive index of the biological sample volume, can be partially corrected by the use of adaptive optics(39).

To appropriately sample complex cellular structures, 3D-SMLM experiments are run for long durations ranging from a few hours(143) to multiple days(149), presenting a significant challenge in lateral and axial drift correction. Lateral drift is typically corrected in post-processing by tracking fiducial markers. On the other hand, axial drift correction requires an active feedback loop which is commonly achieved by measuring the lateral displacement of an infrared laser set up in total internal reflection(150), computing the three dimensional correlation between a previously recorded brightfield Z-stack in a separate imaging channel and a live brightfield image(151) or by tracking fiducial markers in three dimensions(152).

To perform a precise and continuous axial drift correction while imaging multiple Z-slices of the cell volume, commercially available complex Z-stabilization systems using movable offset lenses are needed to compensate for the changing distance between the objective lens and the coverslip. In the alternative approach, termed remote focusing, one changes the focus without moving either the objective or the coverslip. The approach involves shifting the image plane by optical defocussing using an adaptive optical element. This can be achieved at a few kHz rates by using a deformable mirror or an electrically tunable lens(153) and does not require movement of sample or objective(154).

Here, we demonstrate a combined application of AO in super-resolution microscopy by fusing point-spread function engineering, aberration correction and simultaneous rapid remote focusing. It enables us to record Z-stacks of whole COS-7 cells without moving the sample and keeping it axially stabilized for extended periods of time (here up to 2.5 hours). Fast remote

Chapter 3. Adaptive optics enables multimode 3D super-resolution microscopy via remote focusing

focusing also allows us to change the image planes frequently (maximum frequency of 100 Hz), thus homogeneously distributing the effect of bleaching in all the planes by revisiting the same imaging plane multiple times. Finally, we perform multiplane super-resolution microscopy by processing the data with different modalities by using SOFI, 2D SMLM and astigmatism-based 3D SMLM for further increased depth sampling with self-blinking fluorescent probes.

3.2 Results

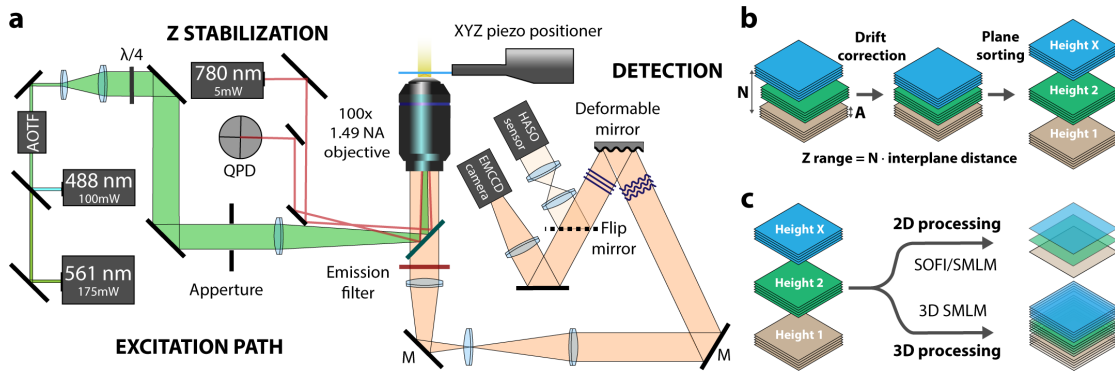


Figure 3.1 – Schematics of the optical setup and image processing pipeline. (a) Sample excitation was achieved by 2 continuous laser sources with independently modulated power by acousto-optic tunable filter. Laser beams were then expanded with a telescope and focused by a lens into the back focal plane of the 100x NA=1.49 oil immersion objective to achieve a widefield illumination of the sample. Fluorescence light was collected by the same objective and filtered using a combination of a dichroic mirror and 2 emission filters. The light is then passed through MicAO 3DSR adaptive optics setup which consists of a deformable mirror and a wavefront sensor. Light is then detected either by a wavefront sensor, which is used for a calibration of AO system or a water-cooled EMCCD camera with a back-projected pixel size of 105 nm. Total internal reflection of an infrared laser is used to axially stabilize the sample which is precisely positioned by the XYZ piezo stage thus eliminating the axial drift. (b) 3D image stacks were recorded by shifting the height using a deformable mirror every N number of frames in order to homogeneously distribute bleaching in all the planes. Fluorescent beads immobilized on a coverslip were imaged every A number of frames with a 488 nm laser line and then used for lateral drift correction (SI drift correction). For final processing image stacks were sorted based on focus values applied for each frame. (c) Sub-stacks were processed by using SOFI and SMLM routines published previously as described in Methods.

In order to demonstrate the advantages of our approach, we labelled microtubules in fixed COS-7 cells with a self-blinking Abberior FLIP-565 dye which does not need a complex imaging buffer for blinking and was used previously for SOFI(30) and SMLM(155; 156). A custom-built widefield microscope equipped with a high NA oil immersion objective and an adaptive optics addon was used for imaging as shown in Figure 3.1a and further explained in Methods. We were able to record Z-stacks by changing the focus remotely i.e. by adding or subtracting a specific amount of Zernike defocus mode (Z_2^0) via the deformable mirror, thus keeping the

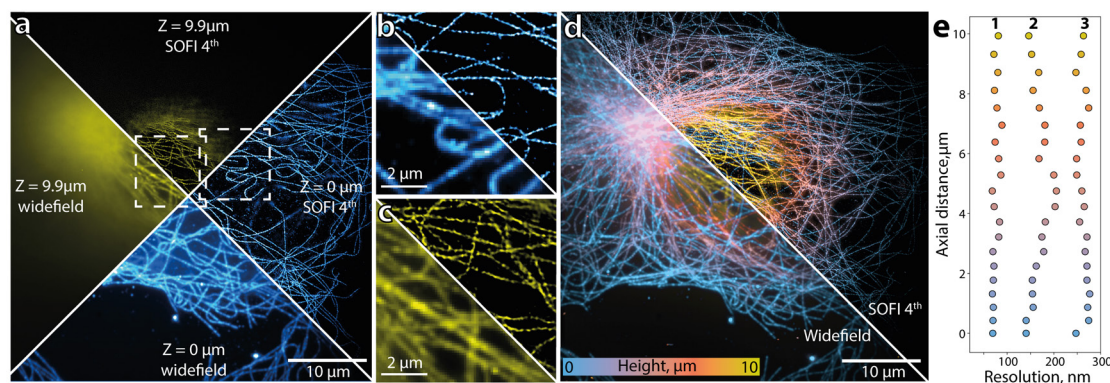


Figure 3.2 – Sequential-plane imaging with SOFI. (a) Images of tubulin of a COS-7 cell immunostained with Abberior FLIP-565 self-blinking dye acquired from different heights of 0 μm (blue) and 9.9 μm (yellow). A comparison of a widefield and SOFI 4th order images recorded at 0 μm (b) and 9.9 μm (c) indicates a clear contrast and resolution improvement provided by SOFI. (d) An overlay of 20 planes spaced with approx. 500 nm axial distance. (e) Lateral resolution dependency on height for different SOFI orders (1 – SOFI 4th, 2 – SOFI 2nd, 3 – widefield).

sample stationary by a closed-loop Z-stabilization system at all times. The stacks of blinking emitters were recorded in a predefined Z-range by shifting the focus every Δ (200-500) frames (Figure 3.1b). An image of the beads immobilized on the coverslip was taken after each such sub-sequence in order to estimate the lateral drift and correct it in post-processing (Figure 3.5). The drift-corrected stacks were then processed with 3 different super resolution processing algorithms (Figure 3.1c) in order to show the versatility of our method.

Z-stacks were first processed with the versatile SOFI approach(49) to demonstrate the multi-plane high-order SOFI imaging capability (Figure 3.2). Since the AO does not allow acquisition of several planes simultaneously, SOFI can only be computed along the lateral dimensions, plane by plane, resulting in a 2.5D volume. In comparison to simultaneous volume recording in a 3D SOFI approach with an image-splitting component(118; 110), the AO element allowed to achieve similar lateral resolution for deconvolved 4th order SOFI images (75 ± 6 nm compared to 78 ± 7 nm) within the higher axial depth in an exchange of longer imaging times (Figure 3.8). The stack consisted of 20 planes spaced approx. 500 nm apart with 6000 frames in total recorded for each plane. The distances between planes were estimated via additional calibrations using a bead stack recorded with a piezo actuator (Figure 3.6) as a reference. The stack was recorded by shifting the focus after 200 frames (10 s) in order to keep the bleaching effect homogenous within the whole volume (Figure 3.9) with an average bleaching lifetime of 54 ± 4 min due to the low laser power used (300 W/cm^2). We found that continuous tubulin structures were resolved in 4th order SOFI images within the whole 10 μm axial range (Figure 3.2) and without an observable difference in estimated image resolution (Figure 3.2b-e). To further demonstrate the versatility of our approach, the same image stack as in Figure 3.2 was processed with a SMLM approach by localizing emitters with a standard routine (See Methods

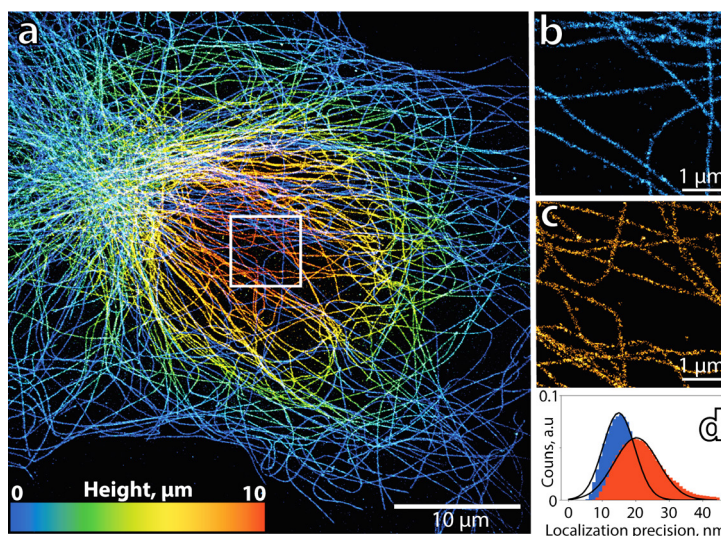


Figure 3.3 – Multiplane single-molecule localization microscopy. (a) A height coded render of 20 resolved planes spaced 500 nm apart. The same dataset as in Figure 3.2 was processed. (b-c) Zoom-ins from the bottom (b) and top (c) planes. (d) Localization precision histogram showing a localization precision difference of 5.3nm in the 10 μm axial range.

for more details). This allowed us to quantify the localization precision and density at different planes (Figure 3.11).

Furthermore, we observed a decrease (5.3 nm) of localization precision when comparing the localization precision histograms of the bottom (0 μm) and top planes (9.9 μm) (Figure 3.3). This decrease is likely due to wavefront distortions introduced by the sample causing additional aberrations and could be in principle corrected by using state-of-the-art *in-situ* image-based online aberration estimation algorithms(157) and correcting each Z-plane of the stack independently to gain maximum performance. Finally, samples were also imaged by adding 60 nm RMS astigmatism at 0° using the same DM to perform an astigmatism-based 3D SMLM with an AO. The calibration curves of the astigmatic PSF using 175 nm diameter beads were recorded at the bottom plane (Figure 3.10) and then used with a standard 3D SMLM routine. 11 slices with an axial distance of approx. 1 μm apart were imaged by changing the height in 300 frame intervals and recording 15000 frames for each Z-slice (165000 frames in total; \approx 2h 20min.). The final 3D stack (Figure 3.4, Figure 3.13) demonstrates the ability to perform astigmatism-based 3D SMLM within a 10 μm axial depth by using AO remote focusing. The height color-coded Z-slices near the bottom (0 μm - 0.8 μm) and top (8.4 μm – 9.2 μm) of the stacks displays the axial dynamic range. The 1 μm interplane distance used for a particular 3D stack resulted in a reduced number of localizations between the planes and sub-optimal Z-sampling, which can be improved by using smaller interplane distances (Figure 3.12a) at the cost of lateral sampling due to bleaching effects. Furthermore, lateral localization precision decreased from 29 nm to 38 nm per 8 μm of depth (Figure 3.12b), while the axial localization precision of 130 nm stayed similar through the depth range (Figure 3.12c. It is important to note

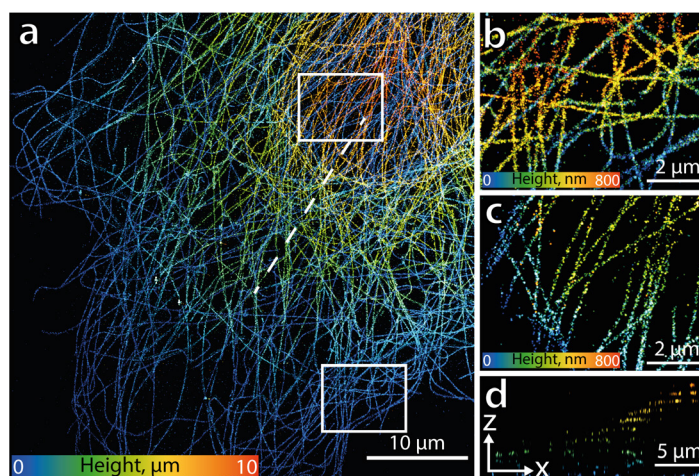


Figure 3.4 – Multiplane astigmatism-based single-molecule localization microscopy. (a) A height coded render of tubulin in a COS-7 cell immunostained with Abberior FLIP-565 self-blinking dye imaged by adding 60 nm RMS of astigmatism. (b-c) Zoom-ins from the bottom (b) and top (c) planes of the full image stack (d) A slice marked in (a) with a dashed line showing the axial profile of the whole volume consisting of 10 sub-volumes spaced with 1 μm distance.

that our choice of an Abberior FLIP-565 self-blinking dye was motivated by its flexibility for different super-resolution modalities, and this dye is sub-optimal for 3D SMLM experiments in terms of photon yield and average ON/OFF ratio(158). Localization precision may be improved by using brighter fluorescent probes such as Alexa647 under STORM conditions(37) allowing one to reach sub 20 nm lateral and axial localization precisions.

3.3 Conclusion

We demonstrated a proof-of-principle application of adaptive optics for multimode 3D super-resolution microscopy imaging over a 10 μm axial range with a deformable mirror for remote focusing combined with aberration correction for 2.5D SOFI and astigmatism-based 3D SMLM achieving subdiffraction resolution across all modalities. We have expanded the previously demonstrated astigmatism-based 3D SMLM(38; 39) using a deformable mirror to higher axial range by applying the focus mode in order to image multiple planes. A high axial range is important to visualize various biological structures such as cortical neurons(159). By exploiting the AO advantages for deep imaging with high-NA oil-immersion objectives, described in detail recently(39), we exploited the remote focus functionality to accommodate the ability to capture the whole cellular volume without moving the sample. Our approach can be easily applied to existing setups equipped with DMs, simplifying acquisition and Z-stabilization of high-resolution 3D image stacks via multiple super-resolution microscopy modalities requiring long acquisition times such as DNA-PAINT(160) and Exchange-PAINT(161), further automating the imaging process. Compared to biplane or multifocal SMLM imaging approaches

using image splitting elements(148), the emission signal is not divided, thus preserving the signal-to-noise ratio and remaining flexible in terms of interplane distance and imaging depth, which can be further extended to perform SMLM in tissues(157; 162). Furthermore, the image-based wavefront calibration procedure can also be improved to account for distortions further away from the image center(39) by using global optimization techniques(157), enabling correction of sample-induced aberrations through the whole available field-of-view. From the data analysis standpoint, novel deep-learning approaches can further refine our technique by improving the accuracy of the localization(60) or reducing the number of frames needed for image reconstruction(59). We believe that our study will foster the use of adaptive optics in modern fluorescence microscopy for biological applications requiring high-throughput and high-resolution imaging.

3.4 Methods

3.4.1 Setup

Imaging was performed on a custom-built microscope(163) (Figure 3.1a). 100 mW 488 nm (Sapphire, Coherent) and 100 mW 561 nm (Excelsior, Spectra Physics) continuous lasers were used for excitation. Laser beams were combined using a dichroic mirror (T495lpxr, Chroma) and passed through an acousto-optic tunable filter (AOTF_{nC-VIS-TN}, AA Opto Electronic), which is used to modulate the power of both lasers independently. Beams were passed through an achromatic $\lambda/4$ plate (AQWP05M-600, Thorlabs), expanded with a 10x telescope ($d = 12\text{mm}$) and focused with a $f = 300\text{mm}$ lens into the back focal plane of the objective mounted on an inverted optical microscope (IX71, Olympus). 100x oil-immersion objective (UApo N $\times 100$, Olympus) with a numerical aperture of 1.49 was used for imaging. Fluorescence signal collected by the objective was filtered using a combination of a quad-line dichroic mirror (R405/488/561/635, Chroma) and two emission filters: quad-line (446/523/600/677 HC Quadband, Semrock) and band-pass (596/83, Chroma). Fluorescence is then passed into the adaptive optics addon (MicAO 3DSR, Imagine Optic) where the back focal plane of the objective is conjugated to a deformable mirror (MIRAO 52-e, Imagine Optic). A flip mirror is used to deflect the light either to a Shack-Hartmann wave-front sensor (HASO3, Imagine Optic) or to an EMCCD camera (iXon DU-897, Andor). The camera was water-cooled with a custom-built water-cooling system to prevent vibrations from the camera fan. The motorized XYZ stage (MS-2000, ASI) was used for coarse positioning of the sample, with a XYZ piezo stage (LPS Series, Mad City lab) for fine XYZ positioning including axial sample stabilization. For the home-built Z-stabilization system, a collimated beam from a 785 nm laser diode (Thorlabs, LPS-785-FC) was focused on the back focal plane of the objective far from the optical axis in order to undergo total-internal reflection from the sample-coverslip interface(150). IR reflection was filtered with a band-pass filter (FL780-10, Chroma) and deflected on a quadrant photo diode (QPD, Pacific Silicon QP50-6SD2). The QPD signal is used in the PID controller implemented in Labview, which forms a closed-loop system with the piezo stage and ensures the Z-stabilization of the sample. The whole setup, including the deformable mirror was

controlled with a custom LabView program.

3.4.2 Sample preparation

Cells were cultured in DMEM high glucose without phenol red medium (Gibco, Thermo Fisher Scientific), containing 10% fetal bovine serum (Gibco, Thermo Fisher Scientific), 1% penicillin-streptomycin (Gibco, Thermo Fisher Scientific) and 4 mM L-glutamine (Gibco, Thermo Fisher Scientific) at 37 °C and 5% CO₂. Cells were detached from a flask with TrypLE (Gibco, Thermo Fisher Scientific) and seeded on 25 mm coverslips coated with fibronectin. Cells were grown overnight (12-16 h) before fixation in 6-well plates. During fixation, coverslips were incubated for 90 s in a prewarmed microtubule extraction buffer, consisting of 80 mM PIPES, 7 mM MgCl₂, 1 mM EDTA, 150 mM NaCl and 5 mM D-glucose with a pH adjusted to 6.8 using KOH with 0.3% (v/v) Triton X-100 (AppliChem) and 0.25% (v/v) EM-grade glutaraldehyde (Electron Microscopy Sciences). The solution was exchanged to pre-warmed 4% paraformaldehyde dissolved in PBS (pH=7.4) and samples were incubated for 10 min at room temperature. Afterwards, samples were washed three times for 5 min with PBS on an orbital shaker. Cells were kept for 5 min with a freshly prepared 10 mM NaBH₄ solution in PBS on an orbital shaker in order to reduce background fluorescence. This step was followed by a rinse in PBS, and two washes of 10 min in PBS on an orbital shaker. Samples were then additionally permeabilized to ensure antibody penetration with 0.1% (v/v) Triton X-100 in PBS (pH=7.4) on an orbital shaker followed by an additional wash with PBS. Finally, samples were blocked with freshly prepared blocking buffer consisting of 2% (w/v) BSA, 10 mM glycine, 50 mM ammonium chloride NH₄Cl in PBS (pH=7.4) for 60 min at room temperature or stored overnight at 4 °C for further staining. All chemicals were bought from Sigma Aldrich unless stated differently. After blocking, samples were incubated with 2% (v/v) primary anti-tubulin antibody (clone B-5-1-2, Sigma-Aldrich) in blocking buffer for 60 min at room temperature. Samples were washed with blocking buffer thrice for 5 min on orbital shaker. Coverslips were incubated with 2% (v/v) secondary donkey anti-mouse-Abberior FLIP-565 antibody, which was labelled as described previously²⁶. Samples were kept in blocking buffer for 60 min and washed thrice for 5 min on orbital shaker. Samples were incubated for 10 min in 2% (w/v) PFA in PBS (pH=7.4) as a post-fixation step followed by three 5 min washes with PBS on an orbital shaker. After staining, samples were incubated with a 1% fluorescent (Ex. 505/ Em. 515 nm) 175 nm diameter beads solution (PS-SpeckTM, Invitrogen) for 10 min and then washed with PBS. Finally, PBS (pH=7.4) was saturated with argon by passing the gas through the solution for at least 1h, thus reducing the O₂ concentration to ≈ 0.01 ppm in order to prevent photobleaching of the fluorophore. The degassed buffer was subsequently used for imaging in a closed imaging chamber.

3.4.3 *In vitro* imaging and calibration routines

The AO system was pre-calibrated before starting imaging experiments using a routine provided by the manufacturer (Image Optic). For the calibration, we imaged an isolated 1 μ m bead immobilized on a surface while operating the DM in a closed-loop mode with the Shack-

Chapter 3. Adaptive optics enables multimode 3D super-resolution microscopy via remote focusing

Hartmann wavefront sensor to establish an interaction matrix, which was further used for routine image-based indirect calibration. Before acquiring each Z-stack, the PSF of an isolated 175 nm fluorescent bead immobilized on a surface was imaged with the 488 nm laser and it was used to correct aberrations in each field-of-view. MicAO software (Image Optic) was used with an integrated 3N algorithm(164) which exploits a maximum contrast as an optimization metric to correct for the wavefront distortions by finding the amplitudes of selected first 15 Zernike modes. After correction, the mirror shape was used with a custom-written Labview program controlling the microscope. For each mirror shape a z-stack of the beads in agarose gel was recorded to calibrate the axial shifts induced by the DM (Figure 3.6). In order to correct the lateral field-of-view (FOV) distortion, the beads immobilized on the surface were imaged with different focus values added with a DM (Figure 3.7). For Abberior FLIP-565 imaging a 561 nm laser was used for excitation with a power ranging from 300 W/cm^2 for regular imaging to 1400 W/cm^2 for astigmatism-based imaging. Exposure time in all experiments was 50 ms, using an EM gain of 150. The Z-stacks with remote DM focussing were typically recorded within the $10 \mu\text{m}$ range, due to the thickness of the cells by adding a specific amount of defocus on top of the mirror shape. The Z-stacks were recorded by specifying the number of equally spaced planes (N) within the selected range. The number of frames (A) and the number of repeats (B) for the whole axial range were specified, resulting in the total number of $N \cdot A \cdot B$ frames per volume. After each A frames-long sequence, the DM was set to 0nm position and the image of beads were taken with 488nm laser for a lateral drift correction in post-processing (Figure 3.5). For astigmatic-based 3D SMLM imaging, 60 nm root-mean-square (RMS) of astigmatism was added using the DM. The RMS value in nm describes the amplitude of the Zernike coefficient, which is the total amount of RMS displacement of the mirror with a respect to a flat surface. Furthermore, the 60nm RMS of 3rd order spherical aberration per $10 \mu\text{m}$ of depth was linearly added in order to compensate for spherical aberration resulting from the refractive index mismatch between water and the objective's immersion oil based on the calibration (165) provided by a manufacturer. Finally, the exact values of the focus applied on the DM were saved to a separate file for image stack sorting.

3.4.4 Image processing

Acquired image stacks were sorted based on the input defocus values and drift-corrected based on the acquired bead stacks (Figure 3.5). Stacks were processed based on the acquisition mode used for imaging. Z-stacks without added astigmatism were processed with a 2D SOFI algorithm implemented in Matlab based on the previous work(52) or with SMLM software Thunderstorm(62) by using the integrated Gaussian PSF model and weighted least-squares fitting method. 2D SMLM stacks were filtered by removing localizations with lateral uncertainty $> 45 \text{ nm}$ and sigma values $< 80 \text{ nm}$ or $> 140 \text{ nm}$. Stacks with 60nm RMS of added astigmatism were also processed with the Thunderstorm 3D localization routine. For final figures, localizations were filtered by removing localizations with lateral uncertainty $> 45 \text{ nm}$ and axial uncertainty $> 100 \text{ nm}$. SOFI images were deconvolved with a Lucy-Richardson deconvolution algorithm with 25 iterations using gaussian PSF model. For data with added astigmatism, an

elliptical Gaussian model was used with weighted least square fitting method. The intrinsic axial shift between different planes was corrected by estimating the axial shift for each mirror shape by using a bead stack recorded with the piezo in agarose as a reference (Figure 3.6) while the lateral FOV distortion was corrected for each height plane as described in Figure 3.7. Final SMLM images were also rendered in Thunderstorm software by using the Averaged shifted histogram method with 10.5 nm pixel size. Localization precision was estimated in Thunderstorm software as well by using a 12.26 photoelectrons per count conversion factor calculated from the experimental photon transfer curve.

3.5 Acknowledgments

V.N. and A.R. acknowledge the Max-Planck EPFL Center for Molecular Nanoscience and Technology as well as NCCR in Biomaterials. V.N. is grateful for Flavien Colaço for the help in Labview programming and Audrius Jasaitis from Imagine Optic for technical assistance with the AO setup. A.R. and A.D acknowledge the support of the EPFL Open Science fund.

3.6 Supporting information

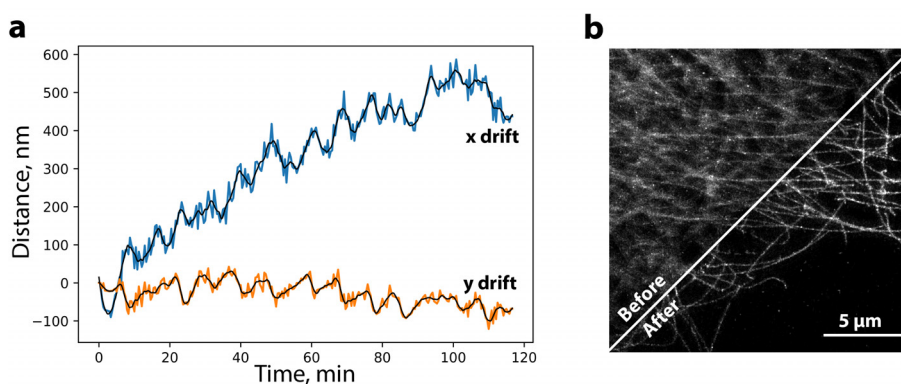


Figure 3.5 – Lateral drift correction with fiducial markers. (a) Lateral x (blue) and y (orange) drift over a total imaging time of 2h. Black lines represent the smoothed signal with a smoothing window of 4.1 min. The smoothed signal was used for correction. (b) Max projection of 3D SMLM stack before and after drift correction, showing the apparent visual improvement.

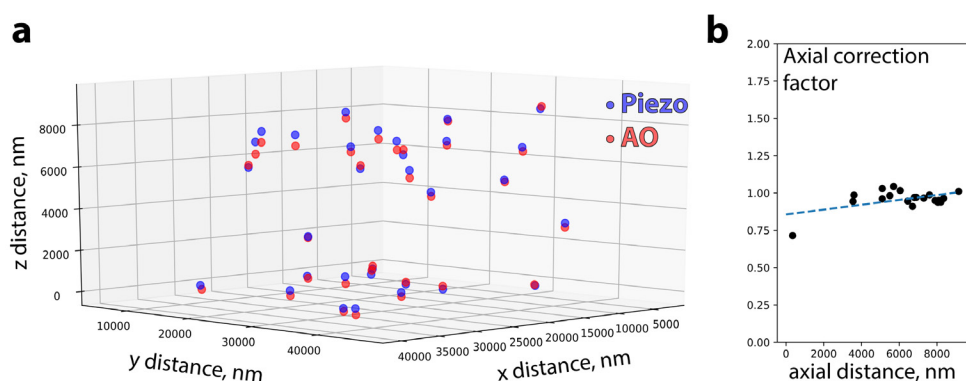


Figure 3.6 – Axial calibration with fluorescent beads. (a) Cumulative 3D localizations from multiple fields of view. The bead sample for axial calibration was prepared in 1% agarose. The beads covered the surface of the coverslip, which was used to align different ROIs axially. The bead stacks were acquired with a piezo stage and by using adaptive optics by adding a constant amount of focus mode. The centers of the beads were subsequently localized in 3D for each ROI (N=6) and the position of the bottom bead was subtracted. Finally, the nearest neighbor for each bead was found between 2 stacks (piezo and AO) and the difference in axial position. (b) Axial calibration factor (blue line) used to correct axial positions for each plane.

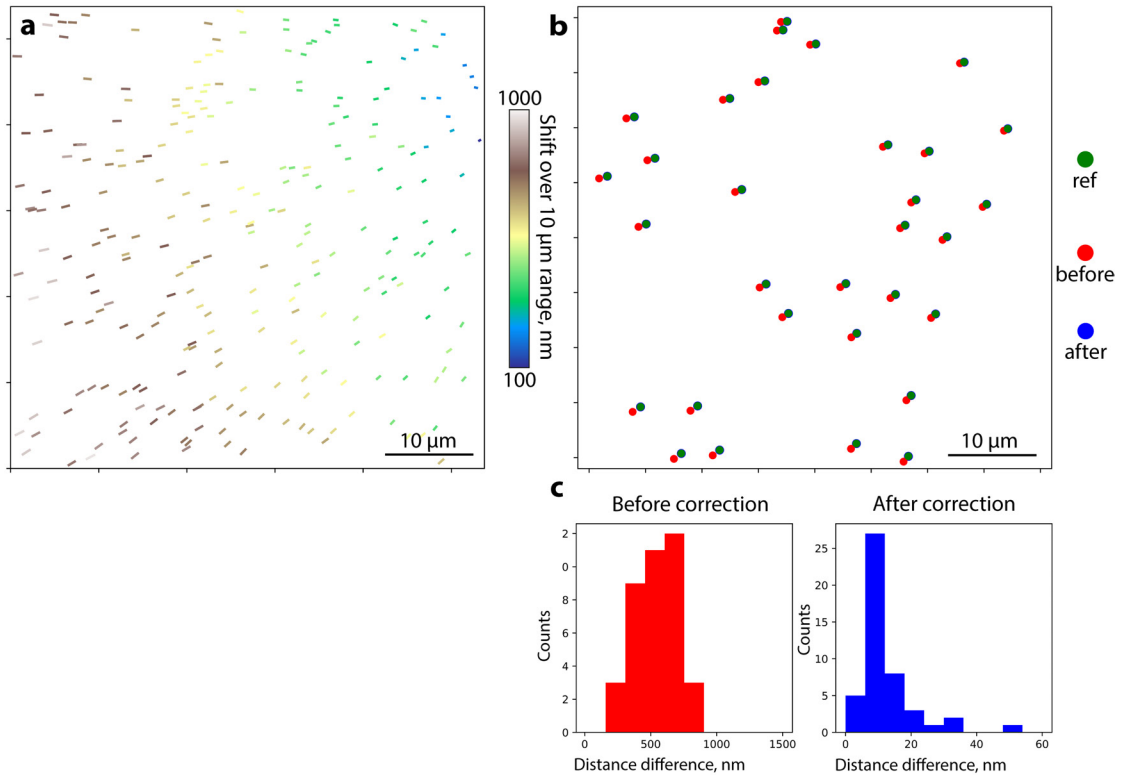


Figure 3.7 – Lateral image distortion correction. Correction of the lateral image distortion. To obtain the image transformation matrix we have added a different focus mode values with a deformable mirror (0 µm, 2 µm, 4 µm, ..., 10 µm) and refocused the sample with a motorized stage to obtain the image stack with 6 different heights. The bead sample was imaged allowed us to quantify the positions of the beads with the precision far beyond the diffraction limit. An average localization uncertainty of 6.1 ± 1.2 nm was measured. We have found that the remote focus with DM indeed induced the nonlinear deformation over the large ($53.76 \mu\text{m} \times 53.76 \mu\text{m}$) field-of-view (FOV) which was observed as a shift of the bead lateral position (a). The FOV deformation scaled linearly over the 10 µm focus range and was repeatable over the different samples and for different mirror shapes. We speculate, that this shift is caused by the slight misalignment in the optical system itself. However, the distortion was straightforwardly corrected for each plane using a piecewise affine image transformation, which was able to correct the positions of the beads (lateral positions at 0 µm and 10 µm are compared) with a precision of $(12.8 \pm 8.6 \text{ nm})$ compared to $(541.7 \pm 154.8 \text{ nm})$ without the correction applied (b-c).

Chapter 3. Adaptive optics enables multimode 3D super-resolution microscopy via remote focusing

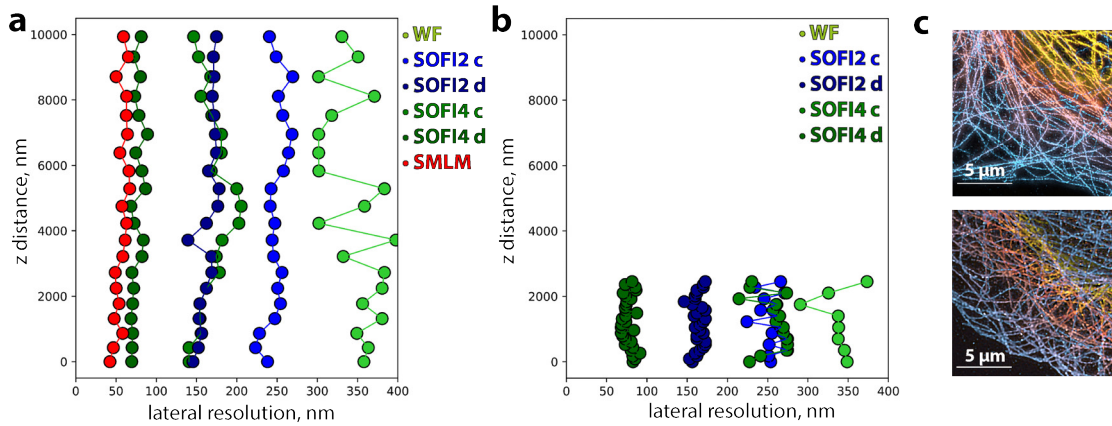


Figure 3.8 – Image resolution comparison. (a) Lateral image resolution per each height plane was estimated with previously published algorithm(4). Raw SOFI cumulants for 2nd and 4th orders (SOFI2c and SOFI4c) and deconvolved SOFI images for 2nd and 4th orders (SOFI2d and SOFI4d) are shown. Furthermore, resolution was also estimated for SMLM reconstruction from Figure 3.3 (SMLM), using bilinear histogram rendering (<https://github.com/Ades91/ImDecorr>). WF resolution values fluctuate due to a low SNR. (b) Corresponding resolution estimates were also done for the 3D SOFI approach published previously(118; 30) using the exact same sample preparation procedure. (c) Deconvolved 4th order SOFI images are shown for both imaging approaches (Adaptive optics SOFI 2D – Top) and (3D-SOFI) bottom. This comparison needs to be interpreted with additional caution and is valid only considering both modalities' intrinsic pros and cons, not just comparing the resolution values directly. Multiplane SOFI imaging was performed with a setup published previously(118; 30). For imaging with adaptive optics, a higher NA objective was used (NA 1.49 compared to NA 1.2), which also contributes to image resolution. On the other hand, an EMCCD camera was used for AO imaging, and an sCMOS for 3D SOFI and it is known that SOFI performs significantly better(166) with sCMOS cameras. Furthermore, the imaging intensity used for 3D SOFI was significantly higher (0.3 W/cm^2 compared to 3.5 W/cm^2). It is also important to note that simultaneous SOFI-3D imaging is significantly faster and allows increased depth sampling by computing inter-plane cross-cumulants, thus providing faster volume acquisition times, however, limited in terms of photobleaching due to the higher laser powers used and it has a fixed Z-range.

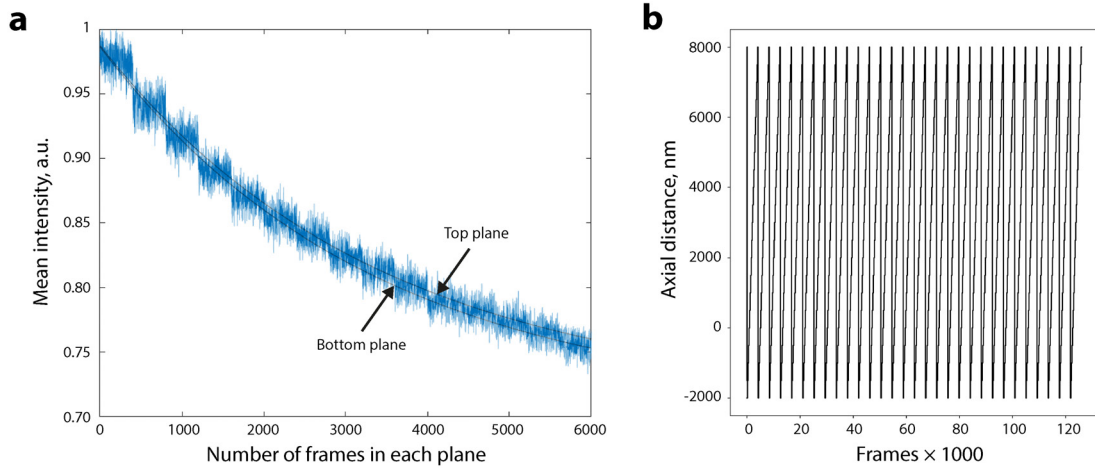


Figure 3.9 – Homogeneous imaging volume bleaching. (a) Bleaching curves for the top and bottom planes spaced $9.9 \mu\text{m}$ apart. Bleaching lifetimes were estimated by calculating the lifetime for each plane and multiplying by the total number of planes recorded ($N=21$). The average lifetime was 54.01 ± 4.76 min which is due to low laser illumination intensity used (300 W/cm^2) and a degassed PBS buffer used. (b) The amount of focus applied with AO over time. The imaging plane was changed every 300 frames (15s) to homogenize the bleaching over the whole image stack.

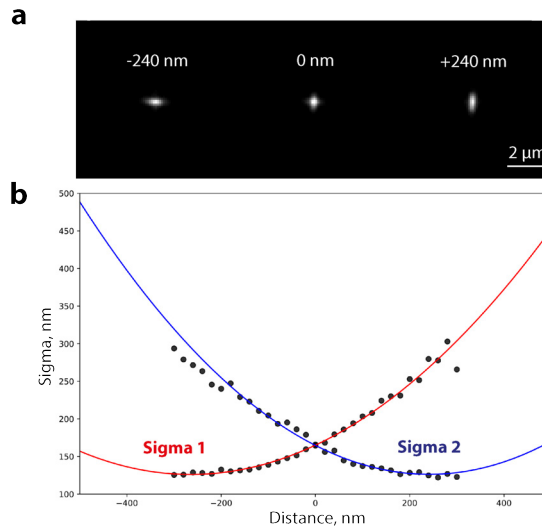


Figure 3.10 – Z-calibration of astigmatic PSF. (a) Bead image at different heights (b) PSF's Sigma calibration curve.

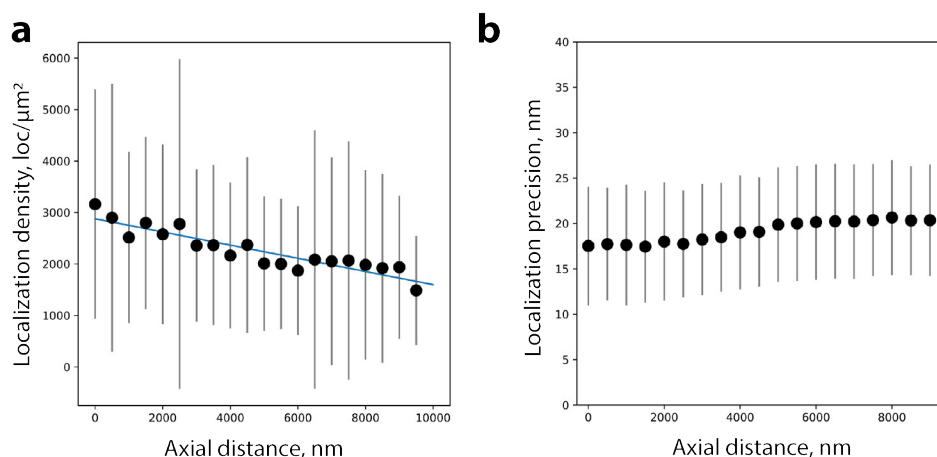


Figure 3.11 – Localization density and localization precision. (a) Localization density for each plane in Figure 3.3 displayed as $\text{mean} \pm \text{std}$. Localization density was estimated from localization maps with removed duplicate molecules based on localization uncertainty. The data was further thresholded based on density to remove background localizations and the final estimation was done with kNN approach using a KDTree algorithm to get the number of neighbours for each molecule within 20nm search radius. The final value is adjusted for area and $\text{mean} \pm \text{std}$ values are plotted. (b) Localization precision plot ($\text{mean} \pm \text{std}$) for each image plane in Figure 3.3

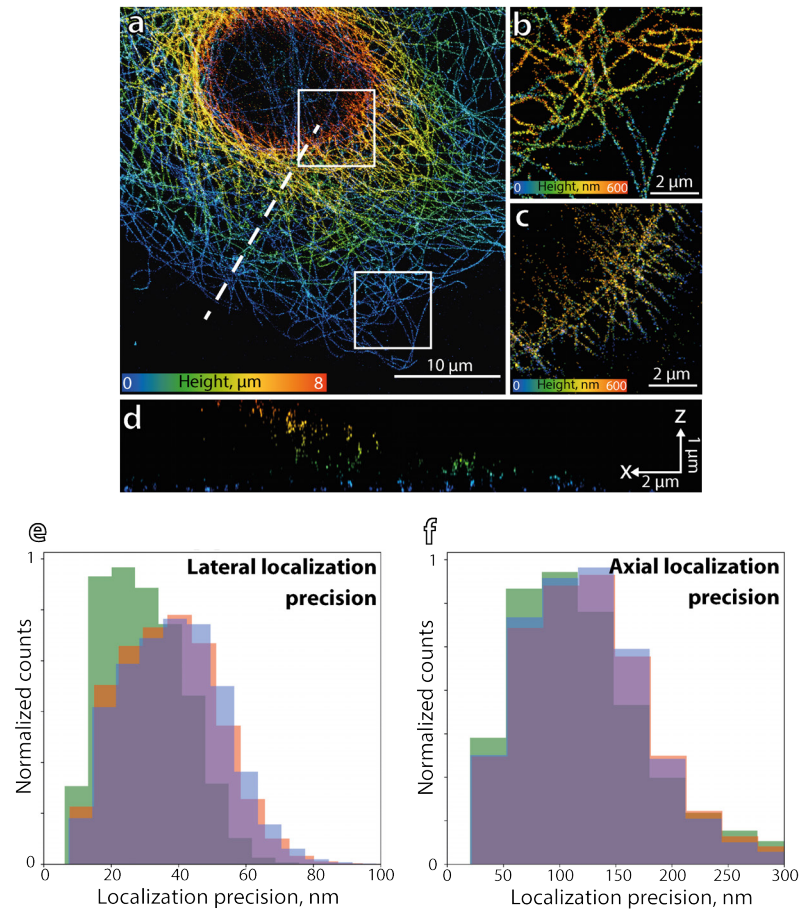


Figure 3.12 – Multiplane astigmatism-based single-molecule localization microscopy with 300nm interplane distance. (a) A height max intensity projection of tubulin in a COS-7 cell immunostained with Abberior FLIP-565 self-blinking dye imaged by adding 60 nm RMS of astigmatism. (b-c) Zoom-ins from the bottom (b) and top (c) planes of the full image stack (d) A slice marked in (a) with a dashed line showing the axial profile of the whole volume consisting of 27 sub-volumes spaced with 0.3 μm distance. (e-f) Lateral and axial localization precisions estimated with a Thunderstorm routine. The precision values are similar to the previous work(156).

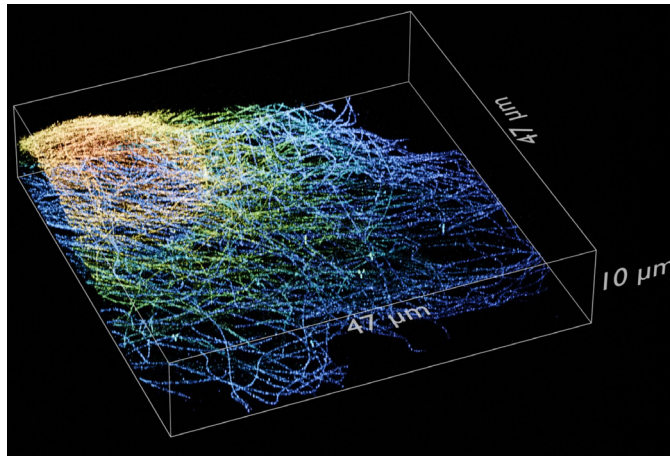


Figure 3.13 – Astigmatism-based 3D SMLM volume. The localized volume was rendered in Blender 3D by using image planes spaced 50nm apart rendered with Thunderstorm(62) plugin. The final rendering was done with cycles rendering engine by using a volumetric rendering functionality.

4 High-Throughput Nanocapillary Filling Enabled by Microwave Radiation for Scanning Ion Conductance Microscopy Imaging

The following chapter is based on the postprint of the following publication:

Vytautas Navikas¹, Samuel M. Leita², Sanjin Marion¹, Sebastian James Davis¹, Barney Drake², Aleksandra Radenovic¹, Georg E. Fantner². **High-Throughput Nanocapillary Filling Enabled by Microwave Radiation for Scanning Ion Conductance Microscopy Imaging**, ACS Appl. Nano Mater. 2020, 3, 8, 7829–7834.

V.N. contributed to the paper by conceiving and refining general idea and writing the final manuscript with input from all the authors. V.N. also fabricated and characterized nanocapillaries and analyzed the data. S.L. Performed electrical and SICM measurements. S.M., S.D. contributed by providing valuable input on data analysis. B.D and S.L. built the SICM setup. A.R and G.E.F. supervised the work.

¹Laboratory of Nanoscale Biology, Institute of Bioengineering, School of Engineering, Swiss Federal Institute of Technology Lausanne (EPFL), Lausanne, Switzerland.

²Laboratory for Bio- and Nano-Instrumentation, Institute of Bioengineering, School of Engineering, Swiss Federal Institute of Technology Lausanne (EPFL), Lausanne, Switzerland.

Abstract

Solid-state nanopores provide a highly sensitive tool for single-molecule sensing and probing nanofluidic effects in solutions. Glass nanopipettes are a cheap and robust type of solid-state nanopore produced from pulling glass capillaries with opening orifice diameters down to below tens of nanometers. Sub-50 nm nanocapillaries allow an unprecedented resolution for translocating single molecules or for scanning ion conductance microscopy imaging. Due to the small opening orifice diameters, such nanocapillaries are difficult to fill with solutions compromising their advantages of low cost, availability and simplicity of the experiment. We present a simple and cheap method to reliably fill nanocapillaries down to sub-10 nm diameters using microwave radiation heating. Using a large statistic of filled nanocapillaries we determine the filling efficiency and physical principle of the filling process using sub-50 nm quartz nanocapillaries. Finally, we have used multiple nanocapillaries filled by our method for high-resolution scanning ion conductance microscopy imaging.

Introduction

Solid-state nanopores are a promising new tool to study various biochemical interactions at the molecular scale(167; 168). In order to perform sensing, an electric potential is applied through a small pore. The sensing is based on the localized conductance drop which depends on the ionic concentration, surface charge, volume and shape of the pore (169; 170; 171). Solid-state nanopores tend to have higher current stability than their biological counterparts, since biological nanopores are limited by the membrane stability, which can be affected and ruptured by electroporation at high bias voltages (200-300 mV)(172; 173). Silicon dioxide nanocapillaries are one of the most widely used platforms for various bio-sensing applications such as single protein detection(174), DNA folding sensing(175), DNA-protein interactions(176), ect. Besides bio-sensing applications from the bulk solutions, the sharp and highly conical geometry of silicon-dioxide nanocapillaries is advantageous for various surface scanning applications and they are typically used for scanning ion conductance microscopy (SICM)(71). Further developments of the SICM technique were used to probe surface charge(177) and surface stiffness (178). Similarly, as for nanopore sensing, the main parameter that determines the resolution of SICM methods is the radius of a nanopore(117), so small nanocapillaries are preferably used. However, glass nanocapillaries under 50 nm are problematic to fill with aqueous solutions.

The common method to fill sub-50 nm nanocapillaries is the use of commercially available capillaries with a glass-filament inside. However, this alters the conical geometry of a nanocapillary. Another method is to prefill the capillaries with a solution with a lower surface tension like ethanol(179), and then to exchange the solution back to an aqueous electrolyte. This exchange procedure takes a long time, which depends on the length of the capillary tip, and can cause clogs or additional nonlinearities in the capillary conductance. Finally, ethanol to water exchanges foster the formation of nanobubbles on contaminated or hydrophobic

surfaces(180) that can significantly increase ionic current rectification and induce measurement artefacts.

As a consequence, several nanocapillary filling techniques have been developed to fill sub 50 nm nanocapillaries directly with the final solution of interest without prefilling steps. The first, heating based, approach called dynamic microdistillation, relies on selective heating of the nanocapillary tip with a heat applied from a conductive coil. Using this technique, sub-20 nm capillaries were successfully filled (181). However, this method is low-throughput and requires precise handling of fabricated nanocapillaries. Alternatively, a microcentrifugation approach was also used to fill 30-200 nm wireless nanocapillary based electrodes (182), which has similar limitations. Recently, a second thermally-driven approach has been shown to simplify the filling procedure and increase throughput to tens of nanocapillaries. The procedure is based on the fact that a temperature gradient between the tip and the body of the capillary varies the surface tension and drive the movement of small bubbles out of the capillary(183). This method requires keeping capillaries for tens of minutes at a high temperature which is incompatible with solvents that evaporate and alter the conductivity of the buffer. The method demonstrated 100 % filling efficiency based on brightfield microscopy images. Further electrical measurements are needed to evaluate the electrical signal of filled nanocapillaries by measuring conductance and rectification values.

This work aims to provide an accessible and robust filling method for glass nanocapillaries in the below 100 nm size range. We demonstrate a fast and high throughput method using easily accessible microwave radiation which is faster than methods published previously and has a 85.9 % filling rate calculated based on electrical measurements, while optical inspection gives the 100 % filling rate. We correlate the imaged size of these nanocapillaries with their electrical conductance and rectification factor to give additional insights into the resulting electrical signal quality. Furthermore, we apply the fabricated nanocapillaries for scanning ion conductance microscopy imaging and compare the image quality of different diameter nanocapillaries.

4.1 Results and discussion

Our batch nanocapillary filling procedure is based on microwave radiation induced rapid heating of the solution in which capillaries are immersed. As shown in the schematic Figure 4.1, capillaries were first placed in the filling solution bath, glued on a glass slide for improved handling. Due to high surface physisorption affinity to water molecules after oxygen plasma treatment, aqueous solution filled the very tip of a 47 nm nanocapillary (Figure 4.1a) by immersing capillaries into solution. As the capillary is tapered, the liquid easily fills the narrow tip due to increased capillarity, P_c until Laplace pressure is in equilibrium with the local pressure due to the local widening. This is explained by the Young-Laplace equation (Eq. 1):

$$P_c = \frac{2\sigma_{gs} \cos \theta}{r}$$

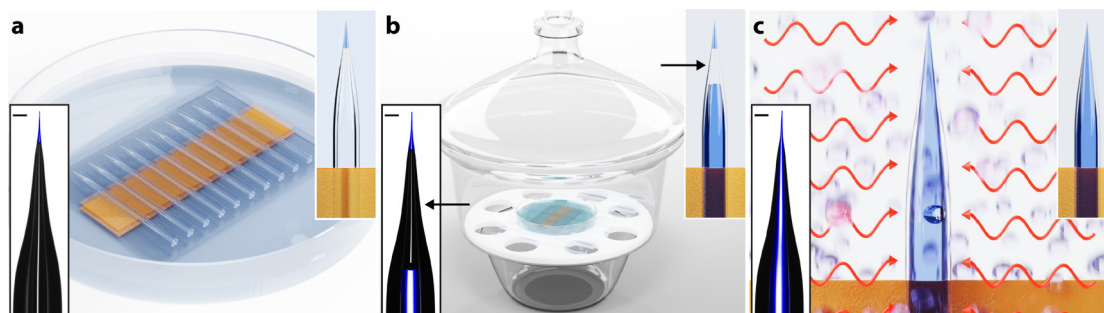


Figure 4.1 – Schematics and microscopy images of the method, sequentially used for filling nanocapillaries. Brightfield microscopy images of the same capillary in different steps are displayed on the bottom left in each panel. The solution is false-colored in blue, scale bar in each image is 50 μm (a) Schematics of a batch of nanocapillaries in the salt solution. (b) Schematics of desiccator showing a gas bubble forming near the tip of the capillary marked with black arrows. (c) Schematics of the capillary under microwave radiation. The measured diameter of the nanocapillary displayed here is 47 nm.

Where σ_{gs} is interfacial energy between gas and solution, θ is a wetting angle and r is the radius of a capillary.

Subsequently, a batch of nanocapillaries is placed in a desiccator and kept in 1-10 mbar absolute pressure to degas the solution and further pre-fill nanocapillaries. It enabled to fill the thick end of the capillary with the solution while leaving a pocket of air near the tip (Figure 4.1b) and typically took a few minutes to complete. The formation of this air/water interface typically prevents nanocapillaries from immediate filling and forming electrical contact, required for further measurements. In this study, we ensured the rapid heating of the solution by irradiating the capillaries placed in a solution bath with microwave radiation ($\lambda = 12.2\text{ cm}$) (Figure 4.1c). Heating was performed in cycles by heating up the solution until its boiling point and letting it cool down for 10-20 s. Heating duration varied based on a volume of a solution used to immerse the nanocapillaries and microwave radiation was always applied until the boiling point only to minimize evaporation. By performing the described procedure (3-5 cycles of heating and cooling), we were able to completely fill batches of sub-50 nm nanocapillaries in less than 10 minutes out of which for most of the time (90 %) the solution was not boiling. The length of the procedure varied in order to insure the complete filling of the batch, but as shown in Figure 4.2 it can be reduced to less than 2 minutes, compared to 20 min, while using a thermally driven approach (183). The batch size was limited by the number of pulled and characterized capillaries and typically was 25, but can be significantly increased for high-throughput fabrication pipelines.

To explain the mechanism behind the filling of the nanocapillaries we studied the time evolution of this process (Figure 4.2) with real-time recording using a custom-built imaging setup (See Methods for more details). After partial filling of the fabricated capillaries with a desiccator (Figure 4.2a, Step 1 and also Figure 4.2b marked as 0s) the batch of nanocapillaries is

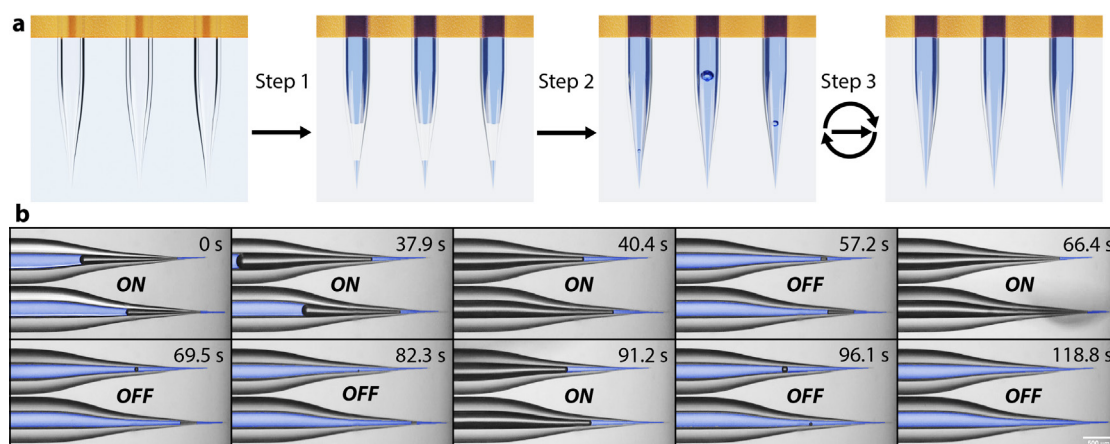


Figure 4.2 – Nanocapillary filling process dynamics. (a) Schematics of the main filling steps: Step 1 - capillaries are prefilled in the desiccator. Step 2 - microwave radiation is applied, thus causing rapid heating of the solution until it boils. This has the effect of reducing the size of the gas bubble. Step 3 - heating is applied in a few cycles, fully filling the nanocapillary in a matter of minutes. (b) Time-lapse snapshots of the filling process while filling 28 nm (top) and 26 nm (bottom) nanocapillaries. The time of each snapshot from the start of the recording is indicated in seconds, the microwave status is indicated as either ON or OFF.

heated with microwave radiation by placing in a microwave oven (Figure 4.2a, Step 2). The microwave radiation induces rapid heating and subsequent boiling of the solution. According to Henry's law, the solubility of gases is reduced with an increase in temperature. The microwave radiation not only causes overheating of the solution(184) but also over-saturation of the liquid with gas which then nucleates into bubbles. Subsequently, gas bubbles grow until they blow up violently, causing additional mixing of the solution inside and outside the capillary and improving transfer of gas outside the capillary. (Figure 4.2b, 0- 40.4s). In the process, the solution is degassed and the gas content in the solution inside the capillary is reduced (Figure 4.2b, 57.2s). After the microwave heating is deactivated, the liquid cools down and starts to absorb the excess gas inside the capillary. Additional cycles (Figure 4.2b, 57.2s - 96.1s) cause the same behaviour. This is observed at the end of the process when only one or more small bubbles are attached to just the sidewalls of the capillary (Figure 4.2b, 96.1-118.8s). As the solution is cooling down its gas capacity is also increasing and that results in air bubbles being absorbed into the now under-gassed solution until there is no visible obstructions (Figure 4.2b, 118.8s). This behaviour was observed in all filled capillaries, so we argue the reason microwave radiation is faster than classical heating methods (with filament(181) or hot plate(183) induced heating) is the high intensity, localized super-heating of the liquid inside the capillary. This causes rapid and efficient over-gassing of the liquid which then transfers the excess gas outside. Microwave radiation is known as a method for enhancing reaction kinetics in both aqueous and non-aqueous solutions(184) and for degassing (185). Corresponding IV curves are shown in Figure 4.5. In addition to this, we have also confirmed the ability to fill the capillaries with glycerol-water and agarose-water solutions by using this method (Figure 4.6). This shows that our method is applicable to a wide range of solutions regardless of high

viscosity.

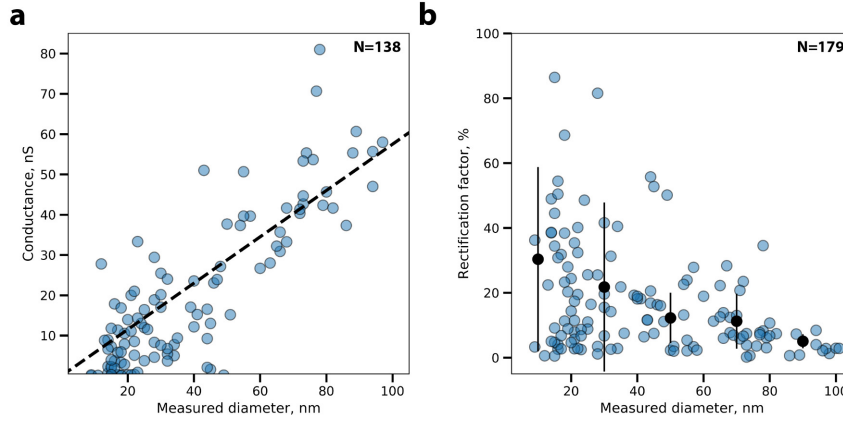


Figure 4.3 – Characterization of filled nanocapillaries after microwave filling protocol. (a) Conductance measured in 400 mM KCl solution vs opening diameter measured with a scanning electron microscope (SEM). The dashed line represents a least-square fit with an equation 2. (b) Rectification factor vs size measured with SEM.

In order to test the efficiency of the filling method of microwave radiation induced filling, multiple nanocapillaries were analyzed by measuring the size of the nanocapillaries with a scanning electron microscope (SEM), taking brightfield microscopy images before and after the microwave radiation induced filling and measuring the electrical characteristics such as IV curves and noise levels (Figure 4.10, Figure 4.11) to quantify the electrical parameters after the filling procedure (Figure 2). Nanocapillaries of different sizes, visually examined after the typical filling procedure showed 100 % filling success rate. Similar results were previously reported with a thermally driven approach(183). In this study, all the fabricated capillaries (N=179) were further electrically characterized, by recording IV curves and 14.1 % of the nanocapillaries displayed electrical characteristics of the nanocapillaries that were either mechanically damaged (broken with much larger current reading) or clogged (no electrical contact). This number could be elevated due to capillary braking and contamination not related to filling procedure, however, we used it to estimate the filling success rate. The dependency of conductance on the diameter of the nanocapillaries as measured by SEM (Figure 4.3) was fitted with a conductance model adapted from a previously published study (186) (Eq. 2):

$$G = \sigma \left(\left(\frac{4t}{\pi Dd} + \frac{1}{2D} + \frac{1}{2d} \right) \right)^{-1}$$

D is the shaft diameter (here 400 μm), d the diameter of the nanopore, t the taper length which was determined to be around 2 mm in our experiments. The indicated fit follows a linear trend for the capillary size range of 10-100 nm. The intrinsic variation for the small diameter (< 20 nm) nanocapillaires can be caused by multiple factors such as quality of

SEM measurement of the diameter of the opening due to charging effects or lack of precise estimate of three-dimensional geometry of the nanocapillary. Furthermore, an increase in the rectification factor with a decrease in nanocapillary diameter was observed (Figure 4.3b) in the nanocapillaries. This is in agreement with previous reports where smaller nanocapillaries are known to have a larger ionic current rectification factor(187)

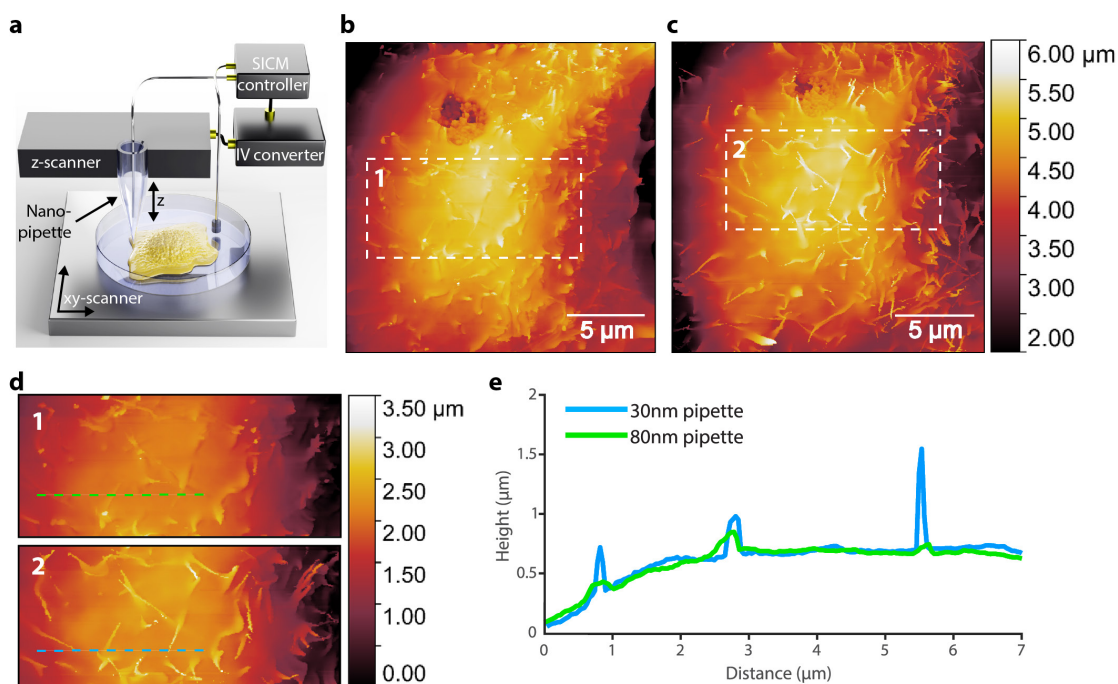


Figure 4.4 – Scanning ion conductance microscopy images of the same area of a fixed cell scanned with a 30 and 80 nm sized nanocapillary filled with the protocol described in this paper. (a) Schematics of a SICM setup used for imaging. (b-c) Topographical image of a fixed COS-7 cell scanned with 80 nm (b) and 30 nm (c) nanocapillary. (d) Corresponding zoom-ins of the areas marked in (b) top and in (c) bottom. (e) Line-profiles from panel (d) indicated in green and blue.

Finally, microwave filled nanocapillaries were used for scanning ion conductance microscopy imaging (Figure 4.4). The SICM was chosen as a proof of principle platform for filled nanocapillaries. Imaging was performed with a home built SICM (Figure 4.4a). Briefly: the SICM was mounted over an inverted optical microscope (Olympus IX 73). The sample was scanned in X,Y by a piezo-stage and the capillary was moved in Z by a home built Z-actuator. Characterized 30 nm and 80 nm capillaries filled with 400 mM KCl solution (pH=7.5) were used for imaging the membrane surface of fixed COS-7 cells. In particular, microvilli were imaged as a structure of interest to perform a comparison of SICM resolution by using different diameter nanocapillaries. Previously reported dimensions of this membrane structure are approx. 1000 nm in length and 100 nm in diameter (188). This corresponds well with the values measured with the 30 nm pipette. The theoretical lateral resolution of SICM is approximately three times the inner opening radius of the nanocapillary $d_0 = 3d$ (117). In Figure 4.4b the microvilli can

not be distinguished clearly while imaged with a 80 nm nanocapillary ($d_0 \approx 120\text{nm}$). However, a 30 nm ($d_0 \approx 45\text{ nm}$) nanocapillary allowed us to visualize the topography of microvilli with the expected topographical dimensions as stated previously.

Conclusion

We have demonstrated an efficient and fast method to fill sub-100 nm quartz nanocapillaries by using microwave radiation induced heating. We have experimentally evaluated the throughput of the method visually and by performing electrical measurements with a fabricated and filled nanocapillaries. To demonstrate the practical application of the fabricated nanocapillaries we have performed a SICM imaging experiment and qualitatively demonstrated the impact of capillary size for the imaging resolution. We believe that the nanocapillary filling method proposed in this paper can be useful for the nanofluidic devices requiring a large number of filled nanocapillaries with various aqueous solutions.

Experimental Section

4.1.1 Nanocapillary fabrication and characterization

Nanocapillaries used in our experiments were fabricated using a CO₂-laser puller (P-2000, Sutter Instrument). Quartz capillaries with 0.5 mm outer diameter and 0.2 mm inner diameter were bought from (Hilgenberg GmbH). Before the pulling process, all capillaries were cleaned with 100 % acetone, 100 % ethanol, miliQ water (Millipore Corp) and again with 100 % ethanol by sonicating in each solution for at least 10min. After washing, nanocapillaries were dried in a desiccator for 1-2 h until they were completely dry. The pulling program used to fabricate nanocapillaries is shown in Supporting Information Table S1. After the fabrication, nanocapillaries were characterized by scanning electron microscope (Zeiss, Merlin). All nanocapillaries were fabricated using a laser pipette puller with a protocol optimized for the fabrication of nanocapillaries with 30-50 nm diameter range. Nanocapillary diameters were confirmed using SEM, and as expected, under relatively high imaging current (400 pA), capillaries under 40 nm shrunk (119) due to electron beam heating induced effects. However, the shrinking process didn't alter significantly nanopipette geometry as the size difference before and after shrinking hasn't exceeded half of the capillary diameter. Diameters of all nanocapillaries were measured manually based on SEM images, using Fiji software (138) as it is shown in Figure 4.11.

4.1.2 Solution

KCl solutions used in this study were prepared from miliQ water (18.2 MΩ cm at 25 °C, Millipore Corp.). 400 mM KCl solutions were buffered with 40 mM TRIS, by adjusting the pH to 7.5 with HCl using a pH meter. All solutions were filtered with 20 nm filters (Whatman Anotop 25 Plus) before use.

4.1.3 Filling of Nanocapillaries

After SEM imaging, nanocapillaries were placed on the cover-glass with double-sided polyimide (Kapton) tape. Nanocapillaries were then cleaned with oxygen plasma (Femto A, Diener electronic GmbH) for 660 s at maximum power setting. Immediately after, the nanocapillaries were immersed in a 400 mM KCl solution and placed inside the desiccator connected to the vacuum pump. Nanocapillaries were kept under low pressure conditions (1-10 mbar) for 10 minutes in order to pre-fill them. Then they were imaged with an inverted brightfield microscope (Figure 4.8). After pre-filling step, the nanocapillaries were placed inside the microwave oven (MW 1766 EASY WAVE, P = 700 W, λ = 12.23 cm). The highest power setting was always used. Microwave radiation was applied in heating cycles in order to heat the solution until its boiling point. Heating duration varied based on the volume and temperature of a solution. First heating phase took (30-60 s), subsequent heating phases were significantly shorter (5-10 s) due to increased temperature of the capillary immersion solution. Heating was always applied until the boiling point of a solution in order to minimize the evaporation. Short 10-20 s pauses were made between heating steps (Supporting Video 1) to allow for the gas to dissolve into the solution. At least 3 heating cycles were performed to complete filling of the batch. Nanocapillaries then were imaged with a brightfield microscope. After the procedure, the buffer was exchanged to ensure salt concentration was not affected by evaporation. For storage, nanocapillaries were kept at 4 °C.

4.1.4 Brightfield microscopy imaging

Nanocapillaries were imaged with a brightfield microscope, equipped with (2.5x) objective (Zeiss EC Plan, NA=0.06) and sCMOS camera (Hamamatsu OrcaFlash 4). Nanocapillaries were imaged in a 400 mM KCl solution prepared as described previously. Basic image analysis and processing was performed in Python and Fiji(138).

4.1.5 Recording of nanocapillary filling dynamics

The nanocapillary filling process was recorded with a long-focal distance USB microscope (Dino-light, AM3113T) mounted outside the microwave oven (WD700J17-2, P = 700 W, λ = 12.23 cm) using a white-light LED illumination source. The schematics of imaging chamber used is displayed in Figure 4.7. Since all the microwave heating experiments were performed at the regular ambient pressure, the boiling point was determined visually, by observing the solution and can be clearly seen in a Supporting Video 1.

4.1.6 Recording of IV curves

Current-voltage (IV) curves were measured with Ag/AgCl electrodes in a dedicated Teflon pipette holder filled with 400 mM KCl, placed in a Faraday cage to reduce noise from external sources (Figure 4.9). The current generated was amplified with a Femto DLPCA-200 (100M Ω

Chapter 4. High-Throughput Nanocapillary Filling Enabled by Microwave Radiation for Scanning Ion Conductance Microscopy Imaging

gain) at 7 kHz. The data was recorded with a dedicated LabVIEW (National Instruments) visual interface by sweeping the bias voltage from -500mV to 500mV in 10mV gradual steps, thus spending the same time in each interval. IV current traces were analyzed and plotted with a custom-written Python script.

4.1.7 Preparation of a fixed COS-7 cell sample

#1.5 cover glass coverslips were cleaned with a piranha solution and coated with fibronectin from bovine plasma (0.5 μ M/ml). African green monkey kidney fibroblast-like cells (COS-7), purchased from ATCC were grown in DMEM without phenol red medium, containing 10 % of fetal bovine serum. Then cells were fixed with 4% PFA with 0.02% Triton X-100 in 1xPBS (pH=7.4) for 15 min and washed thrice for 5 min each with PBS (pH=7.4). Imaging was performed in 400 mM KCl (pH=7.5) solution. All chemicals were purchased from Sigma Aldrich, unless stated differently.

4.1.8 Scanning ion conductance microscopy

The scanning was performed with a custom made SICM setup. The sample was actuated in X and Y by a piezo-stage (Piezosystemjena TRITOR102SG). The capillary is moved in Z by a home built actuator, operated in hopping mode. The hopping height was 1 μ m at a 100 Hz rate. The current set-point used in the hopping actuation was 99 % of the current recorded. Images with 512x512 pixels were generated with a pixel size of 39 nm.

4.1.9 Acknowledgement

S.M. S.J.D. and A.R. acknowledge financial support from the Swiss National Science Foundation (SNSF) Consolidator grant (BIONICBSCGI 0157802). V.N. acknowledges the support of the Max Planck-EPFL Center for Molecular Nanoscience and Technology. G.E.F. acknowledges support from ERC-COG (InCell-773091).

4.1.10 Supporting Information

HEAT=570	FILAMENT=4	VELOCITY=10	DELAY=170	PULL=0
HEAT=570	FILAMENT=4	VELOCITY=10	DELAY=170	PULL=200

Table 4.1 – Pulling parameters used to pull quartz nanocapillaries with Sutter P-2000 instrument with a 2 step program. 0.7mm OD and 0.4mm ID quartz pipettes were used. Average pulling time was 0.96 s

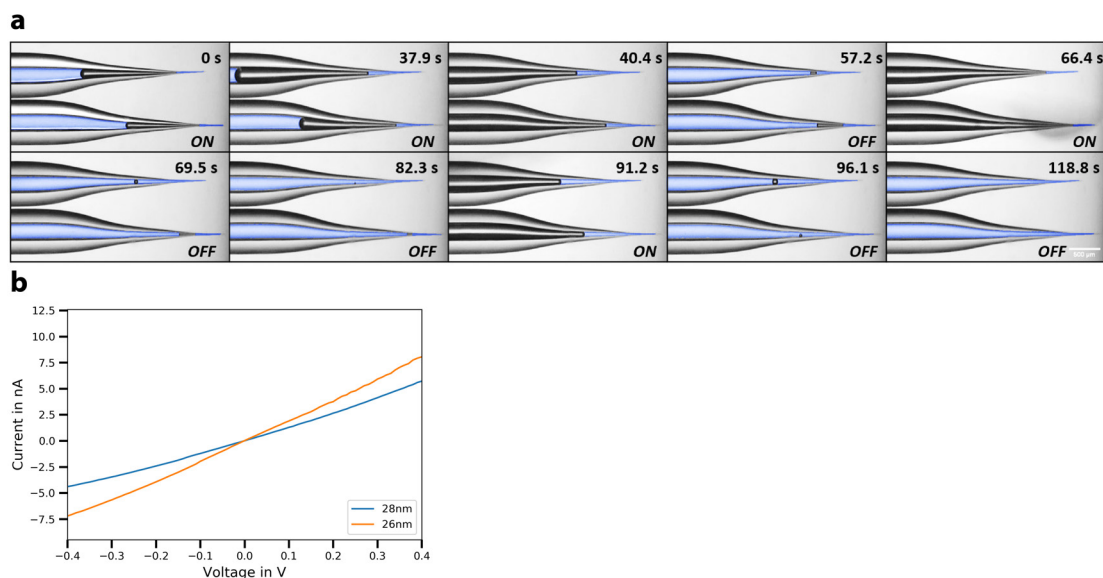


Figure 4.5 – a) A time sequence from Figure 4.2 in the main text. A full video can be found [here](#) and is attached to the paper as SI Video 1 b) IV curves of filmed nanocapillaries. 1.13% and 16.4% rectification factor was measured for 28 nm and 26 nm nanocapillaries respectively with a corresponding RMS noise values of 5.3 pA and 5.9 pA.

Chapter 4. High-Throughput Nanocapillary Filling Enabled by Microwave Radiation for Scanning Ion Conductance Microscopy Imaging

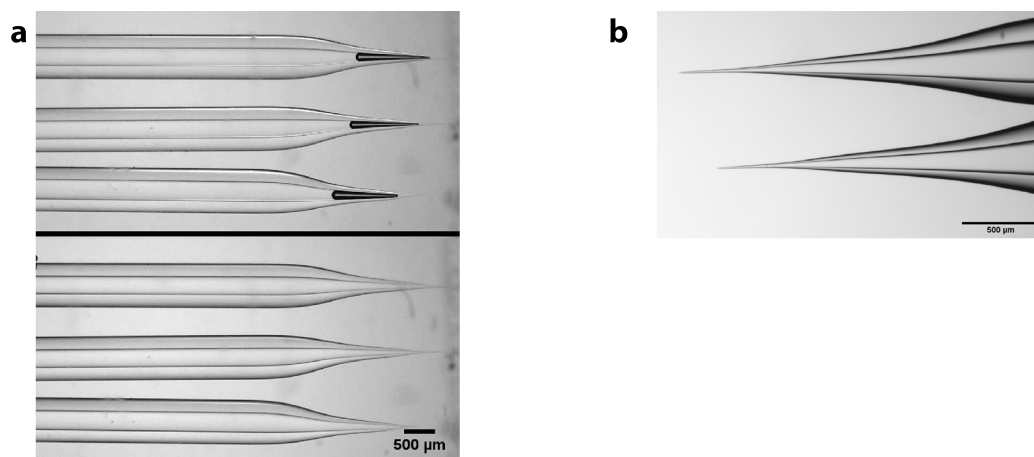


Figure 4.6 – (a) Brightfield microscopy image of sub-30 nm capillaries before and after filling with 50% glycerol 400mM KCl solution. A full filling video can be found here and is attached to the paper as SI Video 2 (b) Brightfield microscopy image of sub-30 nm pipettes filled with 1 % agarose, MiliQ water solution.

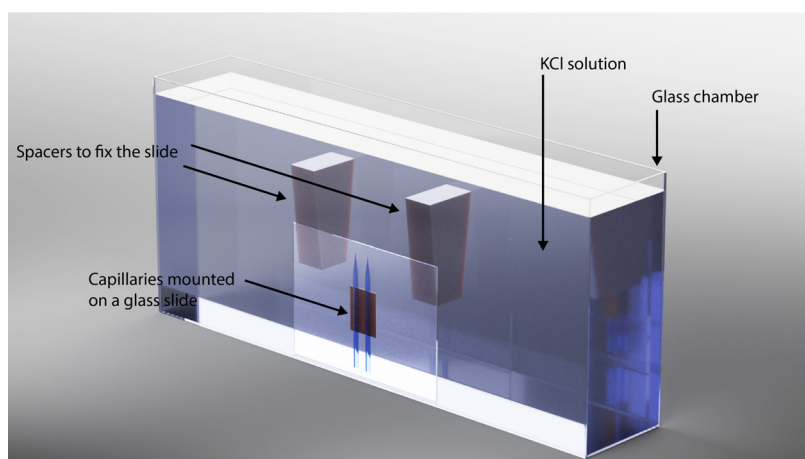


Figure 4.7 – Schematics of a chamber used for direct imaging of nanocapillary filling process. The nanocapillaries were mounted on the glass slide with double-sided Kapton tape and for the filming purpose only, the glass slide was placed vertically in the chamber filled with KCl solution. Slide was fixed with teflon spacers. Chamber then was placed in a microwave oven and filmed through the conductive mesh.

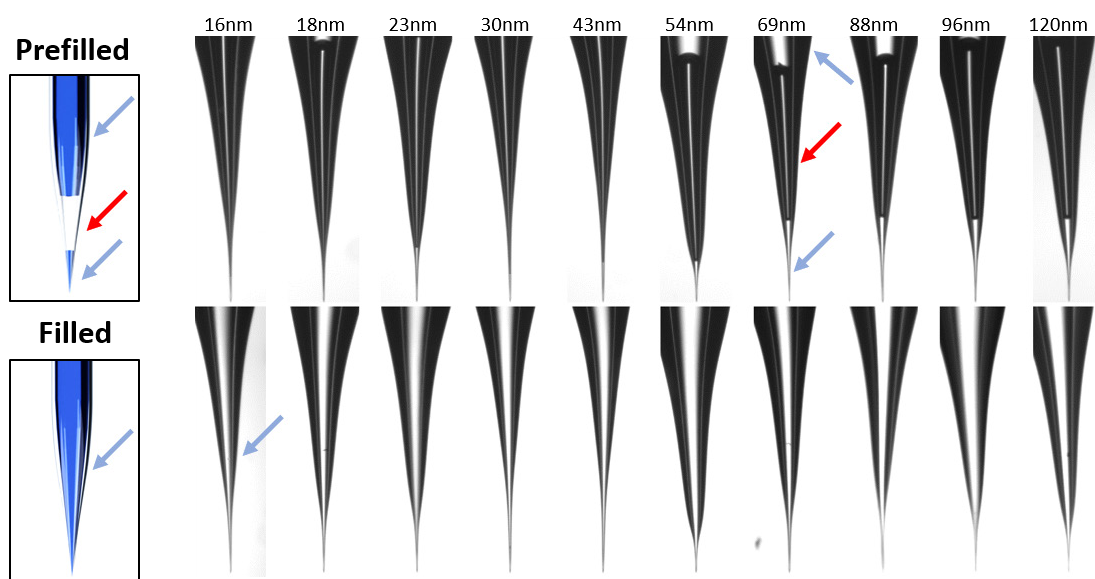


Figure 4.8 – (a) Schematics of prefilled (top) and completely filled (bottom) nanocapillary. (b) Brightfield microscopy images of sub-30 nm capillaries before and after filling with 400mM KCl solution. SEM measured sizes of nanocapillaries are indicated above each row. For better image understanding, blue arrows are showing solution, red arrows - gas bubble.

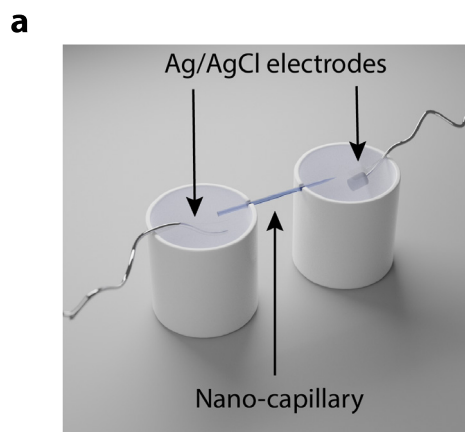


Figure 4.9 – (a) Schematics of current recording setup used for current signal recordings. Capillaries were placed on 2 teflon wells to ensure good insulation between the tip and the thick end. The recordings were performed in a Faraday cage with a setup described in main methods section.

Chapter 4. High-Throughput Nanocapillary Filling Enabled by Microwave Radiation for Scanning Ion Conductance Microscopy Imaging

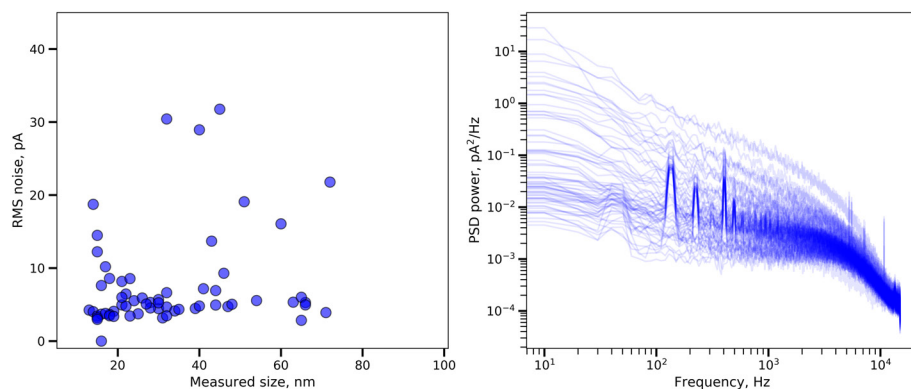


Figure 4.10 – (a) RMS current noise of 72 capillaries together with power-spectral density plots. Signals were measured with Femto amplifier DLPCA-200 (100 *M*Omega gain) with a 7 kHz bandwidth and sampled at 30 kHz. RMS noise seems to be similar within the measured capillary size range. We have also plotted power-spectral density calculated with Welch method.

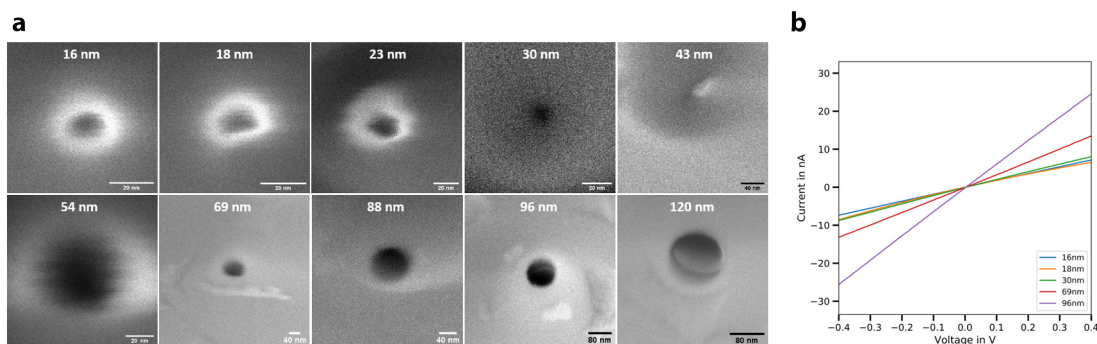


Figure 4.11 – (a) SEM images of the pipettes displayed in the Supporting Figure S4. (b) IV curves of 16nm, 18nm, 30nm, 69nm, 96nm pipettes filled with 400mM KCl.

5 Scanning ion-conductance spectroscopy

The following chapter will be the basis for the publication which is currently under preparation with a tentative title:

Vytautas Navikas¹, Samuel M. Leitao², Sanjin Marion¹, Georg E. Fantner², Aleksandra Radenovic¹. **Scanning ion-conductance spectroscopy**, manuscript under preparation.

V.N. and S.L. equally contributed to the paper by refining the general idea and writing the final manuscript with input from all the authors. V.N. prepared the single-molecule samples, fabricated nanocapillaries, performed optical imaging experiments and data analysis. S.L. built a modified SICM setup and performed the SICS measurements. S.M. contributed by performing simulations and strategizing the data analysis and experimental design. A.R. conceived the general idea. A.R and G.E.F supervised the work.

¹Laboratory of Nanoscale Biology, Institute of Bioengineering, School of Engineering, Swiss Federal Institute of Technology Lausanne (EPFL), Lausanne, Switzerland.

²Laboratory for Bio- and Nano-Instrumentation, Institute of Bioengineering, School of Engineering, Swiss Federal Institute of Technology Lausanne (EPFL), Lausanne, Switzerland.

5.1 Introduction

The main aim of this section of the thesis is to demonstrate the ability to use SICM as a high-throughput and high-sensitivity single-molecule detection platform to extend the use of SICM to detect topological variations in DNA molecules. On top of that, we have performed combined single-molecule fluorescence imaging to explore a correlative aspect and to provide

additional experimental controls. The general principle of SICM was already introduced in Chapter 2. In this chapter, the general principle of ionic-current based topographical imaging is exchanged for the ionic-current based single-molecule topology detection by performing controlled translocations of DNA molecules with a SICM probe.

5.1.1 Biological nanopores

In nature, there is a huge variety of membrane proteins that form pores to allow transport through the otherwise impermeable phospholipid bilayer(189). The most common biological nanopores used in nanopore sensing are bacterial pores such as *Mycobacterium smegmatis* porin MspA, α -hemolysin, or aerolysin among many others. These bacterial porins are robust and widely accessible, thus popular in the biological nanopore field. The first experiments demonstrating the ability to sense the translocation events of DNA by measuring the ionic-current through reconstituted α -hemolysin pore were demonstrated in mid 1990s(190) driving the field towards the ultimate goal of DNA sequencing. The first such demonstration used a mutant MspA porin with phi29 DNA polymerase to control the speed of DNA translocation through the pore and enabling the sequencing-based on ionic-current changes as single-stranded DNA is passing through the pore's constriction(191). Commercial devices created by the Oxford Nanopore company are based on this nanopore sequencing approach and are already available for DNA and RNA sequencing. However, the challenges of the stability and robustness of the devices that are using biological nanopores remain and a variety of alternative nanopore platforms are being explored and developed.

5.1.2 Solid-state nanopores

On the other hand, the synthetic bottom-up approach for nanopore fabrication was developed based on solid-state nanopore technology. Multiple dielectric materials such as silicon nitride (SiN_x)(192; 193), silicon dioxide (SiO_2)(194), aluminium oxide Al_2O_3 (195) and most recently two-dimensional materials such as graphene(196), molybdenum disulfate (MoS_2)(197) or hexagonal boron nitrate ($h\text{BN}$)(198) have been used for solid-state nanopore fabrication and DNA translocations. Compared to biological counterparts, solid-state nanopores can be used for a variety of applications outside molecular sensing such as water filtration, blue energy production(199), thanks to their chemical stability and 2D crystal structure. In the field of bio-sensing, the solid-state nanopores were used to study DNA, polypeptide sequences, proteins, DNA-protein complexes, etc. However, the fast speeds of free translocations are limiting the temporal and spatial resolution due to a finite amplifier bandwidth limiting SNR, thus making the DNA sequencing out of reach. The translocation speed problem was solved in biological nanopores by using genetically engineered nanopore with attached molecular motors(200). However, controlling the translocation speed at the precisely defined nanopore constriction and doing this at a single molecule level using solid-state devices, remains difficult.

Most of the solid-state nanopores such as pores made from 2D materials are fabricated by

using state-of-art expensive cleanroom methods such as focus ion beam (FIB) lithography and focused electron beam (FEB) lithography(201) inside high-end electron microscopes, thus making the fabrication process expensive and low throughput. In contrast, the considerably simpler alternative of glass capillaries allows to produce the nanopore probes at a considerably lower price and without a need for a cleanroom, fabrication (175). Originally introduced for patch clamping applications(202) they were demonstrated to be a robust platform for detecting translocations of various analytes(203; 204). Glass nanocapillaries can be manufactured to the diameters ranging below 4 nm by precisely controlling the diameter of the opening with electron beam irradiation(194) or by depositing the additional coatings by controllable wet-chemical silanization(205) compared to 1-2 nm diameter nanopores demonstrated using 2D materials (201). Furthermore, glass nanopores demonstrate good SNR characteristics for high bandwidth measurements, thanks to a low-capacitance of glass inhibiting high-frequency noise (203).

However, the biological pores are the most capable platform for ionic-current based detection due to their nature-given geometry and the possibility to couple biological motors to precisely control translocation speed. The ability to fabricate small solid-state nanopores, with geometry similar to biological pores is just a part of the story. The following chapter will discuss the attempts to engineer and develop solutions that mimic the biological pore in terms of speed control in order to regulate the speed at which the analyte is passing through the pore.

5.1.3 Controlled DNA translocations

Multiple approaches to reduce translocation speeds were explored. The fundamental goal is to reach the (geometry dependant) translocation speed of $\sim 100 \text{ ntms}^{-1}$ (97), which would allow registering the distinct current levels of different nucleotides using commercially available current amplifiers. Most of the controlled translocation attempts employed a nanopositioning system to controllably position DNA through immobile nanopore. The tip of the atomic force microscope tip(206), optical tweezers (OT) (207), magnetic tweezers(208), tuning fork(209) were used. Methods as OT or AFM can produce the additional force signal which is more sensitive in detecting the forces while translocating negatively charged DNA(207) and DNA-protein complexes(176) and it can be used to correlate the force signal with current traces. Overall, due to the complexity of experimental techniques mentioned, only a limited experimental throughput was so far demonstrated, thus limiting the impact of previous approaches.

5.1.4 Glass nanopores for controlled DNA translocations

In this work, we employ specially manufactured SiO_2 nanopores with openings below 50 nm previously used for controlled DNA translocations with optical tweezers (186; 176). Compared to AFM approaches using hollow cantilevers(210), glass nanopores are an order of magnitude less expensive and simple to manufacture as well as providing excellent SNR characteristics for high bandwidth measurements (119). However, in contrast to the optical tweezers based scan-

ning approach, we use surface-immobilized biotinylated DNA as a semi-stationary analyte and perform the controlled translocation with a nanocapillary itself by using a modified SICM setup. This allows us to scan the same molecule multiple times, thus enabling us to improve the signal-to-noise ratio (SNR) or observe molecular dynamics. Controlling the position of the pipette with a piezo actuator allows us to simplify the DNA pulling procedure. On top of that, we can position the pipette in 3 dimensions, which allows us to scan the surface in a manner similar to SICM hopping mode (72). We name our modified SICM approach scanning ion-conductance spectroscopy (**SICS**) for single-molecule topological imaging and this abbreviation is going to be used further in the thesis. To demonstrate the versatility of our technique we performed SICS imaging on multiple DNA constructs and DNA-protein complexes. We further chapter summarizes the methods used for sample preparation, setup design and data analysis.

5.2 Methods and Experimental setups

5.2.1 Fabrication and characterization of nanocapillaries

Nanocapillary fabrication was similar to the procedure described in Chapter 3. Nanocapillaries used in all experiments were fabricated using a CO₂-laser puller (P-2000, Sutter Instrument) by using commercially available quartz capillaries with 0.5 mm outer diameter and 0.2 mm inner diameter were bought from (Hilgenberg GmbH). Before the pulling process, all capillaries were cleaned with 100 % acetone, 100 % ethanol, miliQ water (Millipore Corp) and again with 100 % ethanol by sonicating in each solution for at least 10min. After washing, nanocapillaries were dried in a desiccator for 1-2 h until they were completely dry and cleaned for 10 minutes in oxygen plasma. After the fabrication, nanocapillaries were characterized by a scanning electron microscope (Zeiss, Merlin). Nanocapillary diameters were confirmed using SEM, and as expected, under relatively high imaging current (400 pA), capillaries under 40 nm shrunk (119) due to electron beam heating induced effects. However, the shrinking process didn't alter significantly nanopipette geometry as the size difference before and after shrinking hasn't exceeded half of the capillary diameter. Diameters of all nanocapillaries were measured manually based on SEM images, using Fiji software (138).

5.2.2 Nanocapillary filling procedure

The Nanocapillary filling method was similar to the procedure described in Chapter X. After SEM imaging, nanocapillaries were placed on the cover-glass with double-sided polyimide (Kapton) tape or a specially designed holder fabricated from PEEK plastic. Nanocapillaries were then cleaned with oxygen plasma (Femto A, Diener electronic GmbH) for 300 s at maximum power setting. Immediately after, the nanocapillaries were immersed in a 400 mM or 1000 mM KCl solution and placed inside the desiccator connected to the vacuum pump. Nanocapillaries were kept under low-pressure conditions (1-10 mbar) for 10 minutes to pre-fill

them and avoid the formation of air bubbles in the thick end of the capillaries. Then they were imaged with an inverted brightfield microscope to confirm pre-filling. After, the nanocapillaries were placed inside the microwave oven (MW 1766 EASY WAVE, $P = 700\text{ W}$, $\lambda = 12.23\text{ cm}$). The highest power setting was always used. Microwave radiation was applied in heating cycles to heat the solution until its boiling point. Heating duration varied based on the volume and temperature of a solution. The first heating phase took (30-60 s), subsequent heating phases were significantly shorter (5-10 s) due to the increased temperature of the capillary immersion solution. Heating was always applied until the boiling point of a solution in order to minimize the evaporation. Short 10-20 s pauses were made between heating steps to allow for the gas to dissolve into the solution. At least 3 heating cycles were performed to complete the filling of the batch. After the procedure, capillaries were kept at $4\text{ }^{\circ}\text{C}$ and the buffer was exchanged after few hours to ensure salt concentration was not affected by evaporation. For storage, nanocapillaries were kept at $4\text{ }^{\circ}\text{C}$ in sealed chambers for up to 1 year.

5.2.3 Ultra-clean chambers for DNA immobilization

The imaging chambers that are compatible with single-molecule fluorescence and single-molecule scanning-ion conductance microscopy imaging were fabricated from high precision No. 1.5 borosilicate 25 mm coverslips (Marienfeld). Coverslips were cleaned with ethanol, washed in MiliQ water, dried with N_2 flow and cleaned with oxygen plasma (Femto A, Diener electronic GmbH) at maximum power for 660s. After cleaning the open circular chamber made from 1 mL pipette tip was glued on top with polydimethylsiloxane (PDMS), forming the final assembly (Figure 5.1). Fabricated chambers were kept in sealed petri-dishes until further use.

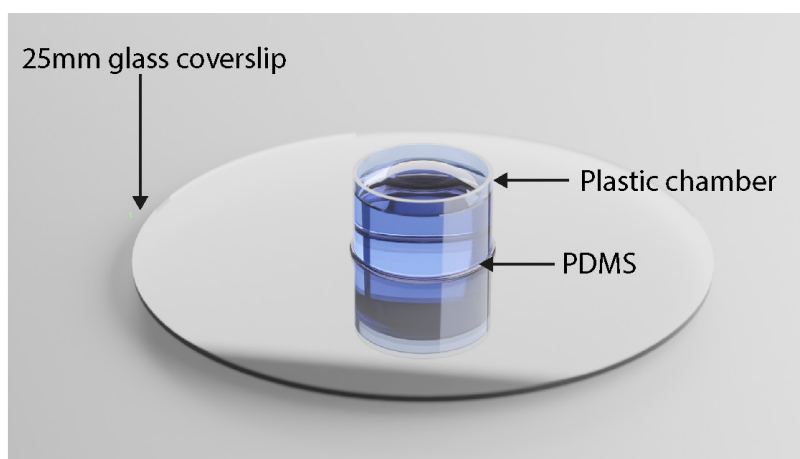


Figure 5.1 – Schematics of an imaging chamber used in this study.

5.2.4 Lambda DNA preparation

10 kilobase long λ -DNA was prepared from full-length phage λ -DNA (New England BioLabs) by performing polymerase chain reaction (PCR) using one primer (Microsynth) with a biotin tag on a 5' end and the second one without biotin at the 3'. PCR was performed using a LongAmp DNA polymerase (New England BioLabs) following the protocol from the manufacturer. The reaction mixture was purified using PCR and Gel Cleanup kit (Qiagen) from the agarose gel according to the protocol from the manufacturer. The length of 10kb λ -DNA product was verified with an agarose gel electrophoresis, and the concentration was measured with a NanoDrop 1000 spectrometer.

5.2.5 DNA ruler constructs

DNA ruler constructs were prepared in the group of Prof. Ulrich F. Keyser, using a well established protocol(211). The DNA ruler was synthesised by cutting circular 7249 base m13mp18 ssDNA (New England Biolabs) using the enzymes EcoRI and BamHI to form a linear ssDNA chain 7228 bases in length. the final scaffold is then purified and mixed in a 1:5 ratio with 212 oligonucleotides which form a double-strand with six equidistant zones of dumbbell hairpins. The mixture is then annealed and purified. The final construct contains 6 markers with 8 dumbbells each. Markers are equally positioned in intervals of 1032 bp (Figure 5.2).

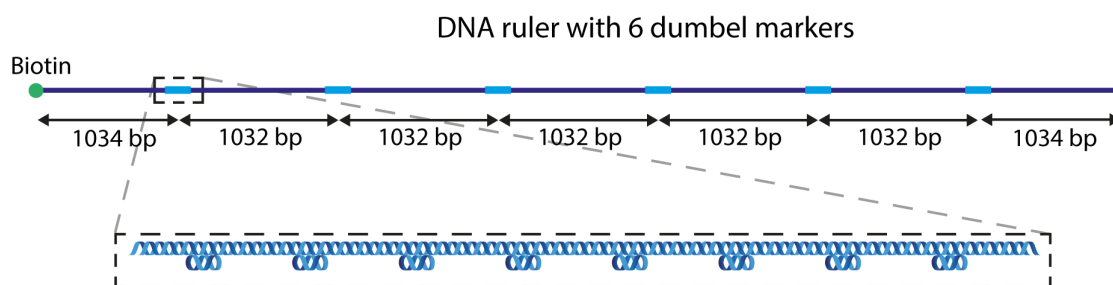


Figure 5.2 – Schematics of a molecular DNA ruler design with 6 markers each containing 8 dumbbell segments. Total length of a construct is 7228 bp.

5.2.6 gRNA preparation and immobilization

10kb long λ -DNA was screened for the presence of PAM motifs (5'X'20NGG3') and two targets separated by 5374 bp were selected. For DNA ruler DNA - one target was selected between the 2nd and 3rd marker (2464 bp from 3' end of a DNA). Single guide RNAs (sgRNAs) were designed bearing complementarity to the 20 bp 5' adjacent PAM motif sites that were selected on a DNA. sgRNAs were prepared by *in vitro* transcription of dsDNA templates carrying a T7 promoter sequence. Transcription templates were generated by PCR amplification of ssDNA templates containing the T7 binding site, 20 bp sequence complementary to the DNA target site and sgRNA scaffold sequence using Phusion High-Fidelity DNA Polymerase (New England Biolabs). The sgRNAs were synthesized by *in vitro* transcription using

the MEGAshortscript T7 Transcription kit (Thermo Fisher) according to the manufacturer's conditions. The sgRNAs were treated with Turbo DNase (Thermo Fisher) and MEGAclean Transcription Clean-Up Kit (Thermo Fisher) was used for purification according to the protocol provided by the manufacturer. The concentration of purified sgRNAs was measured with a NanoDrop 1000 spectrometer and the length and quality of the sgRNA were estimated by agarose gel electrophoresis. sgRNA samples were kept in a freezer for the maximum time of 48h until further use.

5.2.7 dCas-9-DNA complex formation

A commercially available inactive mutant of Cas-9 nuclease (dCas-9) with N-terminal SNAP-tag (EnGen Spy dCas9) was acquired from New England Biolabs. The protein was labelled with SNAP-Surface Alexa Fluor 647 labelling kit (New England Biolabs) according to the protocol provided by the manufacturer. The unreacted substrate was removed by the size exclusion column. Finally, fluorescently labelled dCas-9 was incubated with sgRNA in 1X NEBuffer 3.1 (New England Biolabs). 1nM dCas-9 was incubated with 10nM sgRNA (unless stated differently) for 30min at 37°C on orbital shaker. 0.5 units of RNase inhibitors (Thermo Fisher) was used to prevent the degradation of RNA. After incubation, DNA was added at the final concentration of 50pM and the mixture was further kept for 30 min at 37°C on an orbital shaker. Schematics of the final constructs are shown in Figure 5.3.

5.2.8 Surface immobilization

100µL of 1 mg/ml of BSA-Bt (Sigma-Aldrich) in PBS was incubated for at least 1h in plasma cleaned chambers to achieve the full glass surface coverage. Samples then were washed 10x with PBS by exchanging half of the solution, but without drying a surface. Samples then were incubated with 0.1 mg/ml of streptavidin (Sigma-Aldrich) for 1h, followed by 10x wash with PBS. Finally, 10-100 pM of DNA/DNA rulers/DNA-dCas-9 complexes were incubated for 1h, followed by 10x wash with PBS or 3.1 NEBuffer. Samples were kept at 4°C until use. DNA-dCas-9 samples were imaged immediately. A solution in imaging chambers was exchanged by performing an additional 10x wash before imaging. The final imaging solutions are described in the imaging or SICS sections.

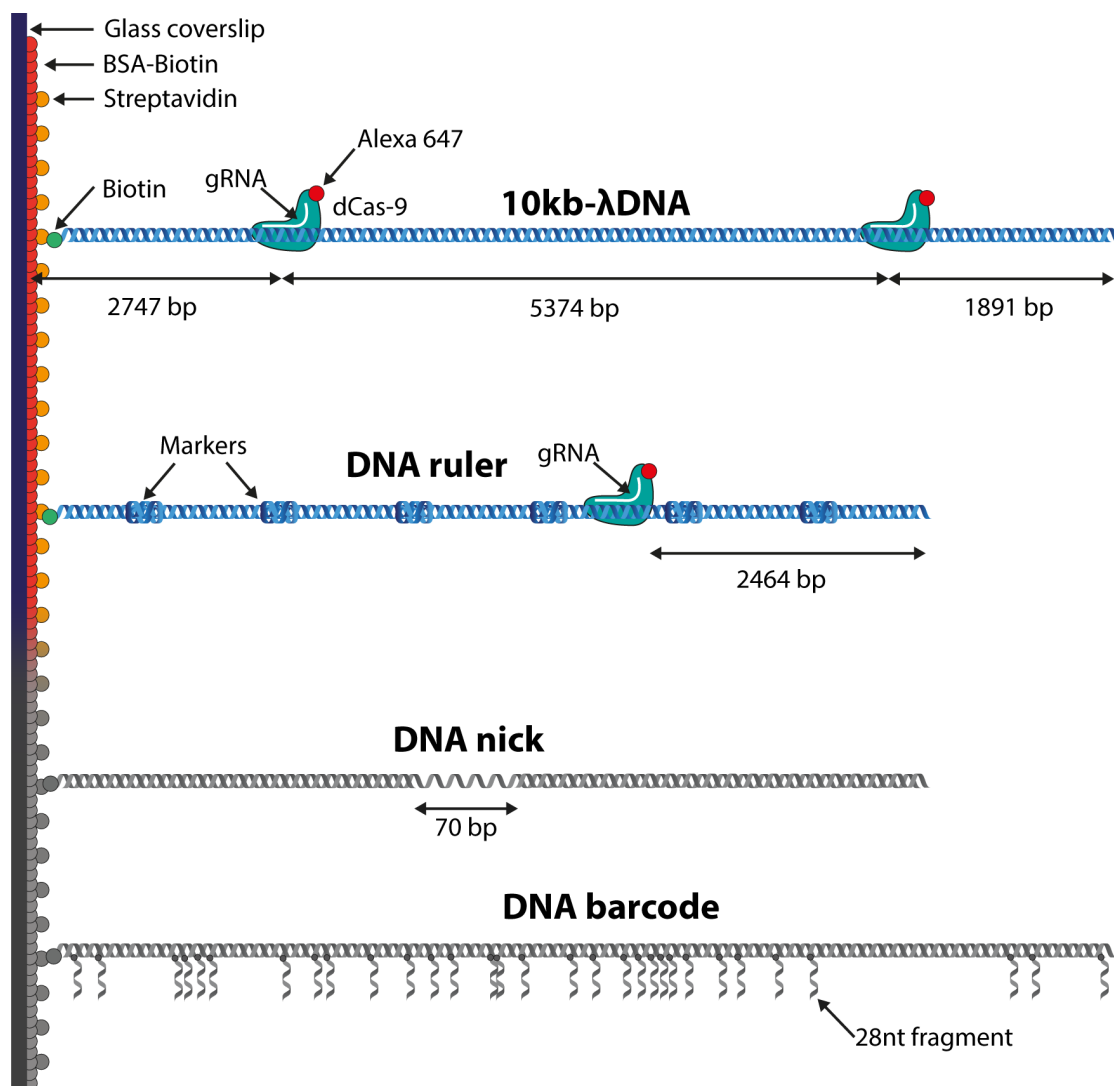


Figure 5.3 – Schematics of dCas-9-DNA complexes and DNA constructs immobilized on a glass surface. 10 kilobase long λ -DNA (top) and DNA-ruler construct was used for dCas-9 immobilization. Locations of dCas-9 proteins are indicated in base pairs (bp). The constructs of DNA nicks and DNA barcodes showed in grey are under development and SICS results from these samples are not showed in the thesis. All objects are not to scale.

5.2.9 Single-molecule fluorescence imaging

To optimize the surface density of DNA and to perform a control of dCas-9 binding, samples were first imaged with a fluorescent microscope described in Chapter 2. For single-molecule imaging and prevent photobleaching reductive/oxidative system (ROXS) based on glucose oxidase and catalyse was used. Final buffer composition consisted of 2mM TROLOX, 40mM TRIS, 400mM KCl, 1% of glucose, 120 units/ml of glucose catalyse, 15 units/ml. Buffer was filtered with a 200 nm filter. Imaging was performed in a sealed chamber to avoid oxygen

exposure. All chemicals were acquired from (Sigma-Aldrich) unless stated otherwise.

5.2.10 SICS setup and electrical measurements

A current signal was measured with Ag/AgCl electrodes in a dedicated PEEK pipette holder filled with 400 mM or 1M KCl, placed in a Faraday cage to reduce noise from external sources. The current generated was amplified with a Femto DLPCA-200 (100M Ω gain) at 7 kHz. The data was recorded with a dedicated LabVIEW (National Instruments) visual interface by performing approach/retract movement by a piezo-stage (Piezosystemjena TRITOR102SG).

5.2.11 Data analysis

Image data analysis was performed using Fiji(138) software. Current trace analysis was done with a custom-written Python program which was used to automatically filter data, align different molecules and calculate various signal parameters.

5.3 Results and Discussion

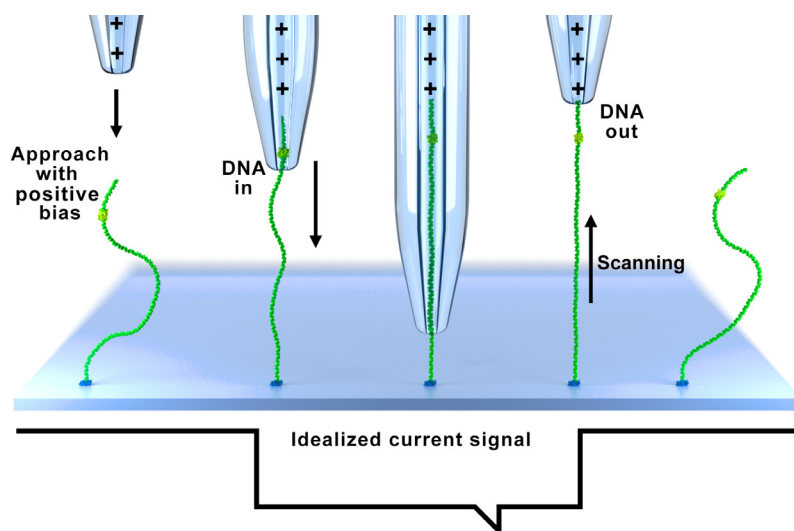


Figure 5.4 – Schematic of the main principle of scanning ion-conductance spectroscopy. The nanocapillary with a positive bias applied between the electrode in the nanocapillary and an electrode in a solution is lowered to the surface where the negatively charged DNA is translocated through the opening what is registered as a drop of the ionic current. When the nanocapillary is moved up, the analytes such as proteins attached to the DNA strand can be detected as well. Finally, the DNA leaves the nanocapillary what is registered as an increase of the ionic current and the process can be repeated, thus scanning the same molecule multiple times.

The study of scanning ion-conductance spectroscopy (SICS) was performed in multiple stages

in order to explore the various applications for SICS method. First, the non-labelled λ -DNA and DNA rulers were used to estimate the resolution, SNR and throughput of the method. Multiple controls using fluorescence microscopy were performed to optimize the DNA surface density. These experiments were followed by the dCas-9-DNA complex SICS imaging. Multiple controls involving single-molecule imaging with AFM, optical-tweezers were additionally done to ensure the dCas-9 binding.

5.3.1 DNA rulers for SICS characterization

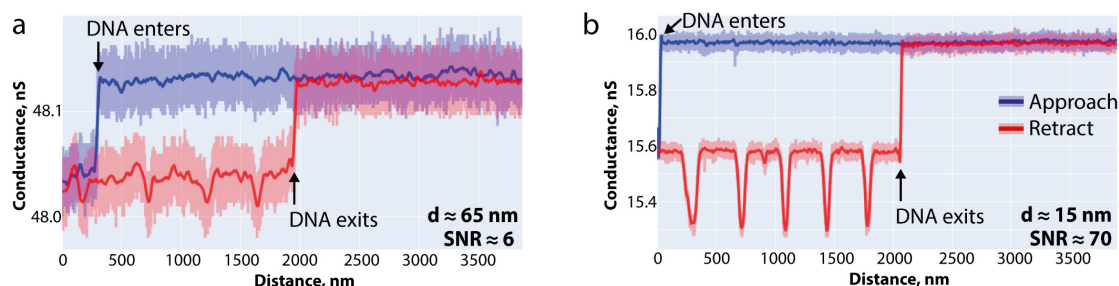


Figure 5.5 – Spatial resolution dependency on the diameter of the nanocapillary. (a) Current signature of a DNA ruler sample imaged with a 65 nm nanocapillary. (b) Corresponding current signature of the same molecule imaged with a 15 nm nanocapillary.

Our scanning ion-conductance spectroscopy approach is based on a slightly modified SICM setup which is able to record current traces for the nanocapillary approach and retract (Figure 5.4). By applying a voltage bias between the inside and outside of the nanocapillary, ions flow through the solid-state nanopore and produce an ionic current which is measured. When a molecule or molecular assembly is passing through the opening of the pore, the change in ionic current is registered, similarly to a current drop in free translocations. Scanning of the surface-immobilized DNA molecule is performed in a similar way as was previously demonstrated with optical-tweezers(212). However, in SICS, the DNA is immobilized on the surface, which is static (excluding Brownian motion of the free-end) and only the nanocapillary is axially moved. Optical tweezers allow recording the force signal as well, however it comes at a cost of the complexity of the setup. Furthermore, polymer bead cannot be positioned close to the nanocapillary, since the nanocapillary scatters the light, thus perturbing the optical trap which results in a distance close to the nanocapillary, where the DNA cannot be imaged. Furthermore, the surface-immobilized DNA platform allows to scan the same molecule multiple times and average the signal from multiple current traces for better sensitivity and/or dynamics.

One of the most important and yet the most challenging aspects of the SICS is spatial resolution and SNR dependency on the diameter of the nanocapillary. This is a common concept well known in a SICM field, where it is assumed that the lateral resolution of the SICM is $\approx 3r$, where r is the radius of the pipette(77). However, the SNR of the current has is not only dependant on the size of the pore but is dependant on the axial thickness of the opening (212; 186). This also leads to a large distribution of the conductance values of nanocapillaries of similar measured

diameter (Figure 4.3a).

5.3.2 Lateral resolution estimation and SNR improvement strategies

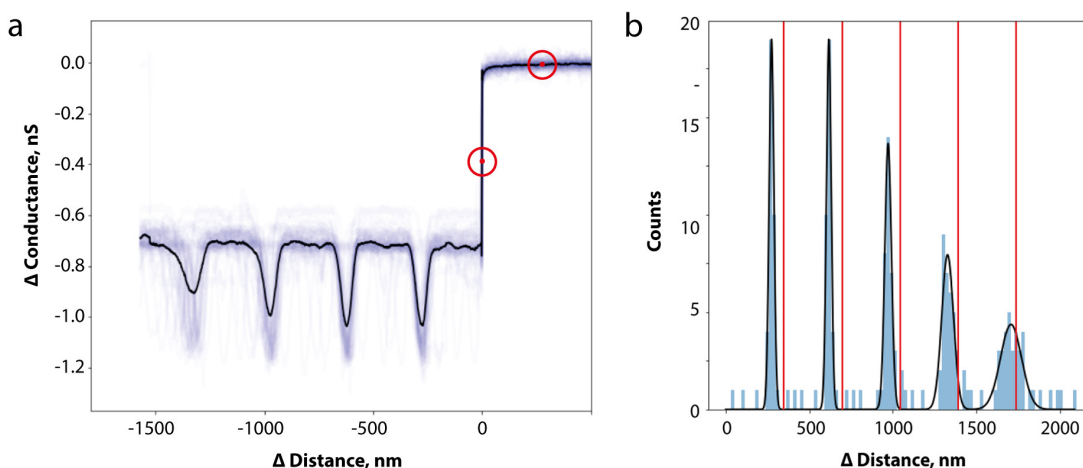


Figure 5.6 – Spatial current signal resolution and averaging signals from multiple molecules. (a) A cumulative current trace from multiple ($N=81$) DNA rulers. Signals were aligned based on points marked in red. (b) Detected peak positions of each DNA ruler fragment with fitted Gaussian distributions.

The signal-to-noise ratio (SNR) estimated in this study, was defined as the ratio between the signal modulation δG produced by the dumbbell fragment and the baseline current root-mean-square I_{RMS} measured at the operating bandwidth. As it is demonstrated in Figure 5.5, the SNR of the dumbbell fragments for the 65 nm nanocapillary was estimated to be 6.2, when for the 15 nm nanocapillary it was found to reach 70. The especially high SNR for small capillaries was achieved partially, due to a slow-scanning speed (1000nm/s), which translates to a translocation speed of $\sim 3 \text{ ntms}^{-1}$, which can be reduced even further. Such a slow translocation speed is only possible when performing a controlled translocation of a single DNA. However, in this case, our SNR is limited by the 3D geometry of the opening of nanocapillary only, which limits our spatial resolution to ~ 100 nucleotides.

The scanning capability of SICS approach allows to straightforwardly image multiple molecules (Figure 5.6) and thus estimate the desired signal parameters with a high statistical significance. However, the measured positions of dumbbell segments were different to the estimated ones due to DNA stretching(176) under applied electrical bias (300 mV). The stretching effect is more pronounced further from a surface and the position difference can be fitted linearly (176), thus simplifying the further data analysis.

Current signal resolution can be estimated experimentally from the acquired curves as it is shown in Figure 5.7. By using a 15 nm nanocapillary we have estimated full-width-half maximum of the Gaussian fit of 26.5 ± 2.1 . Interestingly, we haven't observed any FWHM dependency on the position with a respect to the distance to the surface, so this lateral

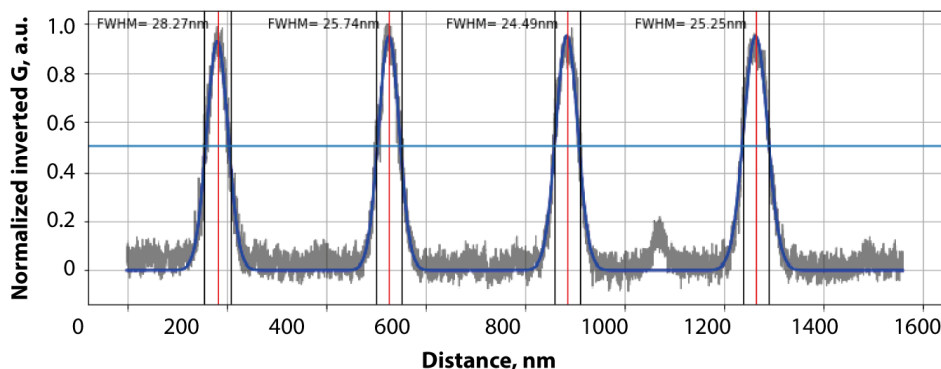


Figure 5.7 – Lateral current signal resolution. A current signature of a DNA ruler sample imaged with a 15 nm nanocapillary with fitted Gaussian distributions. A small amplitude peak in between dumbbell fragments is related to a electrostatic sticking of possible contaminants in a solution.

resolution value can be used equally within the DNA length. However, as it is showed in Figure 5.8 lateral resolution does not correspond to a localization precision of the dumbbell fragment, which can go beyond a few nm (Figure 5.8b) by accumulating the approach-retract current signals from the same molecule scanned multiple times.

5.3.3 SICS application for DNA-protein complex detection

In order to demonstrate the versatility of the technique, we have performed the SICS experiments by using a dCas-9 protein-DNA complex as a model system for our study. Our experiments were performed similarly as it was demonstrated previously(176) by employing optical tweezers, however, we aimed to demonstrate the advantages of our method such as repetitive imaging of the same molecule and correlative SICS approach.

First, a number of control experiments were performed to independently confirm the dCas-9 binding to DNA. Recent advances in low-force atomic-force microscopy (AFM) imaging demonstrated an ability to image Cas-9 protein in physiological conditions(213). Motivated by these achievements, we have performed single-molecule AFM imaging with a peak-force modality. As shown in Figure 5.9 an AFM is not suitable to evaluate dCas-9 binding on long DNA strands, so 600 bp λ -DNA segments, electrostatically immobilized on a mica surface, were used. dCas-9 was incubated together with λ -DNA with and without gRNAs, thus performing positive and negative controls (Figure 5.9b-c AFM dCas-9). dCas-9 binding was indeed confirmed by AFM imaging, however, the throughput of such experiments is typically low and makes it impractical to perform a control on long DNA molecules (10 kb), that are used for SICS experiments.

Secondly, single-molecule fluorescence microscopy imaging of 10kb long λ -DNA arrays was done to perform an additional control and to estimate the dCas-9 binding efficiency

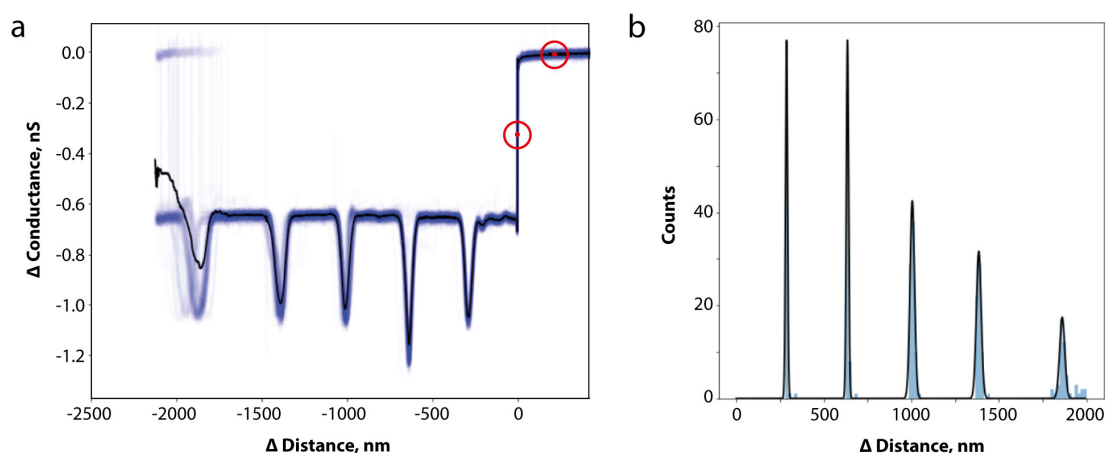


Figure 5.8 – Spatial current signal resolution and averaging signals from the same molecule. (a) A cumulative current trace from the same DNA ruler molecule scanned multiple ($N=89$) times. Signals were aligned based on points marked in red. (b) Detected peak positions of each DNA ruler fragment with fitted Gaussian distributions.

over the large ($50\mu m \times 50\mu m$ FOV and under the identical experimental conditions (400mM KCl, pH=7.5). DNA imaging was done similarly as in previously demonstrated DNA curtain workflow(214). However, for fluorescence imaging a molecular oxygen scavenging system was used as described in the methods section. SM fluorescence imaging revealed, that dCas-9 proteins tend to attach to DNA with 30-50 % efficiency. However, a significant amount of unspecific binding was also observed by performing step-wise photobleaching experiments at a single-molecule level (Figure 5.10). Specifically, more than 2 distinct fluorescence levels were observed, pointing to excess labelling of dCas-9 protein with a fluorescent label or multiple dCas-9 proteins attached to a single DNA. This control not just proved the dCas-9 binding, but also gave us additional information about the dCas-9 binding efficiency.

5.3.4 Correlative SICS and SM fluorescence measurement

To demonstrate the ability of the simultaneous SM fluorescence and SICS recording, we have performed a correlative SM fluorescence and SICS measurement of the DNA-dCas-9 complex. The most challenging part of the measurement was the requirement to use an oxygen-scavenging system to prevent the bleaching of Alexa-647 labelled dCas-9 and enable to perform a fluorescence imaging for a sustained period of time (20-40 s). However, the presence of glucose oxidase and catalyze in the solution used for imaging resulted in significant contamination of the nanocapillary, likely due to an electrostatic sticking of proteins to negatively charged glass. The standard use of TWEEN-20 detergent was not sufficient to mitigate this effect. The resulting current signal was unstable with an applied 200 mV bias voltage. Interestingly, we were still able to observe the controlled dCas-9 translocation event as it is shown in Figure 5.11. Unexpectedly, the recorded DNA-dCas-9 conductance signal was

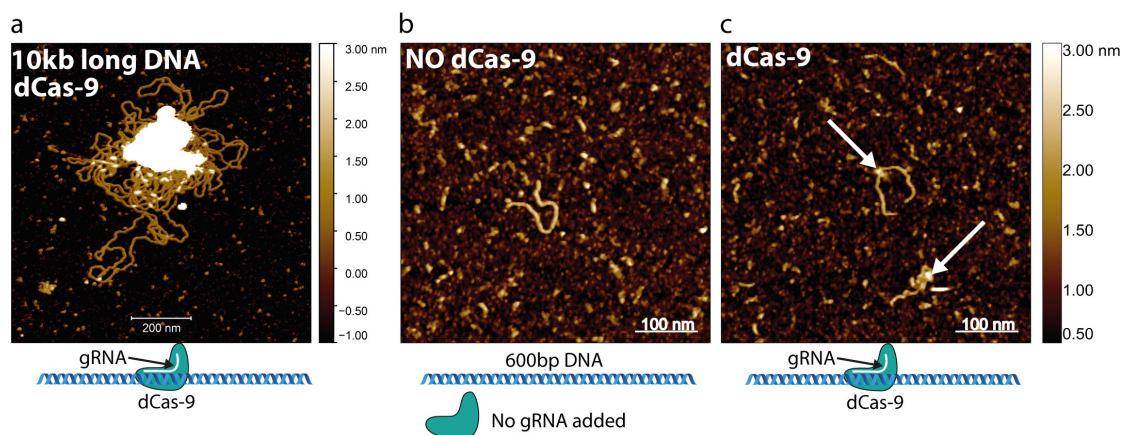


Figure 5.9 – Atomic force microscopy imaging of DNA-dCas-9 complex. (a) AFM image of 10kb long DNA incubated with dCas-9 and gRNA, demonstrating that AFM analysis is not feasible on long DNA sequences. (b) A negative control experiment with an absence of gRNA with no observed dCas-9 binding. (c) A positive control, with gRNA present in a solution with 2 dCas-9 binding events in a field-of-view.

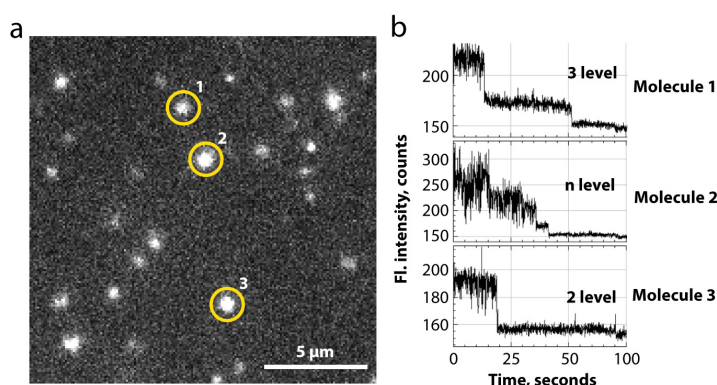


Figure 5.10 – Single-molecule fluorescence microscopy imaging of immobilized DNA-dCas-9 complex. (a) A single widefield image showing the surface distribution of DNA-dCas-9 complexes labelled with Alexa-647 dye. (b) Fluorescence intensity vs time, measured in the areas marked in (a), showing the different bleaching behaviour of different molecules.

inverted, compared to the measurements in a solution without protein residues. We speculate that this effect is due to the crowding of the aperture of nanocapillary with proteins present in a solution. During the translocation event negatively charged DNA is entering the pore opening, thus dislocating a fraction of proteins, that locally increases the ionic-current as it can be seen in Figure 5.11c. Finally, the current signal can be co-aligned together with the emission signal measured in a certain area, demonstrating, in a correlative manner, the ability to position the nanocapillary in a specified point on the sample and controllably translocate protein of interest, thus acquiring a current signature.

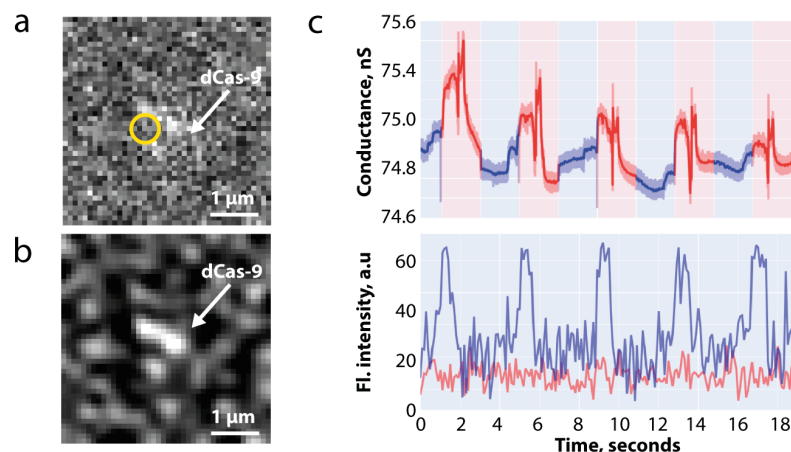


Figure 5.11 – Correlative single-molecule fluorescence and SICS measurement. (a) A single widefield image showing the surface immobilized DNA-dCas-9 complex labelled with Alexa-647 dye. (b) Band-passed image from (a) for improved visualization of the protein. (c) A correlative recording of ionic current (top) co-aligned with fluorescence intensity (bottom) measured from the location marked in (a) plotted in blue and fluorescence intensity from the background plotted in red. The yellow circle marked in (a) also signifies the approach point of the nanocapillary.

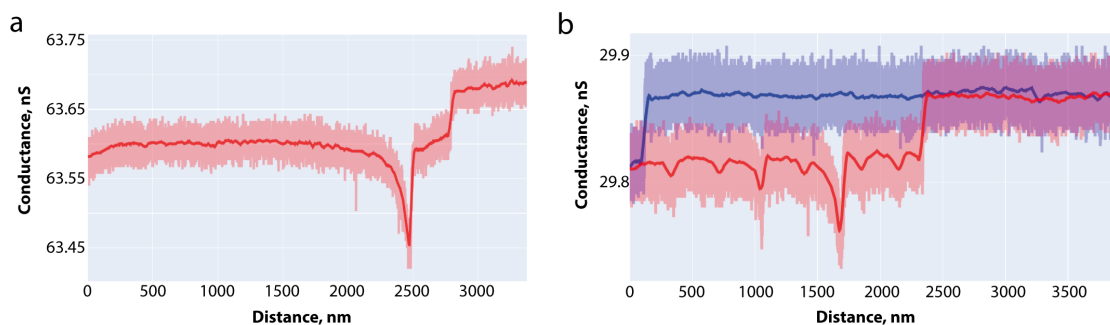


Figure 5.12 – SICS measurements of DNA-dCas-9 complexes. (a) 10kb long λ -DNA-dCas-9 complex measured in 400 mM KCl solution. (b) DNA ruler-dCas-9 complex measured in 400 mM KCl solution.

5.3.5 dCas-9 binding characterization on λ -DNA and DNA rulers

Multiple measurements were performed on DNA-dCas-9 complexes to estimate the dCas-9 binding location. 10kb long λ -DNA, together with 8.2kb long DNA ruler constructs were used for experiments. Corresponding current traces for λ -DNA (a) and for DNA-ruler construct (b) can be seen in the Figure 5.12. However, obtaining reliable statistics of binding locations were particularly challenging. The main problem of detecting proteins like dCas-9 is sticking to the surface of the opening of glass nanocapillary. To mitigate this effect, 0.01% of TWEEN-20 surfactant was present in the KCl solutions, however, it was not sufficient to mitigate the electrostatic sticking. We have also tried to perform the measurements in the pH, which

would be closer to the isoelectric point of dCas-9 ($pI \approx 8.9$), which also had no effect, likely to non-homogeneous charge distribution on the protein.

5.4 Conclusion and Outlook

The field of solid-state nanopores is advancing at a rapid pace in the last decade. However, the nanopore-based DNA sequencing, demonstrated with biological pores, remains elusive due to a variety of reasons. The most important and yet most challenging issue is high translocation speeds, resulting in the insufficient sampling of a current signal. Variety of approaches such as solution gradient in cis and trans chambers (91), using optical tweezers for precise DNA positioning(176) or translocating DNA through a device with two nanopores(215). In parallel, SICM was developed to use a solid-state nanopore probe to scan the surface, by precisely positioning glass-nanocapillary (72), demonstrating the nanometer-range resolution on a cell membrane (125). In this proof-of-principle study, we have utilized the SICM platform to perform controlled translocations of DNA molecules in a surface array format. To evaluate our method we first established the resolution and SNR metrics of our technique demonstrating the lateral FWHM of $26.5 \pm 2.1\text{nm}$ and SNR up to 70. The SNR can be increased n fold with signal averaging by performing multiple scans of the same molecule. Subsequently, we have performed the SICS experiments on DNA-dCas-9 complexes, demonstrating the ability to localize the protein on the DNA strand. Furthermore, we have performed a correlative single-molecule fluorescence imaging and SICS experiment, showing the proof-of-principle framework for correlative measurement. However, the protein measurements were hindered by the electrostatic sticking of the protein to the negatively charged silicon dioxide surface. The following issue can be solved by modifying the nanocapillaries with chemically inert polyethylene glycol coating, however, this approach was out of the scope of this particular study. The further improvements of this approach can include the more complex design of the solid-state nanopore probes such as incorporating a 2D material at the tip and reducing the pore opening size and especially thickness to the dimensions similar to biological nanopores. The following modification could dramatically increase the SNR and the signal resolution, bringing this technique closer to the ultimate goal of DNA sequencing. Alternatively, SICS can be used to image various analytes on the DNA molecules such as methylation sites, DNA nicks that we are continuing to explore. We believe that SICM can be further improved to perform automatic screening of DNA arrays eventually leading to more capable point-of-care diagnostic devices.

6 Conclusion and Outlook

This final chapter of the thesis summarizes the previous chapters and provides a general, yet personal outlook for the different topics discussed in the thesis and hopefully brings a very needed connection between the fundamentally different fields of research.

During the following years, the computational approaches based on the strong a priori knowledge is becoming a standard in the microscopy community for various everyday tasks such as data labeling, de-noising, SMLM image reconstruction, etc. This yet previously unseen revolution is mainly driven by advances in artificial neural networks and widely available computational power. On top of that, SR fluorescence microscopy is often used on fixed cells processed with chemical fixatives, thus disturbing and changing the native cellular structure. In light of these problems, correlative methods are coming into the picture. This was one of the motivations for combining the SICM and SOFI microscopies. In this proof-of-principle paper, we have demonstrated that frequently SOFI is not giving the full picture of the cell state, which was in our approach easily attainable by the SICM microscopy. However, we were somewhat limited to fixed-cell imaging due to the phototoxic nature of SR fluorescence imaging. We demonstrated that SICM can be used to monitor live cell activity for multiple days(139), thus eliminating any doubts about the negative effects SICM can cause for the living cells. The logical continuation of correlative SICM story would be a turn to less phototoxic SR microscopy approaches, such as SIM or RESOLFT. Combined with far red-shifted fluorescent probes such as f-HM-SiR, the methods should extend the live-cell imaging capability and allow to monitor the living sample for a few hours or even days, which would be especially interesting for the biological problems such as cellular morphogenesis, differentiation, etc.

The 3D-SOFI approach used in our study was based on the image-splitting prism element, which allowed us to achieve the super-resolution to the Z-depth of $2.5\ \mu\text{m}$. However, most of the cells that we have, were thicker ($5\ \mu\text{m}$ - $10\ \mu\text{m}$) as we have estimated with SICM measurements. This fostered the development of a remote focusing system to image the full thickness of a single cell. The developed system is based on the commercial adaptive optics setup installed in a detection path of the widefield microscope. The remote focusing with a deformable mirror enabled us to record multiple planes of the sample and measure for several

Chapter 6. Conclusion and Outlook

hours using a relatively low light intensity required by a self-blinking dye while the sample was stabilized in Z with an infrared laser. Constant stabilization in Z eliminated the need to perform a complex axial drift correction and greatly simplified acquisition procedure. The image stacks then were processed using SOFI and SMLM approaches, allowing us to obtain the 3D super-resolution maps of the whole cells. This simple approach can be easily implemented on the setups with adaptive optics modules, requiring very little effort and can also be used for correlative approaches to image deep into the tissues.

During the first experiments with a correlative SICM, we realized the importance of well-characterized nanocapillaries required for robust SICM imaging. One of the problems, while SICM have not become a mainstream technology for imaging as AFM did, is the availability of SICM probes. For AFM the cantilevers are easily obtainable from various suppliers and are relatively cheap, however, SICM requires well-characterized nanocapillaries that can only be manufactured by specialized capillary pulling devices. However, manufacturing the glass capillaries with openings below 100 nm with short taper length is undoubtedly difficult. On top of that, nanocapillaries with openings below 50 nm are complicated to fill with water-based solutions. The pre-filling with ethanol often results in the formation of nanobubbles, that can block the pore or result in increased electrical noise levels. Using the capillaries with incorporated filaments are also not always possible due to limited availability and the additional deformation of the nanocapillary opening, which can result in non-circular ePSF. To solve the problem of nanocapillary filling we have developed microwave radiation based filling approach, which was invented by experimenting with various filling methods based on the local heating of the solution. This allowed us to manufacture batches of precisely electrically and morphologically characterized quartz nanocapillaries with the diameters estimated using SEM and fill batches of 20-30 nanocapillaries, with opening diameters ranging from 5 to 50 nm. I believe, that this nanocapillary filling method which we have published in high detail will foster novel applications for glass-based solid-state nanopores and will help the SICM community to grow even further. The availability of pre-filled and well-characterized glass nanocapillaries was a key for the further SICS experiments that we have performed.

The solid-state nanopores for single-molecule sensing have shown their potential in recent years for various applications, ranging from DNA-protein interactions, poly-peptide sensing, DNA-information encoding, etc. However, the nature of the free translocations and the fast speed (10-10000 bp/ms) at which they are happening is still limiting this approach for applications such as DNA-sequencing, due to a finite bandwidth of the electrical signal amplifiers. On the other hand, controlled translocations with reduced translocation speeds through solid-state nanopores were demonstrated with optical tweezers or dedicated nanopositioning elements with immobilized DNA molecules. Controlled DNA translocations for DNA-protein interaction studies using optical tweezers were demonstrated and extensively studied in our group. However, the added ability to measure the force of single-molecule interactions with a nanopore comes at the cost of the complexity of the experiment. The OT approach is also not suitable for repeated measurement of the same DNA molecule that would allow to study the dynamics of the molecular processes at the single-molecule level or to increase the SNR

by averaging a signal from multiple measurements. The previous experience with controlled DNA translocations using optical tweezers resulted in a natural continuation of the method employing the SICM abilities for a well-established positioning of the nanocapillary.

The SICS work demonstrated in the thesis is the basis of an upcoming publication that will demonstrate the advantages of the modified scanning-ion conductance microscopy setup for controlled electrical measurements of the surface-immobilized DNA molecules. The small (10-20nm) nano-capillaries used, combined with slow translocation speeds allowed us to be not limited by the electrical noise, thus demonstrating the unprecedented SNR. We have explored the various molecules such as DNA-rulers, that we used for overall system characterization, DNA-Nicks - that are used to study DNA damage, DNA-barcodes, that can be employed to map the species based on the positions of TCGA sequences and finally dCas-9-DNA interactions that are important to evaluate the precision of this genome-editing tool. However, we obtained the best results by using modified DNA molecules with covalent modifications. The problem of protein sticking to a glass nanopore surface hindered us to achieve high-throughput measurements with dCas-9 proteins. The problem might be tackled by employing various polymer coatings to make the negatively charged surface of the glass pore inert by reducing the surface charge. The future advancements of this method might employ the more advanced glass-nanopore probes with a reduced sensing thickness, by using 2D materials, that can advance solid-state nanopore field towards DNA-sequencing or by applying recently developed localization algorithms(216) to increase the spatial resolution of the current signal.

I hope that the final conclusions summarized and motivated why the research questions were tackled. The interdisciplinary nature of the thesis gave me valuable experience in multiple research fields. I believe that the future of microscopy is going to bring more synergy for the different types of imaging, thus making multimodal microscopy a standard approach to solve biological problems.

7 An Image Portfolio

During the whole PhD journey the visual side of it was one of the most motivating and rewarding factors to me. Alongside my scientific career I am an amateur 3D artist, focusing mainly on scientific visualizations. My images benefited multiple scientific projects besides my own research. On top of that, I was doing scientific visualization training for Master students in EPFL during my Teaching Assistance for Prof. Sawley Mark. This portfolio reflects a few most honorable images I created during my PhD years.

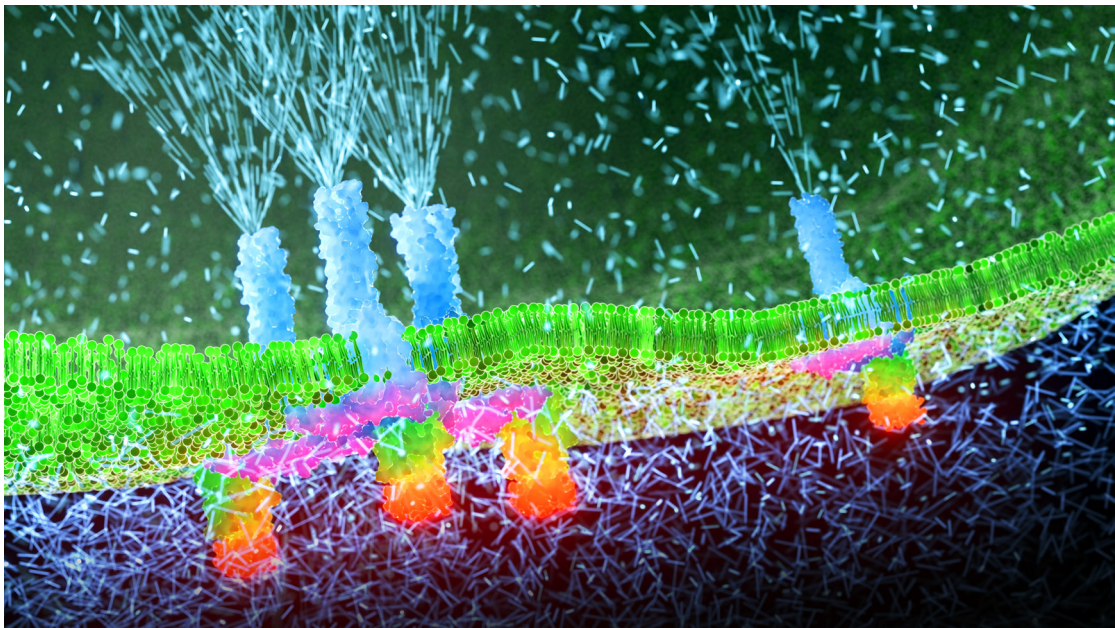


Figure 7.1 – Scientific 3D render prepared for 2018 ACCES Visualization Contest organized by EPFL. The image was awarded 2nd prize. Images illustrates aggregated voltage gated calcium ion channels in a lipid bilayer.



Figure 7.2 – 3D render of the SICM topography of a neuron cell, overlaid with SIM fluorescence image.

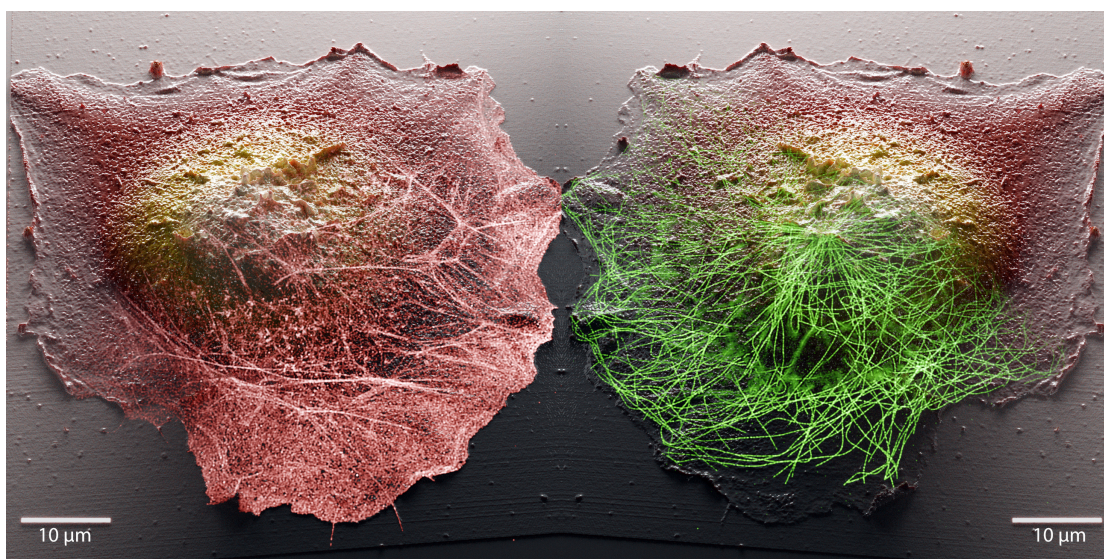


Figure 7.3 – The particular correlative 2-color image of a fixed COS-7 cell was generated using a combination of scanning ion-conductance microscopy (SICM) and super-resolution optical fluctuation imaging (SOFI) and rendered in 3D software. The image was awarded 3rd prize in Voir Est Savoir Scientific Image Competition. The full decription in a video format can be found here: [Link to the video](#).

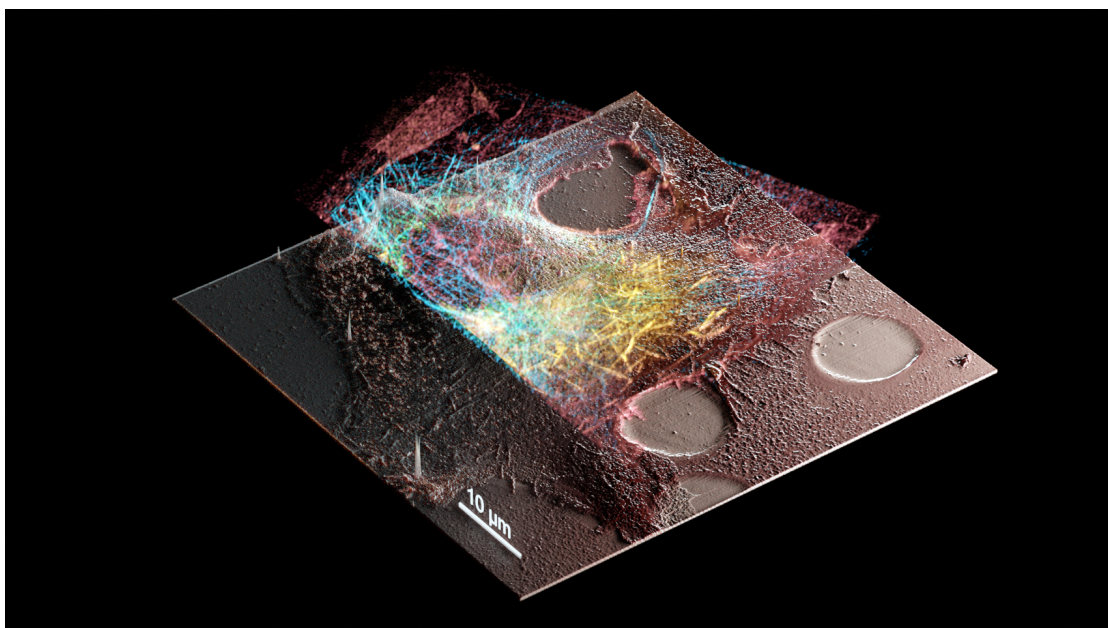


Figure 7.4 – Correlative 2-color image of a fixed COS-7 cell which was generated using a combination of scanning ion-conductance microscopy (SICM) and 3D super-resolution optical fluctuation imaging (SOFI) and rendered in 3D software. The full movie can be found here: [Link to the video](#).

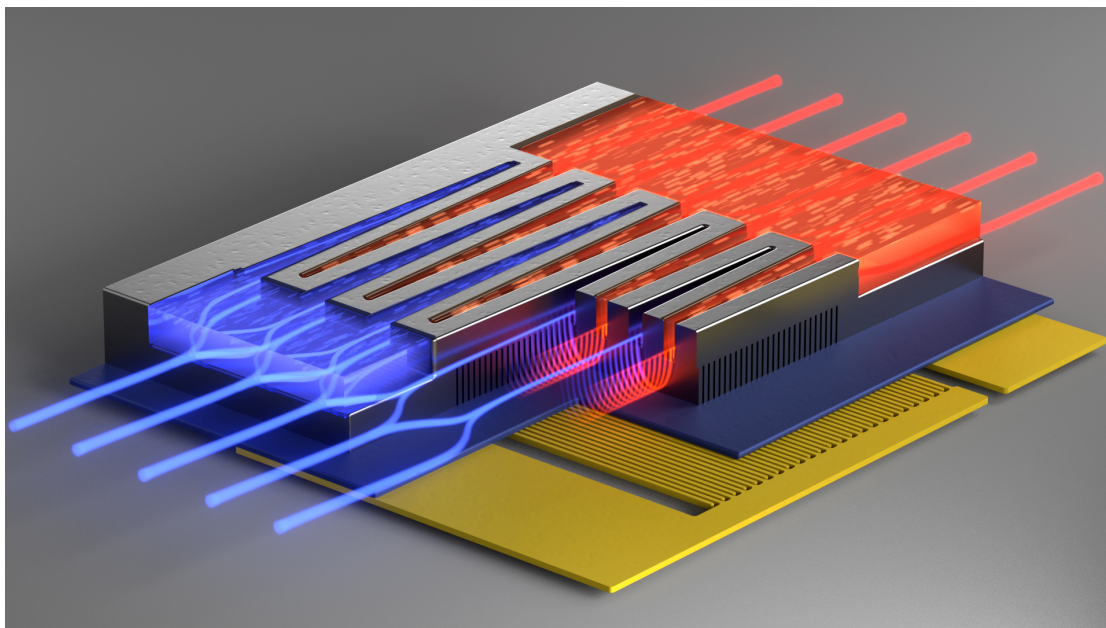


Figure 7.5 – Scientific render which was featured in the publication **Co-designing electronics with microfluidics for more sustainable cooling** by Remco van Erp et al. (Nature volume 585, pages211–216 (2020)) and the press release. The full rendered movie can be found as a Supplementary Movie 1 in the paper. Illustration shows the fluid flow through the mMMC structure. Blue lines indicate the cold coolant flow entering the chip, and red lines indicate the hot coolant leaving the chip (217)

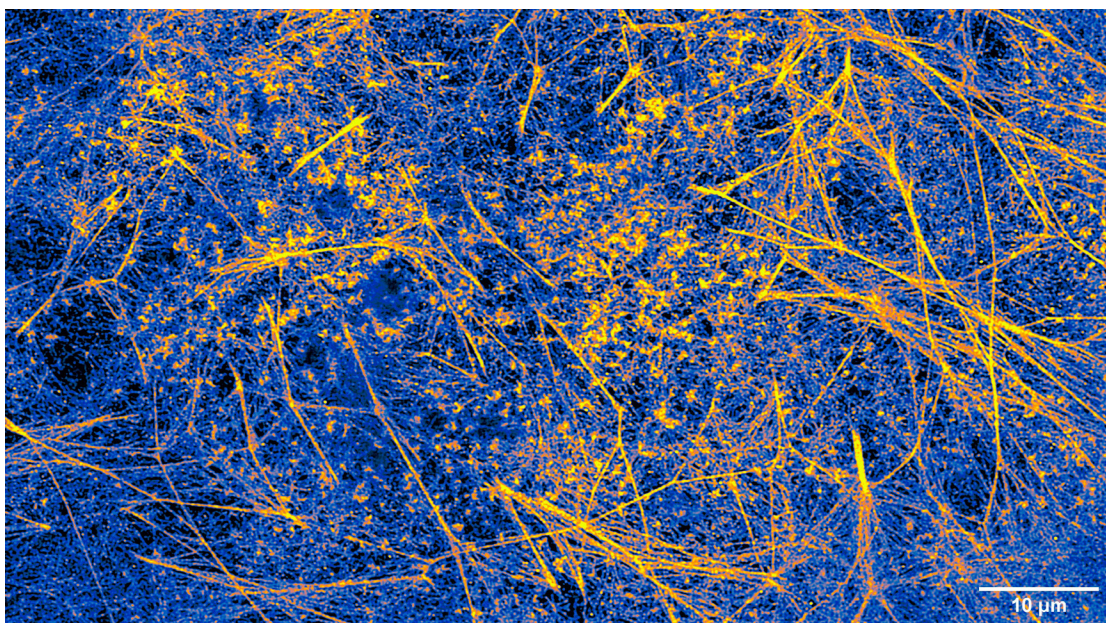


Figure 7.6 – 4th order SOFI image of phalloidin-f-HM-SiR labelled f-actin in COS-7 cells, showing the distribution of a fibrous actin network.

8 Scientific contributions

Alongside the scientific papers that are presented in the thesis chapter, I contributed to a several other publications during Bachelor, Master and PhD years. **The full list** of publications with the exact contributions in a chronological sequence is listed below.

1. **Lipid dip-pen nanolithography on self-assembled monolayers.** Martynas Gavutis, **Vytautas Navikas**, Tomas Rakickas, Sarūnas Vaitekūnas and Ramūnas Valiokas. *J. Microelectromech. Syst.* 26 025016. (2016).

I am the co-shared first author of this manuscript and I contributed by performing all experiments, analysis the data and partially writing the final manuscript.

2. **Wide-field spectral super-resolution mapping of optically active defects in hBN.** Jean Comtet, Evgenii Glushkov, **Vytautas Navikas**, Jiandong Feng, Vitaliy Babenko, Stephan Hofmann, Kenji Watanabe, Takashi Taniguchi, Aleksandra Radenovic. *Nano Lett.* (2019), 19, 4, 2516–2523.

I aided in building the optical setup and performing the data analysis. I also discussed the results and proof-read and corrected the final manuscript.

3. **Fluorescent Nanodiamonds as Versatile Intracellular Temperature Sensors.** Evgenii Glushkov, **Vytautas Navikas**, Aleksandra Radenovic. *CHIMIA International Journal for Chemistry*, 73, 1, (2019), pp. 73-77(5).

For this review article I aided in preparing the figures, proof-reading and correcting the manuscript.

4. **Facile Production of Hexagonal Boron Nitride Nanoparticles by Cryogenic Exfoliation.** Ngoc My Hanh Duong, Evgenii Glushkov, Andrey Chernev, **Vytautas Navikas**, Jean Comtet, Minh Anh Phan Nguyen, Milos Toth, Aleksandra Radenovic, Toan Trong Tran, Igor Aharonovich. *Nano Lett.* (2019), 19, 8, 5417–5422.

I performed SMLM imaging experiments and analysed blinking kinetics of single-photon emitters used in this study. I have also discussed the results, proof-read and corrected the manuscript.

5. **Scanning Probe-Directed Assembly and Rapid Chemical Writing Using Nanoscopic Flow of Phospholipids.** Vytautas Navikas, Martynas Gavutis, Tomas Rakickas, Ramūnas Valiokas. *ACS Appl. Mater. Interfaces* (2019), 11, 31, 28449–28460.

I am the first author of this paper, which is based on my Master thesis results. I conceived the idea, performed all experiments, data analysis and wrote the manuscript together with M.G. with a help from the all co-authors.

6. **Waveguide-based platform for large-FOV imaging of optically-active defects in 2D materials.** Evgenii Glushkov, Anna Archetti, Anton Stroganov, Jean Comtent, Mukeshchand Thakur, Vytautas Navikas, Martina Lihter, Juan Marin Gonzalez, Vitaliy Babenko, Stephan Hofmann, Suliana Manley, Aleksandra Radenovic. *ACS Photonics* (2019), 6, 12, 3100–3107

I aided in preparing the final figures and data analysis. I have proof-read and corrected the manuscript.

7. **Fixed DNA Molecule Arrays for High-Throughput Single DNA–Protein Interaction Studies.** Marijonas Tutkus, Tomas Rakickas, Aurimas Kopūstas, Sarūnė Ivanovaitė, Oskaras Venckus, Vytautas Navikas, Mindaugas Zaremba, Elena Manakova, and Ramūnas Valiokas. *Langmuir* (2019), 35, 17, 5921–5930.

The contributed by creating a silicon mater fabrication technology using a soft-lithography methods which was the basis of my Master thesis. I also aided in making figures, discussed the results, proof-read and corrected the manuscript.

8. **High speed multi-plane super-resolution structured illumination microscopy of living cells using an image-splitting prism.** Adrien Descloux, Marcel Muller, Vytautas Navikas, Andreas Markwirth, Robin Van Den Eynde, Tomas Lukes, Wolfgang Hubner, Theo Lasser, Aleksandra Radenovic, Peter Dedecker, Thomas Huser. *Nanophotonics* (2020), 9(1): 143–148.

I prepared the samples, together with A.D. performed the imaging experiments, aided in making figures, discussed the results and data analysis, proof-read and corrected the manuscript.

9. **High-Throughput Nanocapillary Filling Enabled by Microwave Radiation for Scanning Ion Conductance Microscopy Imaging.** Vytautas Navikas, Samuel M. Leitao, Sanjin Marion, Sebastian James Davis, Barney Drake, Georg E. Fantner, and Aleksandra Radenovic. *ACS Appl. Nano Mater.* (2020 07 02), 3, 8, 7829–7834.

The manuscript is presented as the thesis chapter.

10. **Correlative two and three-dimensional Super-Resolution and Scanning Ion Conductance Microscopy of single cells.** Vytautas Navikas, Samuel M. Leitao, Kristin S. Grussmayer, Adrien Descloux, Klaus Yserentant, Phillip Werther, Georg E. Fantner, Aleksandra Radenovic. *Nat. Commun.* 12, 4565 (2021).

The manuscript is presented as the thesis chapter.

-
11. **Bioorthogonal red and far-red fluorogenic probes for wash-free live-cell and super-resolution microscopy.** Philipp Werther, Klaus Yserentant, Felix Braun, Kristin Grussmayer, **Vytautas Navikas**, Miao Yu, Zhibin Zhang, Michael J. Ziegler, Christoph Mayer, Antoni J. Gralak, Marvin Busch, Weijie Chi, Frank Rominger, Aleksandra Radenovic, Xiaogang Liu, Edward A. Lemke, Tiago Buckup, Dirk-Peter Herten, Richard Wombacher. Accepted, ACS Central Science. (2021).

I prepared the samples, performed a super-resolution imaging (SOFI) of actin and analyzed the data. I also aided in making figures, discussed the results and data analysis, proof-read and corrected the manuscript.

12. **Experimental combination of Super-resolution Optical Fluctuation Imaging with Structured Illumination Microscopy for large Fields-of-View.** Adrien Descloux, Kristin Grussmayer, **Vytautas Navikas**, Dora Mahecic, Suliana Manley, Aleksandra Radenovic. ACS Photonics 8, 8, 2440–2449, (2021).

I prepared the 2 color samples, aided in making figures, discussed the results and data analysis, proof-read and corrected the manuscript.

13. **Direct growth of hexagonal boron nitride on photonic chips for high-throughput characterization.** Evgenii Glushkov, Noah Mendelson, Andrey Chernev, Ritika Ritika, Martina Lihter, Reza R. Zamani, Jean Comtet, **Vytautas Navikas**, Igor Aharonovich, Aleksandra Radenovic. ACS Photonics, 8, 7, 2033–2040, (2021).

I aided in making figures, discussed the results and data analysis, proof-read and corrected the manuscript.

14. **Adaptive optics enables multimode 3D super-resolution microscopy via remote focusing.** **Vytautas Navikas**, Adrien C. Descloux, Kristin S. Grussmayer, Sanjin Marion and Aleksandra Radenovic. Nanophotonics, vol. 10, no. 9, 2021, pp. 2451-2458, (2021).

The manuscript is presented as the thesis chapter.

15. **Tracking mammalian cell surface dynamics using time-resolved scanning ion conductance microscopy.** Samuel M. Leitao, Barney Drake, Katarina Pinjusic, Xavier Pierrat, **Vytautas Navikas**, Adrian P. Nievergelt, Charlène Brillard, Denis Djekic, Aleksandra Radenovic, Alex Persat, Daniel B. Constam, Jens Anders and Georg E. Fantner. Accepted, ACS Nano. (2021).

I made 3D rendered figures based on the SICM time-lapse microscopy data as well as the 3D rendered movies. I have also provided SEM characterized nanocapillaries and discussed the results, data analysis, proof-read and corrected the manuscript.

16. **Engineering optically active defects in hexagonal boron nitride using focused ion beam and water.** Evgenii Glushkov, Michal Macha, Esther Rath, Vytautas Navikas, Nathan Ronceray, Cheol Yeon Cheon, Ahmet Avsar, Ahmed Aqeel, Kenji Watanabe, Takashi Taniguchi, Ivan Shorubalko, Andras Kis, Georg Fantner and Aleksandra Radenovic. Under review.

Chapter 8. Scientific contributions

I analysed a correlative SMLM and SPM data, contributed in making figures, discussed the results, proof-read and corrected the manuscript.

Bibliography

- [1] Adam J.M. Wollman, Richard Nudd, Erik G. Hedlund, and Mark C. Leake. From animaculum to single molecules: 300 years of the light microscope, apr 2015.
- [2] Max Born, Emil Wolf, A B Bhatia, P C Clemmow, D Gabor, A R Stokes, A M Taylor, P A Wayman, and W L Wilcock. *Principles of Optics: Electromagnetic Theory of Propagation, Interference and Diffraction of Light*. Cambridge University Press, 7 edition, 1999.
- [3] Niccolò Banterle, Khanh Huy Bui, Edward A. Lemke, and Martin Beck. Fourier ring correlation as a resolution criterion for super-resolution microscopy. *Journal of Structural Biology*, 183(3):363–367, sep 2013.
- [4] A. Descloux, K. S. Größmayer, and A. Radenovic. Parameter-free image resolution estimation based on decorrelation analysis. *Nature Methods*, 16(9):918–924, sep 2019.
- [5] Martin Chalfie, Yuan Tu, Ghia Euskirchen, William W. Ward, and Douglas C. Prasher. Green fluorescent protein as a marker for gene expression. *Science*, 263(5148):802–805, feb 1994.
- [6] Roger Kilgard, Andrew B. Heim, and Roger Y. Tsien. Improved green fluorescence. *Nature*, 373(6516):663–664, feb 1995.
- [7] Michael J. Rust, Mark Bates, and Xiaowei Zhuang. Sub-diffraction-limit imaging by stochastic optical reconstruction microscopy (STORM). *Nature Methods*, 3(10):793–795, oct 2006.
- [8] E. A. Ash and G. Nicholls. Super-resolution aperture scanning microscope. *Nature*, 237(5357):510–512, 1972.
- [9] Stefan W. Hell and Jan Wichmann. Breaking the diffraction resolution limit by stimulated emission: stimulated-emission-depletion fluorescence microscopy. *Optics Letters*, 19(11):780, jun 1994.
- [10] Thomas A. Klar and Stefan W. Hell. Subdiffraction resolution in far-field fluorescence microscopy. *Optics Letters*, 24(14):954, jul 1999.

Bibliography

- [11] Dominik Wildanger, Brian R. Patton, Heiko Schill, Luca Marseglia, J. P. Hadden, Sebastian Knauer, Andreas Schönle, John G. Rarity, Jeremy L. O'Brien, Stefan W. Hell, and Jason M. Smith. Solid Immersion Facilitates Fluorescence Microscopy with Nanometer Resolution and Sub-Ångström Emitter Localization. *Advanced Materials*, 24(44):OP309–OP313, nov 2012.
- [12] Roman Schmidt, Christian A. Wurm, Stefan Jakobs, Johann Engelhardt, Alexander Egner, and Stefan W. Hell. Spherical nanosized focal spot unravels the interior of cells. *Nature Methods*, 5(6):539–544, jun 2008.
- [13] Michael Hofmann, Christian Eggeling, Stefan Jakobs, and Stefan W. Hell. Breaking the diffraction barrier in fluorescence microscopy at low light intensities by using reversibly photoswitchable proteins. *Proceedings of the National Academy of Sciences of the United States of America*, 102(49):17565–17569, dec 2005.
- [14] Francisco Balzarotti, Yvan Eilers, Klaus C. Gwosch, Arvid H. Gynnå, Volker Westphal, Fernando D. Stefani, Johan Elf, and Stefan W. Hell. Nanometer resolution imaging and tracking of fluorescent molecules with minimal photon fluxes. *Science*, 355(6325):606–612, feb 2017.
- [15] M. G. L. Gustafsson. Surpassing the lateral resolution limit by a factor of two using structured illumination microscopy. SHORT COMMUNICATION. *Journal of Microscopy*, 198(2):82–87, may 2000.
- [16] Andrew G. York, Panagiotis Chandris, Damian Dalle Nogare, Jeffrey Head, Peter Wawrzusin, Robert S. Fischer, Ajay Chitnis, and Hari Shroff. Instant super-resolution imaging in live cells and embryos via analog image processing. *Nature Methods*, 10(11):1122–1130, nov 2013.
- [17] Reto Fiolka, Lin Shao, E. Hesper Rego, Michael W. Davidson, and Mats G.L. Gustafsson. Time-lapse two-color 3D imaging of live cells with doubled resolution using structured illumination. *Proceedings of the National Academy of Sciences of the United States of America*, 109(14):5311–5315, apr 2012.
- [18] D. Li, L. Shao, B.-C. Chen, X. Zhang, M. Zhang, B. Moses, D. E. Milkie, J. R. Beach, J. A. Hammer, M. Pasham, T. Kirchhausen, M. A. Baird, M. W. Davidson, P. Xu, and E. Betzig. Extended-resolution structured illumination imaging of endocytic and cytoskeletal dynamics. *Science*, 349(6251):aab3500–aab3500, aug 2015.
- [19] Tatjana Kleele, Timo Rey, Julius Winter, Sofia Zaganelli, Dora Mahecic, Hélène Perreten Lambert, Francesco Paolo Ruberto, Mohamed Nemir, Timothy Wai, Thierry Pedrazzini, and Suliana Manley. Distinct fission signatures predict mitochondrial degradation or biogenesis. *Nature*, 593(7859):435–439, may 2021.
- [20] Eric Betzig, George H. Patterson, Rachid Sougrat, O. Wolf Lindwasser, Scott Olenych, Juan S. Bonifacino, Michael W. Davidson, Jennifer Lippincott-Schwartz, and Harald F.

- Hess. Imaging intracellular fluorescent proteins at nanometer resolution. *Science*, 313(5793):1642–1645, sep 2006.
- [21] Sergey Ivanchenko, Carlheinz Röcker, Franz Oswald, Jörg Wiedenmann, and G. Ulrich Nienhaus. Targeted green-red photoconversion of EosFP, a fluorescent marker protein. *Journal of Biological Physics*, 31(3-4):249–259, dec 2005.
- [22] Ralf Jungmann, Christian Steinhauer, Max Scheible, Anton Kuzyk, Philip Tinnefeld, and Friedrich C. Simmel. Single-molecule kinetics and super-resolution microscopy by fluorescence imaging of transient binding on DNA origami. *Nano Letters*, 10(11):4756–4761, nov 2010.
- [23] Joerg Schnitzbauer, Maximilian T. Strauss, Thomas Schlichthaerle, Florian Schueder, and Ralf Jungmann. Super-resolution microscopy with DNA-PAINT. *Nature Protocols*, 12(6):1198–1228, jun 2017.
- [24] Daniel J. Nieves, Geva Hilzenrat, Jason Tran, Zhengmin Yang, Hugh H. MacRae, Matthew A.B. Baker, J. Justin Gooding, and Katharina Gaus. TagPaint: Covalent labelling of genetically encoded protein tags for DNA-PAINT imaging. *Royal Society Open Science*, 6(12), dec 2019.
- [25] Stefan Bretschneider, Christian Eggeling, and Stefan W. Hell. Breaking the diffraction barrier in fluorescence microscopy by optical shelving. *Physical Review Letters*, 98(21):218103, may 2007.
- [26] Roman Schmidt, Tobias Weihs, Christian A. Wurm, Isabelle Jansen, Jasmin Rehman, Stefan J. Sahl, and Stefan W. Hell. MINFLUX nanometer-scale 3D imaging and microsecond-range tracking on a common fluorescence microscope. *Nature Communications*, 12(1):1–12, dec 2021.
- [27] Kirti Prakash. At the molecular resolution with MINFLUX? *Preprints*, (February), feb 2021.
- [28] Curran Oi, Zoe Gidden, Louise Holyoake, Owen Kantelberg, Simon Mochrie, Mathew H. Horrocks, and Lynne Regan. LIVE-PAINT allows super-resolution microscopy inside living cells using reversible peptide-protein interactions. *Communications Biology*, 3(1):1–10, dec 2020.
- [29] Kalina L. Tosheva, Yue Yuan, Pedro Matos Pereira, Si n. Culley, and Ricardo Henriques. Between life and death: Strategies to reduce phototoxicity in super-resolution microscopy. *Journal of Physics D: Applied Physics*, 53(16):163001, apr 2020.
- [30] Kristin Großmayer, Tomas Lukes, Theo Lasser, and Aleksandra Radenovic. Self-Blinking Dyes Unlock High-Order and Multiplane Super-Resolution Optical Fluctuation Imaging. *ACS Nano*, 14(7):9156–9165, jun 2020.

Bibliography

- [31] Shin Nosuke Uno, Mako Kamiya, Toshitada Yoshihara, Ko Sugawara, Kohki Okabe, Mehmet C. Tarhan, Hiroyuki Fujita, Takashi Funatsu, Yasushi Okada, Seiji Tobita, and Yasuteru Urano. A spontaneously blinking fluorophore based on intramolecular spirocyclization for live-cell super-resolution imaging. *Nature Chemistry*, 6(8):681–689, jul 2014.
- [32] Gražvydas Lukinavičius, Claudia Blaukopf, Elias Pershagen, Alberto Schena, Luc Reymond, Emmanuel Derivery, Marcos Gonzalez-Gaitan, Elisa D’Este, Stefan W. Hell, Daniel Wolfram Gerlich, and Kai Johnsson. SiR-Hoechst is a far-red DNA stain for live-cell nanoscopy. *Nature Communications*, 6(1):1–7, oct 2015.
- [33] Philipp Werther, Klaus Yserentant, Felix Braun, Nicolai Kaltwasser, Christoph Popp, Mathis Baalmann, Dirk-Peter Hertel, and Richard Wombacher. Live-Cell Localization Microscopy with a Fluorogenic and Self-Blinking Tetrazine Probe. *Angewandte Chemie International Edition*, 59(2):804–810, jan 2020.
- [34] Elias A. Halabi, Dorothea Pinotsi, and Pablo Rivera-Fuentes. Photoregulated fluxional fluorophores for live-cell super-resolution microscopy with no apparent photobleaching. *Nature Communications*, 10(1):1–10, dec 2019.
- [35] Santosh Adhikari, Joe Moscatelli, Elizabeth M. Smith, Chiranjib Banerjee, and Elias M. Puchner. Single-molecule localization microscopy and tracking with red-shifted states of conventional BODIPY conjugates in living cells. *Nature Communications*, 10(1):1–12, dec 2019.
- [36] Russell E. Thompson, Daniel R. Larson, and Watt W. Webb. Precise nanometer localization analysis for individual fluorescent probes. *Biophysical Journal*, 82(5):2775–2783, may 2002.
- [37] Nicolas Olivier, Debora Keller, Pierre Gönczy, and Suliana Manley. Resolution Doubling in 3D-STORM Imaging through Improved Buffers. *PLoS ONE*, 8(7):e69004, jul 2013.
- [38] Bo Huang, Wenqin Wang, Mark Bates, and Xiaowei Zhuang. Three-dimensional super-resolution imaging by stochastic optical reconstruction microscopy. *Science*, 319(5864):810–813, feb 2008.
- [39] Marijn Siemons, Bas M. C. Cloin, Desiree M. Salas, Wilco Nijenhuis, Eugene A. Katrukha, and Lukas C. Kapitein. Comparing strategies for deep astigmatism-based single-molecule localization microscopy. *Biomedical Optics Express*, 11(2):735, feb 2020.
- [40] Ke Xu, Hazen P. Babcock, and Xiaowei Zhuang. Dual-objective STORM reveals three-dimensional filament organization in the actin cytoskeleton. *Nature Methods*, 9(2):185–188, feb 2012.
- [41] Sri Rama Prasanna Pavani, Michael A. Thompson, Julie S. Biteen, Samuel J. Lord, Na Liu, Robert J. Twieg, Rafael Piestun, and W. E. Moerner. Three-dimensional, single-molecule

- fluorescence imaging beyond the diffraction limit by using a double-helix point spread function. *Proceedings of the National Academy of Sciences of the United States of America*, 106(9):2995–2999, mar 2009.
- [42] Shu Jia, Joshua C. Vaughan, and Xiaowei Zhuang. Isotropic three-dimensional super-resolution imaging with a self-bending point spread function. *Nature Photonics*, 8(4):302–306, 2014.
- [43] Yoav Shechtman, Steffen J. Sahl, Adam S. Backer, and W. E. Moerner. Optimal point spread function design for 3D imaging. *Physical Review Letters*, 113(3):133902, sep 2014.
- [44] Yoav Shechtman, Lucien E. Weiss, Adam S. Backer, Steffen J. Sahl, and W. E. Moerner. Precise Three-Dimensional Scan-Free Multiple-Particle Tracking over Large Axial Ranges with Tetrapod Point Spread Functions. *Nano Letters*, 15(6):4194–4199, jun 2015.
- [45] Andrey Aristov, Benoit Lelandais, Elena Rensen, and Christophe Zimmer. ZOLA-3D allows flexible 3D localization microscopy over an adjustable axial range. *Nature Communications*, 9(1):1–8, dec 2018.
- [46] Gleb Shtengel, James A. Galbraith, Catherine G. Galbraith, Jennifer Lippincott-Schwartz, Jennifer M. Gillette, Suliana Manley, Rachid Sougrat, Clare M. Waterman, Pakorn Kanchanawong, Michael W. Davidson, Richard D. Fetter, and Harald F. Hess. Interferometric fluorescent super-resolution microscopy resolves 3D cellular ultrastructure. *Proceedings of the National Academy of Sciences of the United States of America*, 106(9):3125–3130, mar 2009.
- [47] N. Bourg, C. Mayet, G. Dupuis, T. Barroca, P. Bon, S. Lécart, E. Fort, and S. Lévêque-Fort. Direct optical nanoscopy with axially localized detection. *Nature Photonics*, 9(9):587–593, sep 2015.
- [48] Sara A. Jones, Sang Hee Shim, Jiang He, and Xiaowei Zhuang. Fast, three-dimensional super-resolution imaging of live cells. *Nature Methods*, 8(6):499–505, jun 2011.
- [49] T. Dertinger, R. Colyera, G. Iyer, S. Weiss, and J. Enderlein. Fast, background-free, 3D super-resolution optical fluctuation imaging (SOFI). *Proceedings of the National Academy of Sciences of the United States of America*, 106(52):22287–22292, dec 2009.
- [50] Stefan Geissbuehler, Azat Sharipov, Aurélien Godinat, Noelia L. Bocchio, Patrick A. Sandoz, Anja Huss, Nickels A. Jensen, Stefan Jakobs, Jörg Enderlein, F. Gisou Van Der Goot, Elena A. Dubikovskaya, Theo Lasser, and Marcel Leutenegger. Live-cell multiplane three-dimensional super-resolution optical fluctuation imaging. *Nature Communications*, 5(1):1–7, dec 2014.
- [51] Thomas Dertinger, Ryan Colyer, Robert Vogel, Jörg Enderlein, and Shimon Weiss. Achieving increased resolution and more pixels with Superresolution Optical Fluctuation Imaging (SOFI). *Optics Express*, 18(18):18875, aug 2010.

Bibliography

- [52] Stefan Geissbuehler, Noelia L. Bocchio, Claudio Dellagiacoma, Corinne Berclaz, Marcel Leutenegger, and Theo Lasser. Mapping molecular statistics with balanced super-resolution optical fluctuation imaging (bSOFI). *Optical Nanoscopy*, 1(1):1–7, apr 2012.
- [53] Xiyu Yi and Shimon Weiss. Cusp-artifacts in high order superresolution optical fluctuation imaging. *Biomedical Optics Express*, 11(2):554, feb 2020.
- [54] Eran A. Mukamel, Hazen Babcock, and Xiaowei Zhuang. Statistical deconvolution for superresolution fluorescence microscopy. *Biophysical Journal*, 102(10):2391–2400, may 2012.
- [55] Susan Cox, Edward Rosten, James Monypenny, Tijana Jovanovic-Talisman, Dylan T. Burnette, Jennifer Lippincott-Schwartz, Gareth E. Jones, and Rainer Heintzmann. Bayesian localization microscopy reveals nanoscale podosome dynamics. *Nature Methods*, 9(2):195–200, feb 2012.
- [56] Nils Gustafsson, Siân Culley, George Ashdown, Dylan M. Owen, Pedro Matos Pereira, and Ricardo Henriques. Fast live-cell conventional fluorophore nanoscopy with ImageJ through super-resolution radial fluctuations. *Nature Communications*, 7(1):1–9, aug 2016.
- [57] Siân Culley, Kalina L. Tosheva, Pedro Matos Pereira, and Ricardo Henriques. SRRF: Universal live-cell super-resolution microscopy. *International Journal of Biochemistry and Cell Biology*, 101:74–79, aug 2018.
- [58] Kalina L Tosheva, Yue Yuan, Pedro Matos Pereira, Siân Culley, and Ricardo Henriques. Between life and death: strategies to reduce phototoxicity in super-resolution microscopy. *Journal of Physics D: Applied Physics*, 53(16):163001, feb 2020.
- [59] Wei Ouyang, Andrey Aristov, Mickaël Lelek, Xian Hao, and Christophe Zimmer. Deep learning massively accelerates super-resolution localization microscopy. *Nature Biotechnology*, 36(5):460–468, jun 2018.
- [60] Artur Speiser, Lucas Raphael Müller, Ulf Matti, Christopher J. Obara, Wesley R. Legant, Anna Kreshuk, Jakob H. Macke, Jonas Ries, and Srinivas C. Turaga. Deep learning enables fast and dense single-molecule localization with high accuracy. *bioRxiv*, page 2020.10.26.355164, oct 2020.
- [61] Richard J. Marsh, Karin Pfisterer, Pauline Bennett, Liisa M. Hirvonen, Mathias Gautel, Gareth E. Jones, and Susan Cox. Artifact-free high-density localization microscopy analysis. *Nature Methods*, 15(9):689–692, sep 2018.
- [62] Martin Ovesný, Pavel Křížek, Josef Borkovec, Zdeněk Svindrych, and Guy M Hagen. ThunderSTORM: a comprehensive ImageJ plug-in for PALM and STORM data analysis and super-resolution imaging. *Bioinformatics (Oxford, England)*, 30(16):2389–90, aug 2014.

-
- [63] Michela Cosentino, Claudio Canale, Paolo Bianchini, and Alberto Diaspro. AFM-STED correlative nanoscopy reveals a dark side in fluorescence microscopy imaging. *Science Advances*, 5(6):eaav8062, jun 2019.
- [64] L. H. Schaefer, D. Schuster, and J. Schaffer. Structured illumination microscopy: Artefact analysis and reduction utilizing a parameter optimization approach. *Journal of Microscopy*, 216(2):165–174, nov 2004.
- [65] Donna R. Whelan and Toby D.M. Bell. Image artifacts in single molecule localization microscopy: Why optimization of sample preparation protocols matters. *Scientific Reports*, 5(1):1–10, jan 2015.
- [66] G. Binnig and H. Rohrer. Scanning tunneling microscopy. *Surface Science*, 126(1-3):236–244, mar 1983.
- [67] G. Binnig, C. F. Quate, and Ch Gerber. Atomic force microscope. *Physical Review Letters*, 56(9):930–933, mar 1986.
- [68] H. J. Butt, E. K. Wolff, S. A.C. Gould, B. Dixon Northern, C. M. Peterson, and P. K. Hansma. Imaging cells with the atomic force microscope. *Journal of Structural Biology*, 105(1-3):54–61, 1990.
- [69] Noriyuki Kodera, Daisuke Yamamoto, Ryoki Ishikawa, and Toshio Ando. Video imaging of walking myosin v by high-speed atomic force microscopy. *Nature*, 468(7320):72–76, nov 2010.
- [70] Adrian P. Nievergelt, Niccolò Banterle, Santiago H. Andany, Pierre Gönczy, and Georg E. Fantner. High-speed photothermal off-resonance atomic force microscopy reveals assembly routes of centriolar scaffold protein SAS-6. *Nature Nanotechnology*, 13(8):696–701, aug 2018.
- [71] P. K. Hansma, B. Drake, O. Marti, S. A.C. Gould, and C. B. Prater. The scanning ion-conductance microscope. *Science*, 243(4891):641–643, 1989.
- [72] Pavel Novak, Chao Li, Andrew I Shevchuk, Ruben Stepanyan, Matthew Caldwell, Simon Hughes, Trevor G Smart, Julia Gorelik, Victor P Ostanin, Max J Lab, Guy W.J. Moss, Gregory I Frolenkov, David Klenerman, and Yuri E Korchev. Nanoscale live-cell imaging using hopping probe ion conductance microscopy. *Nature Methods*, 6(4):279–281, apr 2009.
- [73] Julia Gorelik, Andrew I. Shevchuk, Gregory I. Frolenkov, Ivan A. Diakonov, Max J. Lab, Corné J. Kros, Guy P. Richardson, Igor Vodyanoy, Christopher R.W. Edwards, David Klenerman, and Yuri E. Korchev. Dynamic assembly of surface structures in living cells. *Proceedings of the National Academy of Sciences of the United States of America*, 100(10):5819–5822, may 2003.

Bibliography

- [74] Andrew I. Shevchuk, Gregory I. Frolenkov, Daniel Sánchez, Peter S. James, Noah Freedman, Max J. Lab, Roy Jones, David Klenerman, and Yuri E. Korchev. Imaging Proteins in Membranes of Living Cells by High-Resolution Scanning Ion Conductance Microscopy. *Angewandte Chemie International Edition*, 45(14):2212–2216, mar 2006.
- [75] Jan Seifert, Johannes Rheinlaender, Pavel Novak, Yuri E. Korchev, and Tilman E. Schäffer. Comparison of Atomic Force Microscopy and Scanning Ion Conductance Microscopy for Live Cell Imaging. *Langmuir*, 31(24):6807–6813, jun 2015.
- [76] Lalita Udpa, Virginia M. Ayres, Yuan Fan, Qian Chen, and Shiva Arun Kumar. Deconvolution of atomic force microscopy data for cellular and molecular imaging. *IEEE Signal Processing Magazine*, 23(3):73–83, 2006.
- [77] Johannes Rheinlaender and Tilman E. Schäffer. Lateral Resolution and Image Formation in Scanning Ion Conductance Microscopy. *Analytical Chemistry*, 87(14):7117–7124, jul 2015.
- [78] Johannes Rheinlaender and Tilman E. Schäffer. An Accurate Model for the Ion Current-Distance Behavior in Scanning Ion Conductance Microscopy Allows for Calibration of Pipet Tip Geometry and Tip-Sample Distance. *Analytical Chemistry*, 89(21):11875–11880, nov 2017.
- [79] Lasse Hyldgaard Klausen, Thomas Fuhs, and Mingdong Dong. Mapping surface charge density of lipid bilayers by quantitative surface conductivity microscopy. *Nature Communications*, 7(1):1–10, aug 2016.
- [80] Jan Seifert, Johannes Rheinlaender, Pavel Novak, Yuri E. Korchev, and Tilman E. Schäffer. Comparison of Atomic Force Microscopy and Scanning Ion Conductance Microscopy for Live Cell Imaging. *Langmuir*, 31(24):6807–6813, jun 2015.
- [81] Supriya V. Bhat, Taranum Sultana, André Körnig, Seamus McGrath, Zinnat Shahina, and Tanya E.S. Dahms. Correlative atomic force microscopy quantitative imaging-laser scanning confocal microscopy quantifies the impact of stressors on live cells in real-time. *Scientific Reports*, 8(1):1–10, dec 2018.
- [82] Ana I. Gómez-Varela, Dimitar R. Stamov, Adelaide Miranda, Rosana Alves, Cláudia Barata-Antunes, Daphné Dambournet, David G. Drubin, Sandra Paiva, and Pieter A.A. De Beule. Simultaneous co-localized super-resolution fluorescence microscopy and atomic force microscopy: combined SIM and AFM platform for the life sciences. *Scientific Reports*, 10(1):1–10, dec 2020.
- [83] Liisa M. Hirvonen and Susan Cox. STORM without enzymatic oxygen scavenging for correlative atomic force and fluorescence superresolution microscopy. *Methods and Applications in Fluorescence*, 6(4):045002, jul 2018.

- [84] Liisa M. Hirvonen, Richard J. Marsh, Gareth E. Jones, and Susan Cox. Combined AFM and super-resolution localisation microscopy: Investigating the structure and dynamics of podosomes. *European Journal of Cell Biology*, 99(7):151106, sep 2020.
- [85] Pascal D. Odermatt, Arun Shivanandan, Hendrik Deschout, Radek Jankele, Adrian P. Nievergelt, Lely Feletti, Michael W. Davidson, Aleksandra Radenovic, and Georg E. Fantner. High-Resolution Correlative Microscopy: Bridging the Gap between Single Molecule Localization Microscopy and Atomic Force Microscopy. *Nano Letters*, 15(8):4896–4904, aug 2015.
- [86] Tayyibah Ali, Joanna Bednarska, Stéphane Vassilopoulos, Martin Tran, Ivan A. Diakonov, Azza Ziyadeh-Isleem, Pascale Guicheney, Julia Gorelik, Yuri E. Korchev, Mary M. Reilly, Marc Bitoun, and Andrew Shevchuk. Correlative SICM-FCM reveals changes in morphology and kinetics of endocytic pits induced by disease-associated mutations in dynamin. *FASEB Journal*, 33(7):8504–8518, jul 2019.
- [87] Philipp Hagemann, Astrid Gesper, and Patrick Happel. Correlative Stimulated Emission Depletion and Scanning Ion Conductance Microscopy. *ACS Nano*, 12(6):5807–5815, jun 2018.
- [88] W H Couter. Means for counting particles suspended in a fluid, aug 1953.
- [89] James Clarke, Hai Chen Wu, Lakmal Jayasinghe, Alpesh Patel, Stuart Reid, and Hagan Bayley. Continuous base identification for single-molecule nanopore DNA sequencing. *Nature Nanotechnology*, 4(4):265–270, feb 2009.
- [90] Tom Z. Butler, Mikhail Pavlenok, Ian M. Derrington, Michael Niederweis, and Jens H. Gundlach. Single-molecule DNA detection with an engineered MspA protein nanopore. *Proceedings of the National Academy of Sciences of the United States of America*, 105(52):20647–20652, dec 2008.
- [91] Jiandong Feng, Ke Liu, Roman D. Bulushev, Sergey Khlybov, Dumitru Dumcenco, Andras Kis, and Aleksandra Radenovic. Identification of single nucleotides in MoS₂ nanopores. *Nature Nanotechnology*, 10(12):1070–1076, dec 2015.
- [92] Lorenz J. Steinbock, Roman D. Bulushev, Swati Krishnan, Camille Raillon, and Aleksandra Radenovic. DNA translocation through low-noise glass nanopores. *ACS Nano*, 7(12):11255–11262, dec 2013.
- [93] Min Hyun Lee, Ashvani Kumar, Kyeong Beom Park, Seong Yong Cho, Hyun Mi Kim, Min Cheol Lim, Young Rok Kim, and Ki Bum Kim. A low-noise solid-state nanopore platform based on a highly insulating substrate. *Scientific Reports*, 4(1):1–7, dec 2014.
- [94] Nicholas A.W. Bell and Ulrich F. Keyser. Digitally encoded DNA nanostructures for multiplexed, single-molecule protein sensing with nanopores. *Nature Nanotechnology*, 11(7):645–651, jul 2016.

Bibliography

- [95] Roman D. Bulushev, Sanjin Marion, Ekaterina Petrova, Sebastian J. Davis, Sebastian J. Maerkl, and Aleksandra Radenovic. Single Molecule Localization and Discrimination of DNA–Protein Complexes by Controlled Translocation Through Nanocapillaries. *Nano Letters*, 16(12):7882–7890, dec 2016.
- [96] Kaikai Chen, Jinglin Kong, Jinbo Zhu, Niklas Ermann, Paul Predki, and Ulrich F. Keyser. Digital Data Storage Using DNA Nanostructures and Solid-State Nanopores. *Nano Letters*, 2019.
- [97] Zhishan Yuan, Youming Liu, Min Dai, Xin Yi, and Chengyong Wang. Controlling DNA Translocation Through Solid-state Nanopores. *Nanoscale Research Letters*, 15(1), 2020.
- [98] Thomas D. Pollard. Cell motility and cytokinesis: From mysteries to molecular mechanisms in five decades, oct 2019.
- [99] Alejandro Sánchez Alvarado and Shinya Yamanaka. Rethinking differentiation: Stem cells, regeneration, and plasticity, mar 2014.
- [100] Merran C. Derby and Paul A. Gleeson. New Insights into Membrane Trafficking and Protein Sorting, 2007.
- [101] Bruce Alberts, Alexander Johnson, Julian Lewis, Martin Raff, Keith Roberts, and Peter Walter. *General Principles of Cell Communication*. Garland Science, 2002.
- [102] N. Ban, P. Nissen, J. Hansen, P. B. Moore, and T. A. Steitz. The complete atomic structure of the large ribosomal subunit at 2.4 Å resolution. *Science*, 289(5481):905–920, aug 2000.
- [103] Qianglin Fang, Dongjie Zhu, Irina Agarkova, Jagat Adhikari, Thomas Klose, Yue Liu, Zhenguo Chen, Yingyuan Sun, Michael L. Gross, James L. Van Etten, Xinzhen Zhang, and Michael G. Rossmann. Near-atomic structure of a giant virus. *Nature Communications*, 10(1):1–11, dec 2019.
- [104] Tanmay A.M. Bharat and Wanda Kukulski. Cryo-Correlative Light and Electron Microscopy. In *Correlative Imaging*, pages 137–153. Wiley, oct 2019.
- [105] Josef Neumüller. Electron tomography—a tool for ultrastructural 3D visualization in cell biology and histology. *Wiener Medizinische Wochenschrift*, 168(11-12):322–329, sep 2018.
- [106] Steffen J Sahl, Stefan W Hell, and Stefan Jakobs. Fluorescence nanoscopy in cell biology. *Nature Publishing Group*, 18, 2017.
- [107] Sina Waldchen, Julian Lehmann, Teresa Klein, Sebastian Van De Linde, and Markus Sauer. Light-induced cell damage in live-cell super-resolution microscopy. *Scientific Reports*, 5, oct 2015.

-
- [108] T Dertinger, R Colyer, G Iyer, S Weiss, and J Enderlein. Fast, background-free, 3D super-resolution optical fluctuation imaging (SOFI). *Proceedings of the National Academy of Sciences of the United States of America*, 106(52):22287–92, dec 2009.
- [109] Stefan Geissbuehler, Claudio Dellagiacoma, and Theo Lasser. Comparison between SOFI and STORM. *Biomedical Optics Express*, 2(3):408, mar 2011.
- [110] Stefan Geissbuehler, Azat Sharipov, Aurélien Godinat, Noelia L. Bocchio, Patrick A. Sandoz, Anja Huss, Nickels A. Jensen, Stefan Jakobs, Jörg Enderlein, F. Gisou van der Goot, Elena A. Dubikovskaya, Theo Lasser, and Marcel Leutenegger. Live-cell multiplane three-dimensional super-resolution optical fluctuation imaging. *Nature Communications*, 5:5830, dec 2014.
- [111] Mikihiro Shibata, Hiroki Watanabe, Takayuki Uchihashi, Toshio Ando, and Ryohei Yasuda. High-speed atomic force microscopy imaging of live mammalian cells. *Biophysics and Physicobiology*, 14(0):127–135, 2017.
- [112] Susana Moreno Flores and José L. Toca-Herrera. The new future of scanning probe microscopy: Combining atomic force microscopy with other surface-sensitive techniques, optical microscopy and fluorescence techniques. *Nanoscale*, 1(1):40–49, sep 2009.
- [113] Michael Krieg, Gotthold Fläschner, David Alsteens, Benjamin M. Gaub, Wouter H. Roos, Gijs J.L. Wuite, Hermann E. Gaub, Christoph Gerber, Yves F. Dufrêne, and Daniel J. Müller. Atomic force microscopy-based mechanobiology, jan 2019.
- [114] Patrick L.T.M. Frederix, Patrick D. Bosshart, and Andreas Engel. Atomic force microscopy of biological membranes, jan 2009.
- [115] Adrian P. Nievergelt, Niccolò Banterle, Santiago H. Andany, Pierre Gönczy, and Georg E. Fantner. High-speed photothermal off-resonance atomic force microscopy reveals assembly routes of centriolar scaffold protein SAS-6, aug 2018.
- [116] Pascal D. Odermatt, Arun Shivanandan, Hendrik Deschout, Radek Jankele, Adrian P. Nievergelt, Lely Feletti, Michael W. Davidson, Aleksandra Radenovic, and Georg E. Fantner. High-Resolution Correlative Microscopy: Bridging the Gap between Single Molecule Localization Microscopy and Atomic Force Microscopy. *Nano Letters*, 15(8):4896–4904, aug 2015.
- [117] Johannes Rheinlaender and Tilman E. Schäffer. Image formation, resolution, and height measurement in scanning ion conductance microscopy. *Journal of Applied Physics*, 105(9), 2009.
- [118] A. Descloux, K. S. Grusmayer, E. Bostan, T. Lukes, A. Bouwens, A. Sharipov, S. Geissbuehler, A. L. Mahul-Mellier, H. A. Lashuel, M. Leutenegger, and T. Lasser. Combined multi-plane phase retrieval and super-resolution optical fluctuation imaging for 4D cell microscopy. *Nature Photonics*, 12(3):165–172, mar 2018.

Bibliography

- [119] L. J. Steinbock, J. F. Steinbock, and A. Radenovic. Controllable shrinking and shaping of glass nanocapillaries under electron irradiation. *Nano Letters*, 13(4):1717–1723, apr 2013.
- [120] Hendrik Deschout, Tomas Lukes, Azat Sharipov, Daniel Szlag, Lely Feletti, Wim Vandenberg, Peter Dedecker, Johan Hofkens, Marcel Leutenegger, Theo Lasser, and Aleksandra Radenovic. Complementarity of PALM and SOFI for super-resolution live-cell imaging of focal adhesions. *Nature Communications*, 7(1):1–11, dec 2016.
- [121] Philipp Werther, Klaus Yserentant, Felix Braun, Nicolai Kaltwasser, Christoph Popp, Mathis Baalmann, Dirk-Peter Hertzen, and Richard Wombacher. Live-Cell Localization Microscopy with a Fluorogenic and Self-Blinking Tetrazine Probe. *Angewandte Chemie International Edition*, 59(2):804–810, jan 2020.
- [122] Eric Henderson and Donald S. Sakaguchi. Imaging F-actin in fixed glial cells with a combined optical fluorescence/atomic force microscope. *NeuroImage*, 1(2):145–150, sep 1993.
- [123] T. Berdyeva, C. D. Woodworth, and I. Sokolov. Visualization of cytoskeletal elements by the atomic force microscope. *Ultramicroscopy*, 102(3):189–198, feb 2005.
- [124] Aya Tanaka, Ryosuke Tanaka, Nahoko Kasai, Shingo Tsukada, Takaharu Okajima, and Koji Sumitomo. Time-lapse imaging of morphological changes in a single neuron during the early stages of apoptosis using scanning ion conductance microscopy. *Journal of Structural Biology*, 191(1):32–38, jul 2015.
- [125] J Gorelik, A Shevchuk, M Ramalho, M Elliott, C Lei, C F Higgins, Max J Lab, D Klenerman, N Krauzewicz, and Y Korchev. Scanning surface confocal microscopy for simultaneous topographical and fluorescence imaging: application to single virus-like particle entry into a cell. *Proceedings of the National Academy of Sciences of the United States of America*, 99(25):16018–23, dec 2002.
- [126] Andrew I. Shevchuk, Phil Hobson, Max J. Lab, David Klenerman, Nina Krauzewicz, and Yuri E. Korchev. Imaging single virus particles on the surface of cell membranes by high-resolution scanning surface confocal microscopy. *Biophysical Journal*, 94(10):4089–4094, may 2008.
- [127] Ricardo Garcia. Nanomechanical mapping of soft materials with the atomic force microscope: methods, theory and applications. *Chemical Society Reviews*, 49(16):5850–5884, aug 2020.
- [128] Peter Hinterdorfer and Yves F. Dufrêne. Detection and localization of single molecular recognition events using atomic force microscopy, may 2006.
- [129] Kenneth M. Yamada and Michael Sixt. Mechanisms of 3D cell migration, dec 2019.

-
- [130] Joanna Bednarska, Annegret Pelchen-Matthews, Pavel Novak, Jemima J. Burden, Peter A. Summers, Marina K. Kuimova, Yuri Korchev, Mark Marsh, and Andrew Shevchuk. Rapid formation of human immunodeficiency virus-like particles. *Proceedings of the National Academy of Sciences of the United States of America*, 117(35):21637–21646, sep 2020.
- [131] Ludger Johannes, Weria Pezeshkian, John H. Ipsen, and Julian C. Shillcock. Clustering on Membranes: Fluctuations and More, may 2018.
- [132] Semen O. Yesylevskyy, Timothée Rivel, and Christophe Ramseyer. The influence of curvature on the properties of the plasma membrane. Insights from atomistic molecular dynamics simulations. *Scientific Reports*, 7(1):1–13, dec 2017.
- [133] Erdinc Sezgin, Ilya Levental, Satyajit Mayor, and Christian Eggeling. The mystery of membrane organization: Composition, regulation and roles of lipid rafts, jun 2017.
- [134] Martin Heine, Anna Ciuraszkiewicz, Andreas Voigt, Jennifer Heck, and Arthur Bikbaev. Surface dynamics of voltage-gated ion channels, jul 2016.
- [135] Joran Deschamps, Andreas Rowald, and Jonas Ries. Efficient homogeneous illumination and optical sectioning for quantitative single-molecule localization microscopy. *Optics Express*, 24(24):28080, nov 2016.
- [136] Vytautas Navikas, Samuel Mendes Leitao, Sanjin Marion, Sebastian James Davis, Barney Drake, Georg E. Fantner, and Aleksandra Radenovic. High-Throughput, Nanocapillary Filling Method Based on Microwave Radiation. *ACS Applied Nano Materials*, page aacsanm.0c01345, jul 2020.
- [137] David Nečas and Petr Klapetek. Gwyddion: an open-source software for SPM data analysis. *Open Physics*, 10(1):181–188, 2012.
- [138] Johannes Schindelin, Ignacio Arganda-Carreras, Erwin Frise, Verena Kaynig, Mark Longair, Tobias Pietzsch, Stephan Preibisch, Curtis Rueden, Stephan Saalfeld, Benjamin Schmid, Jean Yves Tinevez, Daniel James White, Volker Hartenstein, Kevin Eliceiri, Pavel Tomancak, and Albert Cardona. Fiji: An open-source platform for biological-image analysis. *Nature Methods*, 9(7):676–682, jul 2012.
- [139] Samuel M Leitao, Barney Drake, Katarina Pinjusic, Xavier Pierrat, Vytautas Navikas, Adrian P Nievergelt, Charlène Brillard, Denis Djekic, Aleksandra Radenovic, Alex Persat, Daniel B Constam, Jens Anders, and E Fantner. Time-resolved scanning ion conductance microscopy for three-dimensional tracking of nanoscale cell surface dynamics 2. *bioRxiv*, page 2021.05.13.444009, may 2021.
- [140] Lothar Schermelleh, Alexia Ferrand, Thomas Huser, Christian Eggeling, Markus Sauer, Oliver Biehlmaier, and Gregor P.C. Drummen. Super-resolution microscopy demystified, jan 2019.

Bibliography

- [141] Fan Xu, Donghan Ma, Kathryn P. MacPherson, Sheng Liu, Ye Bu, Yu Wang, Yu Tang, Cheng Bi, Tim Kwok, Alexander A. Chubykin, Peng Yin, Sarah Calve, Gary E. Landreth, and Fang Huang. Three-dimensional nanoscopy of whole cells and tissues with in situ point spread function retrieval. *Nature Methods*, 17(5):531–540, may 2020.
- [142] Ignacio Izeddin, Mohamed El Beheiry, Jordi Andilla, Daniel Ciepielewski, Xavier Darzacq, and Maxime Dahan. PSF shaping using adaptive optics for three-dimensional single-molecule super-resolution imaging and tracking. *Optics Express*, 20(5):4957, feb 2012.
- [143] Andrey Aristov, Benoit Lelandais, Elena Rensen, and Christophe Zimmer. ZOLA-3D allows flexible 3D localization microscopy over an adjustable axial range. *Nature Communications*, 9(1):1–8, dec 2018.
- [144] Ulrike Böhm, Stefan W. Hell, and Roman Schmidt. 4Pi-RESOLFT nanoscopy. *Nature Communications*, 7(1):1–8, feb 2016.
- [145] Thomas A. Planchon, Liang Gao, Daniel E. Milkie, Michael W. Davidson, James A. Galbraith, Catherine G. Galbraith, and Eric Betzig. Rapid three-dimensional isotropic imaging of living cells using Bessel beam plane illumination. *Nature Methods*, 8(5):417–423, may 2011.
- [146] Chieh Han Lu, Wei Chun Tang, Yen Ting Liu, Shu Wei Chang, Frances Camille M. Wu, Chin Yi Chen, Yun Chi Tsai, Shun Min Yang, Chiung Wen Kuo, Yasushi Okada, Yeu Kuang Hwu, Peilin Chen, and Bi Chang Chen. Lightsheet localization microscopy enables fast, large-scale, and three-dimensional super-resolution imaging. *Communications Biology*, 2(1):1–10, dec 2019.
- [147] Sara Abrahamsson, Jiji Chen, Bassam Hajj, Sjoerd Stallinga, Alexander Y. Katsov, Jan Wisniewski, Gaku Mizuguchi, Pierre Soule, Florian Mueller, Claire Dugast Darzacq, Xavier Darzacq, Carl Wu, Cornelia I. Bargmann, David A. Agard, Maxime Dahan, and Mats G.L. Gustafsson. Fast multicolor 3D imaging using aberration-corrected multifocus microscopy. *Nature Methods*, 10(1):60–63, jan 2013.
- [148] Laura Oudjedi, Jean-Bernard Fiche, Sara Abrahamsson, Laurent Mazonq, Aurélie Lecestre, Pierre-François Calmon, Aline Cerf, and Marcelo Nöhlmann. Astigmatic multifocus microscopy enables deep 3D super-resolved imaging. *Biomedical Optics Express*, 7(6):2163, jun 2016.
- [149] David P. Hoffman, Gleb Shtengel, C. Shan Xu, Kirby R. Campbell, Melanie Freeman, Lei Wang, Daniel E. Milkie, H. Amalia Pasolli, Nirmala Iyer, John A. Bogovic, Daniel R. Stabley, Abbas Shirinifard, Song Pang, David Peale, Kathy Schaefer, Wim Pomp, Chi Lun Chang, Jennifer Lippincott-Schwartz, Tom Kirchhausen, David J. Solecki, Eric Betzig, and Harald F. Hess. Correlative three-dimensional super-resolution and block-face electron microscopy of whole vitreously frozen cells. *Science*, 367(6475), jan 2020.

-
- [150] Paolo Annibale, Marco Scarselli, Mattia Greco, and Aleksandra Radenovic. Identification of the factors affecting co-localization precision for quantitative multicolor localization microscopy. *Optical Nanoscopy*, 1(1):1–13, nov 2012.
- [151] Ryan McGorty, Daichi Kamiyama, and Bo Huang. Active microscope stabilization in three dimensions using image correlation. *Optical Nanoscopy*, 2(1), 2013.
- [152] Simao Coelho, Jongho Baek, James Walsh, J. Justin Gooding, and Katharina Gaus. 3D active stabilization for single-molecule imaging. *Nature Protocols*, 16(1):497–515, jan 2021.
- [153] M. Bathe-Peters, P. Annibale, and M. J. Lohse. All-optical microscope autofocus based on an electrically tunable lens and a totally internally reflected IR laser. *Optics Express*, 26(3):2359, feb 2018.
- [154] Mantas Žurauskas, Oliver Barnstedt, Maria Frade-Rodriguez, Scott Waddell, and Martin J. Booth. Rapid adaptive remote focusing microscope for sensing of volumetric neural activity. *Biomedical Optics Express*, 8(10):4369, oct 2017.
- [155] Mariano Bossi, Jonas Föiling, Vladimir N. Belov, Vadim P. Boyarskiy, Rebecca Medda, Alexander Egner, Christian Eggeling, Andreas Schönle, and Stefan W. Hell. Multicolor far-field fluorescence nanoscopy through isolated detection of distinct molecular species. *Nano Letters*, 8(8):2463–2468, aug 2008.
- [156] Remi Galland, Gianluca Greci, Ajay Aravind, Virgile Viasnoff, Vincent Studer, and Jean Baptiste Sibarita. 3D high- and super-resolution imaging using single-objective SPIM. *Nature Methods*, 12(7):641–644, jun 2015.
- [157] Marijn E. Siemons, Naomi A.K. Hanemaaijer, Maarten H.P. Kole, and Lukas C. Kapitein. REALM: AO-based localization microscopy deep in complex tissue, jun 2020.
- [158] Graham T Dempsey, Joshua C Vaughan, Kok Hao Chen, Mark Bates, and Xiaowei Zhuang. evaluation of fluorophores for optimal performance in localization-based super-resolution imaging. *Analysis Nature methods*, 8(12), 2011.
- [159] Ben Ewell Urban, Lei Xiao, Siyu Chen, Huili Yang, Biqin Dong, Yevgenia Kozorovitskiy, and Hao F. Zhang. In vivo superresolution imaging of neuronal structure in the mouse brain. *IEEE Transactions on Biomedical Engineering*, 65(1):232–238, jan 2018.
- [160] Joerg Schnitzbauer, Maximilian T. Strauss, Thomas Schlichthaerle, Florian Schueder, and Ralf Jungmann. Super-resolution microscopy with DNA-PAINT. *Nature Protocols*, 12(6):1198–1228, jun 2017.
- [161] Ralf Jungmann, Maier S. Avendaño, Johannes B. Woehrstein, Mingjie Dai, William M. Shih, and Peng Yin. Multiplexed 3D cellular super-resolution imaging with DNA-PAINT and Exchange-PAINT. *Nature Methods*, 11(3):313–318, feb 2014.

Bibliography

- [162] Jeongmin Kim, Michal Wojcik, Yuan Wang, Seonah Moon, Emilia A. Zin, Nadia Marnani, Zachary L. Newman, John G. Flannery, Ke Xu, and Xiang Zhang. Oblique-plane single-molecule localization microscopy for tissues and small intact animals. *Nature Methods*, 16(9):853–857, sep 2019.
- [163] Hendrik Deschout, Tomas Lukes, Azat Sharipov, Daniel Szlag, Lely Feletti, Wim Vandenberg, Peter Dedecker, Johan Hofkens, Marcel Leutenegger, Theo Lasser, and Aleksandra Radenovic. Complementarity of PALM and SOFI for super-resolution live-cell imaging of focal adhesions. *Nature communications*, 7:13693, dec 2016.
- [164] Martin J. Booth, Mark A.A. Neil, Rimas Juškaitis, and Tony Wilson. Adaptive aberration correction in a confocal microscope. *Proceedings of the National Academy of Sciences of the United States of America*, 99(9):5788–5792, apr 2002.
- [165] V. FRAISIER, G. CLOUVEL, A. JASAITIS, A. DIMITROV, T. PIOLOT, and J. SALAMERO. Adaptive optics in spinning disk microscopy: improved contrast and brightness by a simple and fast method. *Journal of Microscopy*, 259(3):219–227, sep 2015.
- [166] Xuanze Chen, Zhiping Zeng, Rongqin Li, Boxin Xue, Peng Xi, and Yujie Sun. Superior performance with sCMOS over EMCCD in super-resolution optical fluctuation imaging. *Journal of Biomedical Optics*, 21(6):066007, jun 2016.
- [167] Cees Dekker. Solid-state nanopores, mar 2007.
- [168] Tim Albrecht. Single-Molecule Analysis with Solid-State Nanopores. *Annual Review of Analytical Chemistry*, 12(1):371–387, jun 2019.
- [169] Ralph M.M. Smeets, Ulrich F. Keyser, Diego Krapf, Meng Yue Wu, Nynke H. Dekker, and Cees Dekker. Salt dependence of ion transport and DMA translocation through solid-state nanopores. *Nano Letters*, 6(1):89–95, jan 2006.
- [170] Nicolas Di Fiori, Allison Squires, Daniel Bar, Tal Gilboa, Theodore D. Moustakas, and Amit Meller. Optoelectronic control of surface charge and translocation dynamics in solid-state nanopores. *Nature Nanotechnology*, 8(12):946–951, nov 2013.
- [171] Ke Liu, Martina Lihter, Aditya Sarathy, Sabina Caneva, Hu Qiu, Davide Deiana, Vasiliki Tileli, Duncan T.L. Alexander, Stephan Hofmann, Dumitru Dumcenco, Andras Kis, Jean Pierre Leburton, and Aleksandra Radenovic. Geometrical Effect in 2D Nanopores. *Nano Letters*, 17(7):4223–4230, jul 2017.
- [172] Mounir Tarek. Membrane electroporation: A molecular dynamics simulation. *Biophysical Journal*, 88(6):4045–4053, jun 2005.
- [173] Alessio Fragasso, Sonja Schmid, and Cees Dekker. Comparing Current Noise in Biological and Solid-State Nanopores, feb 2020.

-
- [174] Wenhong Li, Nicholas A.W. Bell, Silvia Hernández-Ainsa, Vivek V. Thacker, Alana M. Thackray, Raymond Bujdoso, and Ulrich F. Keyser. Single protein molecule detection by glass nanopores. *ACS Nano*, 7(5):4129–4134, may 2013.
- [175] Lorenz J. Steinbock, Oliver Otto, Catalin Chimerele, Joanne Gornall, and Ulrich F. Keyser. Detecting DNA folding with nanocapillaries. *Nano Letters*, 10(7):2493–2497, jul 2010.
- [176] Roman D. Bulushev, Sanjin Marion, Ekaterina Petrova, Sebastian J. Davis, Sebastian J. Maerkl, and Aleksandra Radenovic. Single Molecule Localization and Discrimination of DNA-Protein Complexes by Controlled Translocation Through Nanocapillaries. *Nano Letters*, 16(12):7882–7890, dec 2016.
- [177] Lasse Hyldgaard Klausen, Thomas Fuhs, and Mingdong Dong. Mapping surface charge density of lipid bilayers by quantitative surface conductivity microscopy. *Nature Communications*, 7(1):1–10, aug 2016.
- [178] Johannes Rheinlaender and Tilman E. Schäffer. Mapping the mechanical stiffness of live cells with the scanning ion conductance microscope. *Soft Matter*, 9(12):3230–3236, mar 2013.
- [179] Jung Min Oh, Telli Faez, Sissi De Beer, and Frieder Mugele. Capillarity-driven dynamics of water-alcohol mixtures in nanofluidic channels. *Microfluidics and Nanofluidics*, 9(1):123–129, jul 2010.
- [180] Sanjin Marion, Michal Macha, Sebastian J. Davis, Andrey Chernev, and Aleksandra Radenovic. Wetting of nanopores probed with pressure. *arXiv*, 1911.05229, oct 2019.
- [181] Evelyne Salançon and Bernard Tinland. Filling nanopipettes with apertures smaller than 50 nm: dynamic microdistillation. *Beilstein Journal of Nanotechnology*, 9:2181–2187, aug 2018.
- [182] Rui Gao, Yao Lin, Yi Lun Ying, Yong Xu Hu, Su Wen Xu, Lin Qi Ruan, Ru Jia Yu, Yuan Jie Li, Hao Wen Li, Ling Fei Cui, and Yi Tao Long. Wireless nanopore electrodes for analysis of single entities. *Nature Protocols*, 14(7):2015–2035, jul 2019.
- [183] Linhao Sun, Kazuki Shigyou, Toshio Ando, and Shinji Watanabe. Thermally Driven Approach To Fill Sub-10-nm Pipettes with Batch Production. *Analytical Chemistry*, 91(21):14080–14084, nov 2019.
- [184] David R. Baghurst and D. Michael P. Mingos. Superheating effects associated with microwave dielectric heating. *Journal of the Chemical Society, Chemical Communications*, (9):674–677, jan 1992.
- [185] Satoshi Horikoshi, Shohei Matsuzaki, Shintaro Sakamoto, and Nick Serpone. Efficient degassing of dissolved oxygen in aqueous media by microwave irradiation and the effect of microwaves on a reaction catalyzed by Wilkinson’s catalyst. *Radiation Physics and Chemistry*, 97:48–55, apr 2014.

Bibliography

- [186] Lorenz J. Steinbock, Roman D. Bulushev, Swati Krishnan, Camille Raillon, and Aleksandra Radenovic. DNA translocation through low-noise glass nanopores. *ACS Nano*, 7(12):11255–11262, dec 2013.
- [187] Michelle L. Kovarik, Kaimeng Zhou, and Stephen C. Jacobson. Effect of conical nanopore diameter on ion current rectification. *Journal of Physical Chemistry B*, 113(49):15960–15966, dec 2009.
- [188] Jan Seifert, Johannes Rheinlaender, Pavel Novak, Yuri E. Korchev, and Tilman E. Schäffer. Comparison of Atomic Force Microscopy and Scanning Ion Conductance Microscopy for Live Cell Imaging. *Langmuir*, 31(24):6807–6813, jun 2015.
- [189] Kerstin Göpflich, Chandrashekhara V. Kulkarni, Oliver J. Pambos, and Ulrich F. Keyser. Lipid nanobilayers to host biological nanopores for DNA translocations. *Langmuir*, 29(1):355–364, jan 2013.
- [190] John J. Kasianowicz, Eric Brandin, Daniel Branton, and David W. Deamer. Characterization of individual polynucleotide molecules using a membrane channel. *Proceedings of the National Academy of Sciences of the United States of America*, 93(24):13770–13773, nov 1996.
- [191] Elizabeth A. Manrao, Ian M. Derrington, Andrew H. Laszlo, Kyle W. Langford, Matthew K. Hopper, Nathaniel Gillgren, Mikhail Pavlenok, Michael Niederweis, and Jens H. Gundlach. Reading DNA at single-nucleotide resolution with a mutant MspA nanopore and phi29 DNA polymerase. *Nature Biotechnology*, 30(4):349–353, apr 2012.
- [192] Jiali Li, Derek Stein, Ciaran McMullan, Daniel Branton, Michael J. Aziz, and Jene A. Golovchenko. Ion-beam sculpting at nanometre length scales. *Nature*, 412(6843):166–169, jul 2001.
- [193] Jiali Li, Marc Gershow, Derek Stein, Eric Brandin, and J. A. Golovchenko. DNA molecules and configurations in a solid-state nanopore microscope. *Nature Materials*, 2(9):611–615, aug 2003.
- [194] L. J. Steinbock, J. F. Steinbock, and A. Radenovic. Controllable shrinking and shaping of glass nanocapillaries under electron irradiation. *Nano Letters*, 13(4):1717–1723, apr 2013.
- [195] Bala Murali Venkatesan, Brian Dorvel, Sukru Yemenicioglu, Nicholas Watkins, Ivan Petrov, and Rashid Bashir. Highly Sensitive, Mechanically Stable Nanopore Sensors for DNA Analysis. *Advanced Materials*, 21(27):2771–2776, jul 2009.
- [196] Grégory F. Schneider, Stefan W. Kowalczyk, Victor E. Calado, Grégory Pandraud, Henny W. Zandbergen, Lieven M.K. Vandersypen, and Cees Dekker. DNA translocation through graphene nanopores. *Nano Letters*, 10(8):3163–3167, aug 2010.

-
- [197] Jiandong Feng, Ke Liu, Roman D. Bulushev, Sergey Khlybov, Dumitru Dumcenco, Andras Kis, and Aleksandra Radenovic. Identification of single nucleotides in MoS₂ nanopores. *Nature Nanotechnology*, 10(12):1070–1076, dec 2015.
- [198] Zhi Zhou, Ying Hu, Hao Wang, Zhi Xu, Wenlong Wang, Xuedong Bai, Xinyan Shan, and Xinghua Lu. DNA Translocation through hydrophilic nanopore in hexagonal boron nitride. *Scientific Reports*, 3(1):1–5, nov 2013.
- [199] Michal Macha, Sanjin Marion, Vishal V.R. Nandigana, and Aleksandra Radenovic. 2D materials as an emerging platform for nanopore-based power generation. *Nature Reviews Materials*, 4(9):588–605, sep 2019.
- [200] Elizabeth A. Manrao, Ian M. Derrington, Andrew H. Laszlo, Kyle W. Langford, Matthew K. Hopper, Nathaniel Gillgren, Mikhail Pavlenok, Michael Niederweis, and Jens H. Gundlach. Reading DNA at single-nucleotide resolution with a mutant MspA nanopore and phi29 DNA polymerase. *Nature Biotechnology*, 30(4):349–353, apr 2012.
- [201] Michael Graf, Martina Lihter, Mukeshchand Thakur, Vasileia Georgiou, Juraj Topolancik, B. Robert Ilic, Ke Liu, Jiandong Feng, Yann Astier, and Aleksandra Radenovic. Fabrication and practical applications of molybdenum disulfide nanopores. *Nature Protocols*, 14(4):1130–1168, apr 2019.
- [202] Erwin Neher and Bert Sakmann. Single-channel currents recorded from membrane of denervated frog muscle fibres. *Nature*, 260(5554):799–802, apr 1976.
- [203] Lorenz J. Steinbock, Roman D. Bulushev, Swati Krishnan, Camille Raillon, and Aleksandra Radenovic. DNA translocation through low-noise glass nanopores. *ACS Nano*, 7(12):11255–11262, dec 2013.
- [204] Wenhong Li, Nicholas A.W. Bell, Silvia Hernández-Ainsa, Vivek V. Thacker, Alana M. Thackray, Raymond Bujdoso, and Ulrich F. Keyser. Single protein molecule detection by glass nanopores. *ACS Nano*, 7(5):4129–4134, may 2013.
- [205] Xiaolong Xu, Chuanping Li, Ya Zhou, and Yongdong Jin. Controllable Shrinking of Glass Capillary Nanopores Down to sub-10 nm by Wet-Chemical Silanization for Signal-Enhanced DNA Translocation. *ACS Sensors*, 2(10):1452–1457, oct 2017.
- [206] Edward M. Nelson, Hui Li, and Gregory Timp. Direct, concurrent measurements of the forces and currents affecting DNA in a nanopore with comparable topography. *ACS Nano*, 8(6):5484–5493, jun 2014.
- [207] Ulrich F. Keyser, Bernard N. Koeleman, Stijn Van Dorp, Diego Krapf, Ralph M.M. Smeets, Serge G. Lemay, Nynke H. Dekker, and Cees Dekker. Direct force measurements on DNA in a solid-state nanopore. *Nature Physics*, 2(7):473–477, jul 2006.
- [208] Hongbo Peng and Xinsheng Sean Ling. Reverse DNA translocation through a solid-state nanopore by magnetic tweezers. *Nanotechnology*, 20(18):8, apr 2009.

Bibliography

- [209] Changbae Hyun, Harpreet Kaur, Ryan Rollings, Min Xiao, and Jiali Li. Threading immobilized DNA molecules through a solid-state nanopore at $>100\ \mu\text{s}$ per base rate. *ACS Nano*, 7(7):5892–5900, jul 2013.
- [210] Morteza Aramesh, Csaba Forró, Livie Dorwling-Carter, Ines Lüchtfeld, Tilman Schlotter, Stephan J. Ihle, Ivan Shorubalko, Vahid Hosseini, Dmitry Momotenko, Tomaso Zambelli, Enrico Klotzsch, and János Vörös. Localized detection of ions and biomolecules with a force-controlled scanning nanopore microscope. *Nature Nanotechnology*, 14(8):791–798, aug 2019.
- [211] Nicholas A.W. Bell, Kaikai Chen, Sandip Ghosal, Maria Ricci, and Ulrich F. Keyser. Asymmetric dynamics of DNA entering and exiting a strongly confining nanopore. *Nature Communications*, 8(1):1–8, dec 2017.
- [212] Roman D. Bulushev, Lorenz J. Steinbock, Sergey Khlybov, Julian F. Steinbock, Ulrich F. Keyser, and Aleksandra Radenovic. Measurement of the Position-Dependent Electrophoretic Force on DNA in a Glass Nanocapillary. *Nano Letters*, 14(11):6606–6613, nov 2014.
- [213] Nicholas A.W. Bell, Kaikai Chen, Sandip Ghosal, Maria Ricci, and Ulrich F. Keyser. Asymmetric dynamics of DNA entering and exiting a strongly confining nanopore. *Nature Communications*, 8(1):1–8, dec 2017.
- [214] Mikihiro Shibata, Hiroshi Nishimasu, Noriyuki Kodera, Seiichi Hirano, Toshio Ando, Takayuki Uchihashi, and Osamu Nureki. Real-space and real-Time dynamics of CRISPR-Cas9 visualized by high-speed atomic force microscopy. *Nature Communications*, 8(1):1–9, dec 2017.
- [215] Xu Liu, Philip Zimny, Yuning Zhang, Ankit Rana, Roland Nagel, Walter Reisner, and William B. Dunbar. Flossing DNA in a Dual Nanopore Device. *Small*, 16(3):1905379, jan 2020.
- [216] George R. Heath, Ekaterina Kots, Janice L. Robertson, Shifra Lansky, George Khelashvili, Harel Weinstein, and Simon Scheuring. Localization atomic force microscopy. *Nature*, 594(7863):385–390, jun 2021.
- [217] Remco van Erp, Reza Soleimanzadeh, Luca Nela, Georgios Kampitsis, and Elison Matioli. Co-designing electronics with microfluidics for more sustainable cooling. *Nature*, 585(7824):211–216, sep 2020.



Vytautas Navikas

PhD student in biotechnology and bioengineering

vytnav@gmail.com ✉

+41779603769 📞

Saint-Sulpice, Switzerland 📍

www.eyeofscientist.com/ 🌐

linkedin.com/in/vytautas-navikas in

Inspired by a visual side of science.

EDUCATION

PhD student in biotechnology and bioengineering

École polytechnique fédérale de Lausanne

09/2017 - Present

Lausanne, Switzerland

Projected thesis

- Biophysical applications of correlative scanning probe and super-resolution microscopy. Developed custom hardware, experimental methods, data analysis pipelines. Final thesis exam passed. Expected graduation date: 09/2021.

Master degree in Biophysics

Vilnius University

09/2015 - 06/2017

Vilnius, Lithuania

Thesis

- Scanning probe nanolithography for rapid prototyping of single-cell arrays.

Bachelor in Biophysics

Vilnius University

09/2011 - 06/2015

Vilnius, Lithuania

Thesis

- Lipid nanolithography for in vitro biophysical systems.

WORK EXPERIENCE

Manager

Baltfab ✨

04/2016 - 08/2017

Vilnius, Lithuania

Open access facility for business and research

Tasks

- Managed open-access surface bio-patterning services. (Part-time)

Engineer

Center for Physical Sciences and Technology ✨

07/2014 - 08/2017

Vilnius, Lithuania

Research institute Center for Physical Sciences and Technology

Tasks

- Various R&D projects related to biochemical surface patterning methods and their development. (Full-time)

Consultant

Spronk 3D ✨

2014 - 2017

Vilnius, Lithuania

3D animation services for science

Tasks

- Consulted various projects for scientific animation and performed visualizations with Blender 3D. (Part-time)

SKILLS AND COMPETENCES

Super-resolution microscopy

Adaptive optics

ISO 7 cleanroom experience

Wet lab skills

Image processing

Python

LabVIEW

Fiji

Adobe Illustrator

Blender 3D

CNNs

PERSONAL PROJECTS

Business Concept Course (02/2021 - 06/2021) ✨

- Developed a "Visual Scientific" business project and gained the hands-on entrepreneurship experience.

Exposure Science Film Hackathons 2018 and 2020

- Created short movies for science communication and won a public (2018) and committee (2020) awards.

Visualizing holographic product designs for Morphotonix (2018 - Present) ✨

- Making [short-videos](#) of product designs with Blender 3D for a holographic security company.

MAIN PUBLICATIONS

Correlative 3D microscopy of single cells using super-resolution and scanning ion-conductance microscopy ✨

The main publication of my PhD, showing a combination of two different microscopy modalities.

Adaptive optics enables multimode 3D super-resolution microscopy via remote focusing ✨

Developed a novel approach of remote focusing for super-resolution microscopy.

Updated full list of publications ✨

LANGUAGES

Lithuanian

Native or Bilingual

English

Expert

French

Beginner

Russian

Beginner

INTERESTS

Photography

Conceptual scientific visualizations

Scientific communication

Nanotechnology

Deep learning

MTB